Applications of Raman Spectroscopy

by

Jeremy Flannery

A thesis
presented to the University of Waterloo
in fulfillment of the
thesis requirement for the degree of
Master of Science
in
Physics

Waterloo, Ontario, Canada, 2014

I hereby declare that I am the sole author of this thesis. This is a true copy of the thesis, including any required final revisions, as accepted by my examiners.

I understand that my thesis may be made electronically available to the public.

Abstract

This thesis is devoted to exploring experimental applications of Raman spectroscopy. The ability of Raman spectroscopy to investigate the vibrational modes of a molecule was explored in several studies. The work included using Raman spectroscopy to examine the molecular configuration of proteins, the relative amounts of certain molecules present in a nanoporous material, the enhanced scattering properties of nano-structures and finding the local temperature of nanowire materials.

The primary research project presented in this thesis focused on determining the structural conformation of lysozyme in a variety of contact lens solutions and the relation to its functionality. Protein activity was established by the use of micrococcal assays. The two multipurpose solutions tested, BioTrue and ReNu, as well as a neutralized hydrogen peroxide solution, ClearCare, showed no indications of major structural alterations in the lysozyme when exposed to the separate solutions. The assay experimental data indicated a consistently high protein activity during exposure to the various solutions. Both the data indicating a native structural conformation and high degree functionality result in the conclusion that the multipurpose solutions do not denature lysozyme during a regular cleaning cycle.

The non-neutralized ClearCare and the other hydrogen peroxide solution, UltraCare (both neutralized and non-neutralized), demonstrated signs of lysozyme denaturation within a time period of a typical cleaning cycle, due to structural changes to the protein. However, the functionality of non-neutralized UltraCare and ClearCare (by the micrococcal assay) were both found to remain relatively high, seemingly contradicting the structural indications of denaturation. This discrepancy between the structure and function of the proteins may be attributed to the irreversible process of aggregation that occurs at the high concentrations of protein which are require to produce a strong Raman signal. However, the relatively lower concentration of lysozyme used in the assay experiments better reflect the true amounts found in the tear film. Thus, the conclusion can be made that if lysozyme is denatured by the majority of the solutions, they are only reversibly denatured, posing minimal risks when reintroduced back into the eye. The only contact lens solution that may pose the potential for inducing an inflammatory response to permanently denatured lysozyme is following exposure to neutralized UltraCare. The exact reason for this permanent denaturation seems to be from the components of the neutralizing tablet, but this requires further investigation.

Raman spectroscopy was also employed in several additional research projects for other graduate groups. The first side project involved the use of heptane to wash away only

the low M_w polystyrene molecules in blend samples of high and low M_w to produce a nanoporous material. The efficiency of this process was determined by deuterating the high M_w, which shifts certain characteristic spectral peaks creating distinct Raman signatures for each component. The relative amounts of the different M_w polystyrene molecules was measured by comparing the intensities of these corresponding shifted spectral peaks. The heptane washing procedure is almost perfectly efficient for percentages of $< 30\%$ low M_w. However, this technique loses all dissolving ability for percentages $< 10\%$ low M_w.

Another side project presented in this thesis was the examination of Raman signal enhancing effects for graphene on different silver nano-structures. The two types of nano-structures studied were a ring and crescent pattern with varying dimensional sizes. The greatest enhancement of the graphene Raman peaks achieved was due to a crescent shaped structure producing an increase in Raman signal by a factor of 890. These results were also compliant with the theoretical model of the enhanced electric field localized at the nano-structures.

The last research project involved using Raman spectroscopy to investigate any changes occurring with changing the temperature of GaAs nanowires. The heating effect caused by the incoming excitation radiation was studied by using the spectral shifts of the characteristic TO and LO peaks of GaAs nanowires to calculate the local temperatures of the samples. A variety of diameters of the etched GaAs nanowires was tested and the optimal heating occurred by a resonance effect at a diameter of 95 nm. These findings suggest that the particular wavelength of the incident radiation source corresponds to a specific nanowire size in which this photo-thermal heating effect is maximized.

Acknowledgements

I would like to thank my two supervisors, Jamie Forrest and Lyndon Jones, for their generosity in supplying me with the opportunity to perform the research in this thesis under their guidance. Their continual encouragement facilitated the support and leadership needed for me to complete my degree. I also would like to thank my advisory committee members Walter Duley and Kostadinka Bizheva for their contributions and input to my research.

I thank my fellow research students Chad Daley, Kurt Schreiter, Yu Chai, and Brad Hall for their friendship and feedback with regards to any concern I may have had while performing this project. I would like to Miriam Heynen at Optometry and Vision Science for her invaluable guidance and suggestions experiments utilized in this thesis. I am also thankful to Mohammadreza Khorasaninejad and Jaspreet Walia for their collaborations of certain data in this thesis.

Lastly, I would like to thank my mother, Laurie, my father, Timothy, and my brother, Bryan, for their uncompromising support and for allowing me to follow my passions and interests, resulting in the enrichment of both my personal and academic life.

Dedication

This thesis is dedicated to my friends and family who have encouraged me and stood by the writing of this thesis allowing me to persevere through any and all obstacles I have faced in this period of my life.

Table of Contents

List of Tables xi

List of Figures xii

1 Introduction 1

I Background Information 4

2 Raman Spectroscopy 5

2.1 Historical Perspective . . . 6

2.2 Fundamentals of Spectroscopy . . . 7

2.2.1 Electromagnetic Radiation and Molecular Interactions . . . 9

2.2.2 Absorption and Emission . . . 10

2.2.3 Transition Dipole Moment . . . 14

2.3 The Raman Effect . . . 17

2.3.1 Classical Model . . . 18

2.3.2 Quantum Model . . . 21

2.4 Vibrational Spectroscopy . . . 23

2.4.1 Features of Vibrational Spectra . . . 26

2.5 Selection Rules . . . 28

2.5.1 Group Theory and Symmetries . . . 29
2.5.2 Vibrational Selection Rules . . . 33
2.6 Raman vs IR Spectroscopy . . . 36
2.6.1 Advantages of Raman Spectroscopy . . . 37
2.6.2 Disadvantages of Raman Spectroscopy . . . 37
2.7 Surface Enhanced Raman Spectroscopy . . . 38

3 Proteins **40**
3.1 Protein Structure . . . 40
3.2 Denaturation . . . 46
3.2.1 Forces Affecting Protein Configuration . . . 48
3.3 Aggregation . . . 49
3.4 Lysozyme . . . 51
3.4.1 Structure . . . 51
3.4.2 Function . . . 52
3.4.3 Human and Hen Egg-White Lysozyme . . . 52
3.4.4 Denaturation of Lysozyme . . . 54

4 Motivations for Contact Lens Research **56**
4.1 Contact Lens Materials . . . 56
4.2 Contact Lens Solutions . . . 57
4.2.1 Hydrogen Peroxide Systems . . . 58
4.2.2 Multi-purpose Solutions . . . 60
4.3 Corneal Staining . . . 61
4.4 Relevance of Lysozyme in Contact Lens Research . . . 62
4.5 Objectives . . . 64

5 Experimental Techniques **65**
5.1 Raman Spectrometer . . . 66
5.1.1 Optical Path in the Raman Spectrometer . . . 66
5.1.2 System Configurations . . . 69
5.1.3 Sampling Procedures . . . 69
5.1.4 Data Analysis . . . 71
5.1.5 Interpretation of Lysozyme Spectra . . . 71
5.2 Micrococcus Assay . . . 76
5.2.1 General Concept . . . 76
5.2.2 Experimental Procedure . . . 77
5.2.3 Data Analysis . . . 78

II Lysozyme Denaturation Results and Discussion **80**

6 Lysozyme in Contact Lens Solutions **81**
6.1 Raman Spectra of Lysozyme in Contact Lens Solutions . . . 81
6.2 Micrococcus Assay of Lysozyme in Contact Lens Solutions . . . 93
6.2.1 Ineffective Experimental Methods . . . 93
6.2.2 Final Results . . . 98
6.3 Discussion . . . 101
6.4 Conclusion and Future Work . . . 105

III Additional Applications of Raman Spectroscopy **108**

7 Polystyrene Nanoporous Material **109**
7.1 Introduction . . . 109
7.2 Experimental Methods . . . 110
7.3 Results . . . 111
7.4 Discussion and Conclusion . . . 111

8 Graphene Raman Signal Enhancement by Silver Nano Pillars **114**

8.1 Introduction 114

8.2 Experimental Methods 115

8.3 Results 116

8.4 Discussion and Conclusion 118

9 Photo-Thermal Effects of GaAs Nano-Structures **121**

9.1 Introduction 121

9.2 Experimental Methods 122

9.3 Results 123

9.4 Discussion and Conclusion 124

References **127**

List of Tables

4.1 Average protein concentration of tear solution 63

5.1 Raman spectral peak values of native lysozyme 72

6.1 Activity assay results with and without the use of BSA 98

List of Figures

2.1 An electromagnetic wave 9
2.2 Absorption and emission of a photon. 11
2.3 Absorption, emission and stimulated emission 12
2.4 Energy-level diagram of Stokes, anti-Stokes, Rayleigh, and fluorescent scattering. 20
2.5 A Raman spectrum showing both Stokes and anti-Stokes scattering peaks. 22
2.6 Vibrational modes of carbon dioxide 24
2.7 Center of Symmetry 26
2.8 Fermi resonance 28
2.9 Symmetry operations of reflection and rotation 30

3.1 An amino acid chemical diagram 41
3.2 A polypeptide chain 42
3.3 An α helix structure 43
3.4 A β sheet structure 44
3.5 A diagram of disulfide brides. 45
3.6 Protein Aggregation 50
3.7 Primary structure of lysozyme 51
3.8 A diagram of the structure of lysozyme 53

4.1 A picture of corneal staining 61

4.2 A picture of giant papillary conjunctivitis (GPC) 63

5.1 Schematic overlay of the Raman spectrometer 67
5.2 Schematic overlay of the spectrograph. 68
5.3 Diffraction grating 68
5.4 A diagram of a peptide bond 73
5.5 Raman spectra of chemically denatured lysozyme by LiBr 74
5.6 Raman spectra of chemically denatured S-cyanoethyl lysozyme 76

6.1 Raman spectrum of ReNu solution without lysozyme 83
6.2 Raman spectrum of BioTrue 83
6.3 Raman spectrum of ReNu with lysozyme 84
6.4 Raman spectrum of BioTrue with lysozyme 85
6.5 Raman spectrum of ClearCare without lysozyme 86
6.6 Raman spectrum of UltraCare without lysozyme 86
6.7 Raman spectrum of ClearCare with lysozyme 87
6.8 Raman spectrum of UltraCare with lysozyme 88
6.9 Raman spectrum of lysozyme in 10% hydrogen peroxide solution 91
6.10 Raman spectrum of neutralized ClearCare without lysozyme 92
6.11 Raman spectrum of neutralized UltraCare without lysozyme 92
6.12 Raman spectrum of ClearCare with lysozyme 94
6.13 Raman spectrum of UltraCare with lysozyme 95
6.14 Raman spectrum of UltraCare tablet in PBS 96
6.15 Multipurpose solution activity assay 99
6.16 ClearCare activity assay 100
6.17 UltraCare activity assay 101
6.18 UltraCare tablet activity assay 102

7.1 A figure depicting the monomer styrene 110

7.2 The measured relationship between the low M_w hydrogenated PS fraction and the normalized intensity of the deuterated high M_w 112

8.1 A graphene sheet composed of carbon atoms 115

8.2 A schematic of the periodic arrangement of nano-structures to create an enhanced electric field effect 116

8.3 The enhanced Raman spectra of graphene due to the ring and crescent shaped silver nano-structures 117

9.1 Spectral decomposition of the Raman spectrum obtained from an array of 50 nm diameter nanowires 123

9.2 Raman spectra of eight different GaAs nanowire diameters ranging from 50 to 155 nm 125

9.3 The central peak positions of the TO and LO phonon modes as a function of diameter and corresponding temperature 126

Chapter 1

Introduction

The relatively new and innovative field of nanotechnology has become the forefront for research and development. The study of nanotechnology has immense potential and will most likely impact future generations of technologies in ways we are only beginning to comprehend. One exciting tool that has become increasingly more important in the understanding of materials at the nano-scale is Raman spectroscopy. This thesis is the study of the applications and enhancement techniques of Raman spectroscopy as applied to nano-scale molecules and structures.

The main attribute of Raman spectroscopy is that it allows for the structural characterization of molecules by probing the vibrational and rotational modes of the system [96]. Different atomic bonds between various elements are associated with specific modes of vibration, and thus knowledge of these modes allows for the determination of the variety of molecular bonds present. Raman spectroscopy utilizes the inelastic scattering of monochromatic light to determine these molecular modes.

When light interacts with a molecule, most of the light is simply scattered away due to Rayleigh scattering in which the incoming and outgoing photons have equivalent energy and wavelength. However, a small portion of the incident light will result in 'Raman scattering'. This process begins when the incoming photon excites certain molecular vibrational modes to a higher virtual energy state. The molecule then immediately relaxes back to a lower energy state that differs from the original state the molecule was in prior to the interaction with the photon. The resulting scattered photon will have an energy equal to the difference between the initial and final energy states of the molecule. This energy difference corresponds to a particular change in the wavelength of the photon that can be measured using a spectrometer. Each particular change in a scattered photon wave-

length corresponds to a characteristic vibrational mode of the molecule, and thus the full molecular structure may be investigated [35].

This full characterization of the molecular bonds and the symmetries of molecules is incredibly useful in a variety of applications. The Raman spectra of a substance may be used as a 'fingerprint' to identify an unknown chemical compound. For example, the compounds SiO, Si_2O_2, and Si_3O_3 were all identified with normal coordinate analyses using IR and Raman spectrums [56]. Raman has even been utilized in specific situations such as identifying counter counterfeit drugs in sealed packages, or even in detecting explosives from large distances [38]. Changes in chemical bonding may also be studied, such as that seen when enzymes bind to substrates [17, 18, 66, 103].

Raman gas analyzers have multiple uses, including medical applications such as the real-time monitoring of respiratory and anaesthetic gases during surgery [107]. Raman spectroscopy is applicable in many fields of research, from studying crystal structures and orientations of materials, analyzing nanowires, or in the non-invasive probing of biological tissues. Recent advances even allow for the detection and study of single molecules at a time using certain Raman enhancement techniques, such as surface enhancement Raman spectroscopy (SERS) [59].

The first part of this thesis details the theoretical framework behind the Raman effect, outlining how calculations of the various vibrational modes of a given molecule are possible. Specific spectroscopic techniques and methodologies are also discussed. The next chapter of the background knowledge is devoted to providing all background information and knowledge needed to understand the final results and techniques used. This includes a discussion of proteins, specifically lysozyme. The motivations behind the research in contact lens solutions, as well as the experimental methods used for this research are included in the background chapters.

The next parts of this thesis are concerned with the application of Raman spectroscopy. The main body of work in this thesis is the investigation of protein detection and the possible use of various methods to determine protein denaturation in contact lens solutions. The results of this research and the subsequent discussion of the data are presented.

The final part of this thesis is comprised of chapters describing work done for other graduate student projects. Each additional work performed involved Raman spectroscopy to investigate a particular material in some regard. These supplementary applications include using Raman spectroscopy to detect the efficiency of a novel technique for selectively removing specific polymers from thin polymer blend films to create nanoporous materials. The second project in which Raman data was collected used silver nano pillars to create surface enhanced Raman signals of a layer of graphene. This research studied the effects

from differently shaped nano-structures. The last project used etching techniques to create nano-structured Gallium Arsenide. The Raman spectra of these nanowires could be used to determine the amount of heating caused by the excitation laser.

Part I

Background Information

Chapter 2

Raman Spectroscopy

This chapter contains the theoretical background information needed to understand the Raman effect and how it is applied in spectroscopic techniques. It will begin with a brief historical perspective that describes the discovery and eventual utilization of the Raman phenomenon in spectroscopy. General background knowledge of spectroscopy and certain fundamental principles that are important for any spectroscopist will be explored. This includes a quick overview of electromagnetic waves as well as the absorption and emission rates using Einstein coefficients, and the transition dipole moment.

The interactions of light with matter will then be investigated, specifically Rayleigh scattering and the introduction of Raman scattering. Florescence will also be briefly described in contrast to Raman scattering. These processes are described with a classical as well as a quantum model. There will then be a small section on the basics of group theory and symmetries, which will lead into calculating the selection rules for vibrational spectroscopy of molecules.

The next section is concerned with the general description of vibrational spectroscopy and the features of this technique. Finally, the methods of the closely related infrared (IR) spectroscopy and Raman spectroscopy will be contrasted and compared, outlining the weakness and strengths of each technique as well as the specific uses of each. The final section will provide a brief explanation of the Raman signal enhancement effect called Surface Enhanced Raman Spectroscopy (SERS), which will be relevant in later chapters.

2.1 Historical Perspective

The long development of the instrumentation and underlining theory behind Raman spectroscopy begins with the first prediction of the inelastic scattering of light in 1923 by Adolf Smekal [95]. This prediction was later confirmed by the first observation of this phenomenon in 1928. This fundamental discovery was named after the Indian scientist who first observed it, Sir Chandrasekhra Venkata Raman. He performed these experiments together with Kariamanickam Srinivasa Krishnan, while an independent group of soviet physicists Grigory Landsberg and Leonid Mandelshtam also observed this process [88].

At the time of this discovery, only basic instruments were available. The source of light Sir Raman used was sunlight, the collecting device used was a telescope, and the detector was simply his eyes. Monochromatic light was created by looking at sunlight using a narrow band photographic filter, in which a crossed filter was then used to theoretically block all of this light. He realized that a small amount of light was still able to pass through the cross filter because it had an altered frequency. He later won the Nobel prize in physics for this remarkable accomplishment in 1930. The pioneering theoretical work behind the Raman effect was then developed in 1930-1934 by a Czechoslovakian physicist by the name of George Placzek [86].

The initial Raman instruments involved placing the sample in a long tube that would be excited with filtered monochromatic light from a gas discharge lamp. Scattered photons from the sample were put through an optical flat at one end of the tube with the use of photographic detectors. However, the low sensitivity of this device required the sample to be highly concentrated (1 Molar or more) at large volumes (5ml or more) in order to maximize the signal. Due to these features, Raman devices were used less when infrared (IR) instruments became commercially available in the 1940s.

Fortunately, improvements to the various components of the Raman instrumentation have developed over time. A major component that has gone through many variations throughout the decades is the source of the excitation light. The first excitation sources used were lamps of different elements, but these lamps produced low light intensities.

The first main improvement to the light sources was to use mercury lamps. In 1939 a mercury burner was utilized by Hibben, while a cooled version was experimented with by Spedding and Stamm in 1942. In 1948 further progression by Rank and McCartney was made by studying the backgrounds of mercury burners. A commercial mercury excitation source consisting of the Raman tube surrounded by four lamps was then made available by Hilger Co. This lamp was further improved upon in 1952 by Welsh, using a four-turn helix of Pyrex tubing known as the Toronto Arc. Other materials began to be examined,

including helium, argon, rubidium, and caesium to create coloured lamps. Finally, in 1962, laser technology was incorporated to Raman systems. The Ar^+ (351.1-514.4 nm) and the K^+ (337.4-676.4 nm) lasers, as well as the more recent Nd-YAG laser (1,064 nm) were all developed and have been used in Raman spectroscopy. The invention of the laser drastically increased in the sensitivity of Raman spectra, promoting the relevance of this technique for scientific research.

The detection systems have also gone through a long history of development. The original measurements were made with photographic plates. However, this included a very tedious and inept development process. During World War II, photoelectric Raman devices were introduced, the first of these being used in 1942 by Rank and Wiegand, using a cooled cascade detector. In 1950, the Heigl instrument was produced, using a cooled photomultiplier tube. In 1953, the Hilger E612 instrument was introduced, which incorporated both a photographic and photoelectric instrument. The Cary Model 81 Raman spectrometer was thereafter produced with the use of a 3 kW helical Hg arc of the Toronto type and contained a twin-grating, twin-slit double monochromator. The eventual shift from photographic detection to spectroscopic detection greatly increased the resolution and accuracy of Raman spectra.

The optical arrangements of the Raman setup even went through different stages of advancement. These major developments occurred in the 1960s, when it was discovered that stray light could be removed more efficiently using a double monochromator, rather than a single monochromator. Naturally, a triple monochromator was soon after used to remove this stray light even more effectively. In 1968, holographic gratings were added in commercial Raman optics to improve the proficiency of collecting Raman scattered light.

These developments have all facilitated the increase in applicability and utility of Raman spectrometers. This allowed for the use of Raman spectra to be the first technique to catalogue molecular frequencies. Current Raman spectra can now also be obtained by Fourier transform (FT) spectroscopy and are even commercially available as duel systems combined with Fourier transform infrared (FT-IR) instruments [35].

2.2 Fundamentals of Spectroscopy

The general field of spectroscopy is defined simply as the study of the interaction of matter with radiation. This radiation may be in the form of energetic particles, radiated pressure waves (acoustic spectroscopy) or, most commonly, electromagnetic radiation. This broad concept includes daily phenomenon such as our observation of the colours of materials.

Paints and dyes are composed of chemicals that are specifically selected for their spectroscopic characteristics in order to produce a variety of colours and hues. Fluorescent lightings, and other neon lamps, involve the collision of electrons with a gas, such as neon or other noble gases. This excites the atoms, resulting in the emission of light of a different colour depending on the certain type of gas.

In experimental methodologies, spectroscopy refers to the measurement of the intensity of this radiation as a function of the frequency when interacting with a substance to produce a spectrum. There are several different types of interactions that may be described by these spectra, such as the absorption and emission of radiation. Photons may be scattered by the material elastically, which involves how the incident radiation is reflected and scattered by the material. They may also scatter inelastically, which describes how the incident radiation exchanges energy with the material. Other interactions include the impedance of a material, which depicts the ability of the medium to slow the transmittance of energy, and coherence, involving the coupling of two quantum states of the material by the radiative energy.

One of the main components behind the basic theory of any type of spectroscopy is a mechanism of resonance. In quantum systems, this translates to a coupling between quantum mechanical states, such as atomic states. A photon can then act as an oscillatory source of energy that is capable of coupling these states when its energy is close to the energy difference between the states. The spectra produced by atoms and molecules are composed of peaks that represent the resonance between quantum states.

Molecules can be considered as a combination of atoms to create a unique energy state with a unique spectrum indicating its transitions between these states. Molecular spectral peaks are mainly due to the transitions between rotational, vibrational and electronic states. Rotations are the collective motion of atomic nuclei, which typically lead to features in the microwave spectral region. Vibrational modes are defined as the relative motions between atomic nuclei, which are mainly studied by Raman and IR spectroscopy, as further discussed in section 2.4. The electronic states are the energy states of the bound electrons. These transitions are best studied with visible and ultraviolet spectroscopy, as well as fluorescent spectroscopy.

Spectroscopy appears in a range of research areas such as physical and analytical chemistry. It is even applicable in astronomy and remote sensing on Earth, with most research telescopes incorporating spectrographs into their design. This is due to the ability of spectroscopy to detect, identify, and quantify information about atoms and molecules by their unique spectra.

The following sections of 2.2.1, 2.2.2, 2.2.3 outline the important fundamental principles

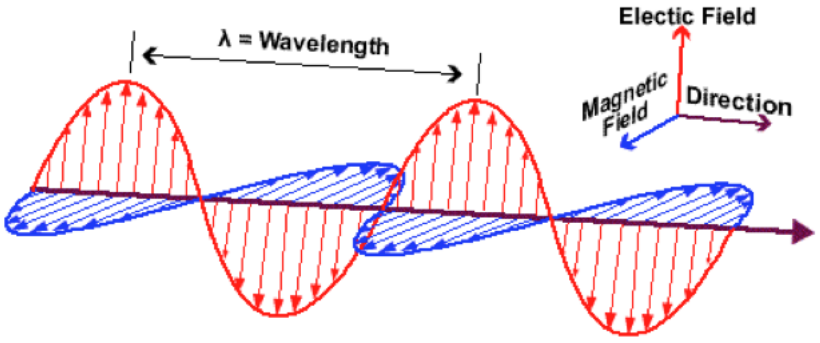

Figure 2.1: An electromagnetic wave with oscillating electric and magnetic fields in perpendicular directions [15].

of light interacting with matter. Knowledge of these interactions are incredibly valuable and essential to all types of spectroscopy. Specifically, an introduction to electromagnetic radiation, the absorption and emission rates using Einstein coefficients. The transition dipole moment will the be discussed, which will become central when using the selection rules of vibrational modes in section 2.5.

2.2.1 Electromagnetic Radiation and Molecular Interactions

Light can be described as a propagating electromagnetic wave. It consists of an electric field oscillating in one direction and a magnetic field oscillating in a perpendicular direction to the electric field. Both the electric and magnetic fields oscillate in perpendicular directions to the direction of motion, as shown in figure 2.1. In most situations, only the electric component of the wave is considered. This mostly is due to the fact that the magnetic field strength is very weak relative to the electric field strength, and thus the interactions that will be discussed do not involve magnetic phenomena.

The electric field as a function of time, t, and space, $\vec{r}$, may be expressed as

$$\vec{E}(\vec{r},t) = \vec{E}_0 \cos(\vec{k}\cdot\vec{r} - \omega t) \tag{2.1}$$

where $\vec{E}_0$ is the amplitude, ω is the angular frequency of the wave, and $\vec{k}$ is the wavevector which is in the direction of propagation. The angular frequency is proportionate to the

frequency, ν, of the wave by $\omega = 2\pi\nu$. The wavevector is related to the wavelength by $|\vec{k}| = 2\pi/\lambda$.

The relationship between the frequency and wavelength, λ, of the wave can be expressed as

$$\nu = \frac{c}{\lambda} \tag{2.2}$$

where c is the speed of light.

The most common parameter used in vibrational spectroscopy is called the wavenumber, $\tilde{\nu}$, which is defined by

$$\tilde{\nu} = \frac{\nu}{c} \tag{2.3}$$

Using equation 2.2 and 2.3, the relationship between the parameters describing a wave can be obtained as

$$\tilde{\nu} = \frac{\nu}{c} = \frac{1}{\lambda} \tag{2.4}$$

When molecules interact with electromagnetic fields, energy is transferred from the fields to the molecule. This causes the excitation of the molecule from a low energy state to a higher one. In quantum mechanical systems, these energy states are quantized, requiring the molecule to only occupy certain discrete states. In the same manner, the quantization of electromagnetic radiation can be considered, which is termed a photon. Photons can be described as discrete packets of light with an energy of

$$E = h\nu = h\frac{c}{\lambda} = hc\tilde{\nu} \tag{2.5}$$

where E is the energy of the photon, and h is Planck's constant.

If the energy difference, ΔE, between two quantized energy states of a molecule is exactly equal to the energy of an incoming photon, the molecule may absorb the photon. Conversely, a molecule can transition from a high to a low energy state, in which a photon is emitted. The energy difference between the two quantized states of the molecule will be equal to the energy of the emitted photon, as shown in figure 2.2.

The energy difference between vibrational energy states of molecules correspond to IR and Raman spectra.

2.2.2 Absorption and Emission

The absorption and emission of photons by molecules can be simplified by examining a two-level system, with a lower energy, E_0, and an upper energy, E_1. When a unit

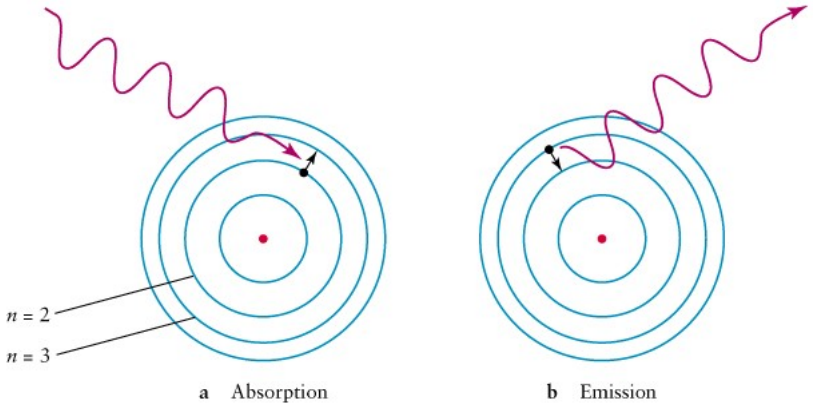

Figure 2.2: Shows the absorption of a photon with an energy equal to the energy difference, ΔE, between molecular states. Emission of a photon occurs when the molecule relaxes back to a lower energy state [64].

volume of space is considered, there may be N number of these two-level systems at a constant temperature, T. These systems are then bombarded by a radiation density of $\rho(\nu)$, which has a certain distribution as a function of frequency, ν, which is dependent on the temperature. If the number of systems with the energy E_0 and E_1 is N_0 and N_1, respectively, then since the entire population is in thermal equilibrium, the relationship between N_0 and N_1 is

$$\frac{N_1}{N_0} = e^{-(E_1 - E_0)/kT} \tag{2.6}$$

This is the Boltzmann expression for thermal equilibrium. The energy difference may be equated to the energy of a photon of frequency ν_{10} using equation 2.5, such that

$$\Delta E = E_1 - E_0 = h\nu_{10} \tag{2.7}$$

Thus the Boltzmann equation becomes

$$\frac{N_1}{N_0} = e^{-h\nu_{10}/kT} \tag{2.8}$$

There are three possible processes that can alter the energy of any given system. Absorption occurs when the state changes from E_0 to E_1, while spontaneous emission and stimulated emission result in a change from E_1 to E_0 as shown in figure 2.3.

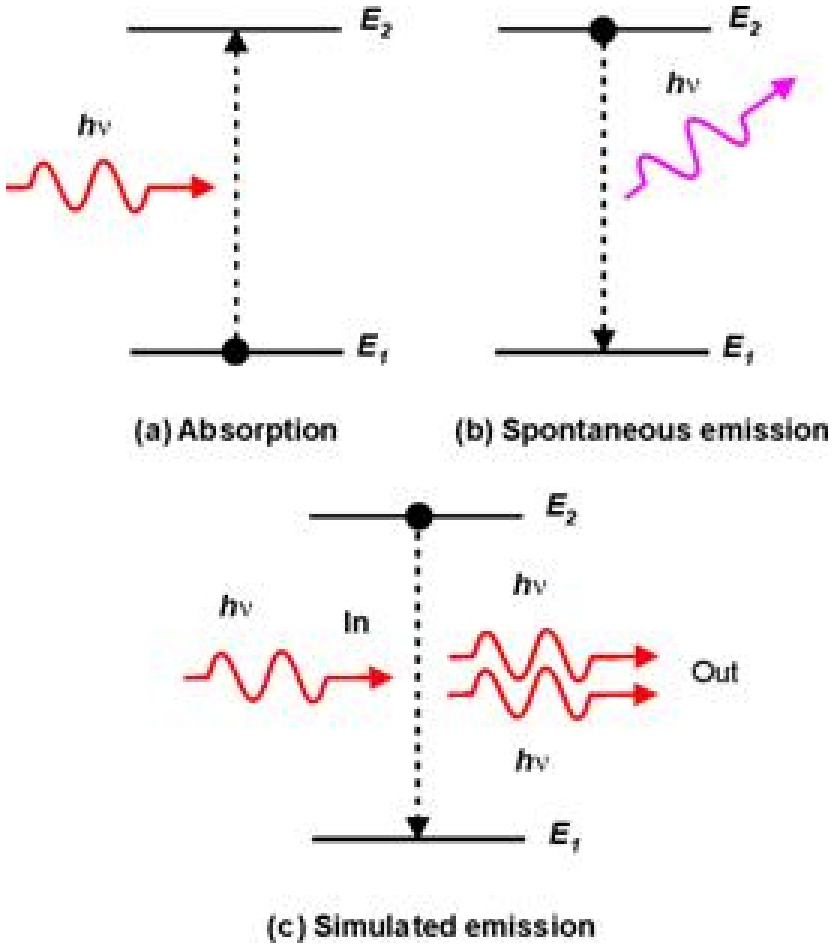

Figure 2.3: Figure a.) shows absorption of a photon b.) shows spontaneous emission c.) shows stimulated emission [61].

Absorption occurs from the interaction of the radiation density, $\rho(\nu_{10})$, at the specific frequency required to excite the transition from the ground state to the excited state. The rate of this transition is described by the rate of change of the number of excited systems, $\frac{dN_1}{dt}$, determined by

$$\frac{dN_1}{dt} = B_{0\to1}\rho(\nu_{10})N_0 \tag{2.9}$$

where $B_{0\to1}$ is a rate constant known as the Einstein absorption coefficient or the Einstein B coefficient.

If a system is already in the excited state, it may be induced to relax to the ground state by another photon of energy ν_{10} from the radiation density $\rho(\nu_{10})$. This interaction is deemed a stimulated emission and the rate of this transition is

$$\frac{dN_1}{dt} = -B_{1\to0}\rho(\nu_{10})N_1 \tag{2.10}$$

where $B_{1\to0}$ is the stimulated emission coefficient. This rate of change is negative because stimulated emission causes the number of excited states to decrease.

The last transition that may occur is when an excited state spontaneously emits a photon at a rate

$$\frac{dN_1}{dt} = -A_{1\to0}N_1 \tag{2.11}$$

where $A_{1\to0}$ is the spontaneous emission coefficient or Einstein A coefficient. This rate is again negative because spontaneous emission results in a decrease in the number of excited states in the volume.

Due to the assumption that this entire collection of systems are in equilibrium, the total number of systems in the upper energy state must be constant, thus

$$\frac{dN_{1total}}{dt} = 0 \tag{2.12}$$

The total change in the number of excited states is simply the sum of the rates of absorption, stimulated emission and spontaneous emission. Using equations 2.9, 2.10 and 2.11, equation 2.12 becomes

$$\frac{dN_{1total}}{dt} = B_{0\to1}\rho(\nu_{10})N_0 - B_{1\to0}\rho(\nu_{10})N_1 - A_{1\to0}N_1 = 0 \tag{2.13}$$

and thus

$$\frac{N_1}{N_0} = \frac{B_{0\to1}\rho(\nu_{10})}{B_{1\to0}\rho(\nu_{10}) + A_{1\to0}} = e^{-h\nu_{10}/kT} \tag{2.14}$$

using equation 2.6. Using equation 2.14 to solve for $\rho(\nu_{10})$ yields

$$\rho(\nu_{10}) = \frac{A_{1\to0}}{B_{0\to1}e^{h\nu_{10}/kT} - B_{1\to0}} \tag{2.15}$$

The radiation density, however, can also be described by the Plank function for black body radiation, in which

$$\rho(\nu_{10}) = \frac{8\pi h\nu_{10}^3}{c^3}\frac{1}{e^{h\nu_{10}/kT} - 1} \tag{2.16}$$

Thus for both equations 2.15 and 2.16 to be true, it is necessary that

$$B_{0\to1} = B_{1\to0} \tag{2.17}$$

and it follows that

$$A_{1\to0} = \frac{8\pi h\nu_{10}^3}{c^3}B_{0\to1} \tag{2.18}$$

Both equations 2.17 and 2.18 are remarkable as they have significant implications. These results indicate that the rate constants for absorption and stimulated emissions are equivalent, despite the fact they are separate physical phenomena. Additionally, the spontaneous emission constant (and thus rate) can be calculated from the absorption coefficient using equation 2.18. This reveals that there is a ν_{10}^3 factor relating the competing processes of induced and spontaneous emission.

2.2.3 Transition Dipole Moment

The concept of a two-level system allows for the introduction of quantum mechanics by describing each of these upper and lower states of the molecule as wavefunctions, ψ_1 and ψ_2, respectively. The energy levels of the molecule can be obtained from the eigenfunctions of the time-independent Schrödinger equation

$$\hat{H}\psi_n = E_n\psi_n \tag{2.19}$$

for a given state, ψ_n, at a certain energy, E_n, in which its Hamiltonian is given by $\hat{H}$. The Hamiltonian of the system is an operator corresponding to the total energy, which essentially is the summation of its kinetic and potential energies. As before, a photon with an energy of $E_1 - E_0 = h\nu = \hbar\omega$ is required to promote the transition from the lower state to the higher energy state.

Any molecule can be described as a collection of positively charged nuclei and negatively charged electrons. Thus, this system of particles has a given charge, q_i, at a position, $\vec{r_i} = (x_i, y_i, z_i)$, with a net electric dipole moment, $\vec{\mu}$, with components defined by

$$\begin{aligned} \mu_x &= \Sigma x_i q_i \\ \mu_y &= \Sigma y_i q_i \\ \mu_z &= \Sigma z_i q_i \end{aligned} \tag{2.20}$$

The coordinates of the particles are relative to the center of mass of the molecule.

The interaction of the electromagnetic radiation and the molecule causes a time-dependent perturbation of the initial Hamiltonian of the material. This perturbation, $\hat{H}'$, is dependent on the electric dipole moment of the molecule using equation 2.20, and the varying electric field described by equation 2.1. This resulting change in the Hamiltonian is

$$\begin{aligned} \hat{H}' &= -\vec{\mu} \cdot \vec{E(t)} \\ &= -\vec{\mu} \cdot \vec{E}_0 \cos(\vec{k} \cdot \vec{r} - \omega t) \end{aligned} \tag{2.21}$$

The electric field can be assumed to be in the z direction and the molecular system can be set at the origin, thus $\vec{r} = 0$. The wavelength of the radiation can also be set to much greater than the dimensions of the system, allowing for the field strength to be constant at all parts of the system. The perturbation in the Hamiltonian then simply becomes

$$\hat{H}' = -\mu_z E_{0z} \cos(\omega t) \equiv -\mu E \cos(\omega t) \tag{2.22}$$

The new perturbed time-dependent Schrödinger equation becomes

$$i\hbar \frac{\partial \Psi}{\partial t} = [\hat{H} + \hat{H}']\Psi \tag{2.23}$$

When the photon is not interacting with the system, and the initial Hamiltonian, $\hat{H}$, is not perturbed, the solutions of equation 2.23 for the upper and lower energy states are

$$\begin{aligned} \Psi_0 &= \psi_0 e^{-iE_0 t/\hbar} = \psi_0 e^{-i\omega_0 t} \\ \Psi_1 &= \psi_1 e^{-iE_1 t/\hbar} = \psi_1 e^{-i\omega_1 t} \end{aligned} \tag{2.24}$$

since $\omega_n = E_n/\hbar$.

The general solution to the perturbed Schrödinger equation is a linear combination of the complete set of the wavefunctions Ψ_0 and Ψ_1 given by

$$\begin{aligned}\Psi(t) &= a_0(t)\Psi_0 + a_1(t)\Psi_1 \\ &= a_0\psi_0 e^{-i\omega_0 t} + a_1\psi_1 e^{-i\omega_1 t}\end{aligned} \tag{2.25}$$

The time-dependent coefficients of the linear combination are a_0 and a_1. Using this solution of equation 2.25 and substituting into the Schrödinger equation (2.23), and taking into account the unperturbed Schrödinger equation (2.19), then

$$i\hbar(\dot{a}_0\psi_0 e^{-i\omega_0 t} + \dot{a}_1\psi_1 e^{-i\omega_1 t}) = \hat{H}' a_0\psi_0 e^{-i\omega_0 t} + \hat{H}' a_1\psi_1 e^{-i\omega_1 t} \tag{2.26}$$

where a dot notation signifies a time derivative, $\dot{a} \equiv da/dt$.

Two coupled differential equations can be derived using equation 2.26. This is done by multiplying both sides by $\psi_0^* e^{i\omega_0 t}$ and integrating over all space to produce the first equation. The second equation is obtained by multiplying both sides by $\psi_1^* e^{i\omega_1 t}$ and integrating over all space, giving

$$\begin{aligned}i\hbar\dot{a}_0 &= a_0\langle\psi_0|\hat{H}'|\psi_0\rangle + a_1\langle\psi_0|\hat{H}'|\psi_1\rangle e^{-i\omega_{10}t} \\ i\hbar\dot{a}_1 &= a_0\langle\psi_1|\hat{H}'|\psi_0\rangle e^{i\omega_{10}t} + a_1\langle\psi_1|\hat{H}'|\psi_1\rangle\end{aligned} \tag{2.27}$$

where $\omega_{10} \equiv \omega_1 - \omega_0$. The Dirac notation is also used in which $\langle f_1|\hat{A}|f_2\rangle \equiv \int f_1^* \hat{A} f_2 d\tau$. The orthogonality of the two states, ψ_0 and ψ_1, are utilized in these equations, such that $\langle\psi_0|\psi_1\rangle = \langle\psi_1|\psi_0\rangle = 0$. The coupled equations (2.27) are equivalent to the original Schrödinger equation and has made no approximations other than restricting each system to only two discrete states, ψ_0 and ψ_1.

In order to help evaluate the integrals of equations 2.27, the perturbation of the Hamiltonian, $\hat{H}'$, can be expressed using the electric-dipole approximation by equation 2.22. This perturbation is an odd function with respect to space since $\mu = ez$, while $|\psi_0|^2$ and $|\psi_1|^2$ are even functions. This means the integrands $\psi_0^*\hat{H}'\psi_0$ and $\psi_1^*\hat{H}'\psi_1$ are both odd functions, and thus

$$\begin{aligned}\langle\psi_0|\hat{H}'|\psi_0\rangle &= \int \psi_0^*\hat{H}'\psi_0 d\tau = 0 \\ \langle\psi_1|\hat{H}'|\psi_1\rangle &= \int \psi_1^*\hat{H}'\psi_1 d\tau = 0\end{aligned} \tag{2.28}$$

This reduces the coupled equations 2.27 to

$$\begin{aligned}i\hbar\dot{a}_0 &= -a_1 M_{01} E e^{-i\omega_{10}t}\cos\omega t \\ i\hbar\dot{a}_1 &= -a_0 M_{01} E e^{i\omega_{10}t}\cos\omega t\end{aligned} \tag{2.29}$$

where

$$M_{01} = M_{10} \equiv \langle \psi_1 | \mu | \psi_0 \rangle \tag{2.30}$$

is an integral called the transition dipole moment.

The purpose of this section was to provide a brief introduction to this concept of the transition dipole moment. It is one of the most important quantities in spectroscopy, as it is used to derive the selection rules for molecular spectra and line intensities, which will be discussed in sections 2.5 and 2.4. This is due to its apparent significance in the relative amplitudes of the two quantum states, ψ_0 and ψ_1 for a general state involving the superposition of the two wavefunctions.

2.3 The Raman Effect

The Raman effect is a phenomenon that may occur when light is scattered. When light is passed through a material, a fraction of the radiation will be scattered, even if the material is transparent. Most of this scattered light has the same frequency as the incident light, which is deemed Rayleigh scattering.

Some of the scattered light, however, will have a different frequency than the initial light. One phenomena that can result in this type of inelastic scattering of light is referred to as Raman scattering. Raman scattered light is very weak, and occurs with an intensity of about 10^{-5} of the initial source. This light will be shifted by a specific discrete amount to either a larger or smaller frequency than the original frequency, for reasons that will be further discussed in this section. Light that has been shifted to a lower frequency is called Stokes scattering, while a higher frequency is called anti-Stokes scattering. The amount of this shift from the excitation frequency is called the Raman shift, $\Delta\nu$, and defined as

$$\Delta\nu = |\nu_{incident} - \nu_{scattered}| \tag{2.31}$$

The frequency shifts of the Raman scattered light corresponds to vibrational, rotational or electronic transitions of the molecules of interest. The vibrational Raman effect is the most important and significant occurrence because the molecular structure can be fully determined if all vibrational information about the molecule is known. However, rotational and electron Raman effects are also sometimes studied. Both the classical and quantum mechanical models of the Raman effect are relevant in the understanding and application of Raman spectroscopy.

2.3.1 Classical Model

The classical theory of the Raman effect does not provide a full explanation of the phenomenon, in which quantum mechanical effects must be considered. However, classical theory is still incredibly useful in providing insight to the process of the different scatterings of light. Specifically, an understanding of the polarizability property of a molecule may also be obtained using classical theory, which is a fundamental concept to spectroscopy.

When a molecule is in the presence of an electric field, the negatively charged electrons and positively charged nuclei are forced in opposite directions according to Coulomb's law. This separation induces a dipole moment, μ_{Ind}, in the molecule. This dipole moment will be linearly proportional to the electric field as long as the field is not too strong, and thus given by

$$\vec{\mu}_{Ind} = \alpha \vec{E} \tag{2.32}$$

The proportionality constant, α, is characteristic to the molecule and is called the polarizability.

The electric field of the incoming radiation is given by equation 2.1. If the field is assumed to be in one direction with an incident frequency of ν_0 and amplitude E_0, the field becomes

$$E = E_0 \cos(2\pi\nu_0 t) \tag{2.33}$$

The induced electric dipole moment of the molecule then becomes

$$\mu_{Ind} = \alpha E = \alpha E_0 \cos(2\pi\nu_0 t) \tag{2.34}$$

If the molecule vibrates with a frequency, ν_m, the displacement between the nuclei and electrons, q, changes with time periodically and so can be written as

$$q = q_0 \cos(2\pi\nu_m t) \tag{2.35}$$

where the vibrational amplitude is q_0. For vibrations with small amplitudes, the polarizability is a linear function of displacement, and thus can be Taylor expanded to

$$\alpha = \alpha_0 + \left(\frac{\partial \alpha}{\partial q}\right)_0 q + \dots \tag{2.36}$$

with the constant α_0 as the polarizability at the equilibrium position, and $(\partial\alpha/\partial q)_0$ as the ratio of the change of α with respect to the change in q, evaluated at the equilibrium position.

The equations 2.34, 2.35, and 2.36 can be combined to obtain (up to first order terms)

$$\begin{aligned}
\mu_{Ind} &= \alpha E_0 \cos(2\pi\nu_0 t) \\
&= \alpha_0 E_0 \cos(2\pi\nu_0 t) + \left(\frac{\partial\alpha}{\partial q}\right)_0 q E_0 \cos(2\pi\nu_0 t) \\
&= \alpha_0 E_0 \cos(2\pi\nu_0 t) + \left(\frac{\partial\alpha}{\partial q}\right)_0 q_0 E_0 \cos(2\pi\nu_0 t)\cos(2\pi\nu_m t) \\
&= \alpha_0 E_0 \cos(2\pi\nu_0 t) + \frac{1}{2}\left(\frac{\partial\alpha}{\partial q}\right)_0 q_0 E_0 [\cos\{2\pi(\nu_0+\nu_m)t\} + \cos\{2\pi(\nu_0-\nu_m)t\}] \quad (2.37)
\end{aligned}$$

The final step utilized the trigonometric identity

$$\cos\theta\cos\phi = \frac{1}{2}[\cos(\theta+\phi) + \cos(\theta-\phi)] \quad (2.38)$$

The first term in equation 2.37 represents an oscillating dipole which will radiate light of frequency ν_0. Since the frequency of the radiated light is the same as the incident radiation, this first term represents Rayleigh scattered light. The second term in equation 2.37 represents Raman scattered light. The anti-Stokes portion of the Raman scattering is the term with a frequency $\nu_0 + \nu_m$, while the Stokes light is due to the term which has a frequency of $\nu_0 - \nu_m$. It is also evident that if $(\partial\alpha/\partial q)_0$ is zero, the vibration does not produce any Raman scattering. Thus, to be Raman-active, a vibration must cause some change in the molecular polarizability. This is in contrast to IR, in which activity is dependent on the vibration producing a change in the electric dipole of the molecule (which will not be proven here).

For normal Raman specroscopy, the incident radiation is chosen to have an energy below the first electronic excited state, as shown in figure 2.4. The dotted lines indicate a virtual state, which is distinguished from real excited states of the molecule.

Fluorescence is observed when a molecule is excited to a real state, unlike Raman which excites the molecule to a virtual state. This means that the radiation is actually absorbed in fluorescence, in which the molecule can proceed to decay to lower excited states over a resonance lifetime by non-radiative transitions. Radiation is then emitted for the final transition at the characteristic energy of the difference between the real energy states. The overall result of both Raman and fluorescence is the same: an incident light source is scattered with a shifted frequency in which the energy state of the molecule has changed. The Raman effect, however, is not a resonance effect since it can occur for any frequency of incident radiation, whereas fluorescence can only occur for very specific frequencies.

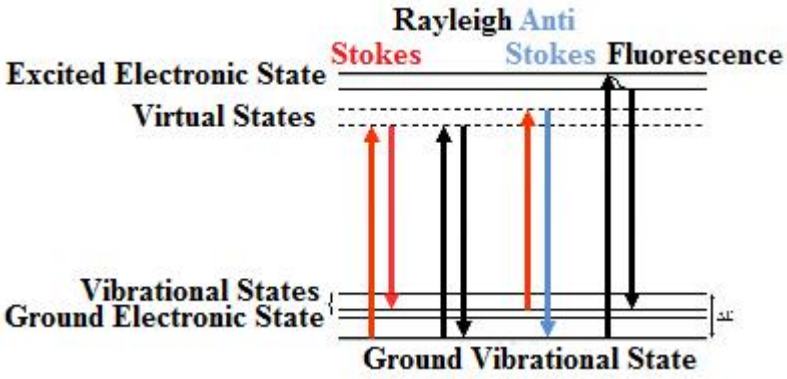

Figure 2.4: Energy-level diagram of Stokes, anti-Stokes, Rayleigh, and fluorescent scattering. Virtual states and real states are signified by dotted and solid lines, respectively [55].

Using the model of a classical oscillator, the intensity of scattered light, both Raman and Rayleigh, are proportional to the fourth power of the frequency. The intensity of the Raman scattered, I_R, light is given by

$$I_R \propto \nu^4 I_0 N \left(\frac{\partial \alpha}{\partial q}\right)^2 \tag{2.39}$$

where I_0 is the incident laser intensity, and N is the number of scattering molecules in a given state [62]. Equation 2.39 indicates several different parameters that affect the amount of Raman scattering that occurs. An increase in either the concentration or the excitation intensity will both increase the amount of Raman scattered light. This equation for intensity also clearly demonstrates that the Raman effect can only be caused by vibrations that cause a change in the polarizability. As previously mentioned, this change in polarizability with respect to the vibrational amplitude, $\left(\frac{\partial \alpha}{\partial q}\right)$, cannot be zero in order for Raman scattering to occur.

Equation 2.39 can also be used to find the ratio of the intensity of Stokes and anti-Stokes scattering. It is evident that anti-Stokes scattering occurs less often than Stokes scattering, causing much stronger Stokes lines than anti-Stokes. This is due to the fact that, in thermodynamic equilibrium, the population of molecules, N, in the lower energy states will be much larger than that for the higher energy states by the Maxwell-Boltzmann distribution law. Only molecules that are initially in a higher energy state can undergo anti-Stokes scattering.

This ratio is also dependent on the temperature of the molecules. If the Boltzmann distribution of vibrational populations is included, the ratio between the Stokes and anti-Stokes radiation intensities becomes

$$\frac{\text{Anti-Stokes intensity}}{\text{Stokes intensity}} = \frac{(\nu_0 + \nu_m)^4 e^{-h\nu_m/k_B T}}{(\nu_0 - \nu_m)^4} \tag{2.40}$$

where k_B is Boltzmann's constant and T is the temperature of the material. This applies for non-degenerate vibrations, ν_m [6]. Since the magnitude of the difference between the initial and final molecular states is the same for Stokes and anti-stokes, both processes give the same information.

For these main reasons, only the Stokes side of the spectra are customarily measured under normal conditions. Figure 2.5 shows a Raman spectrum plotting the intensity at varying wavenumber shifts, $\Delta k = \frac{1}{\lambda_0} - \frac{1}{\lambda_1}$, from the incident radiation (note the large Rayleigh intensity of unshifted scattered light at a wavenumber $\Delta k = 0$).

2.3.2 Quantum Model

Quantum mechanics can be used to create a relatively simply conceptual picture of the underling mechanism behind the Raman scattering. As previously discussed in section 2.2.1, quantum mechanics treats electromagnetic radiation as quantized particles, called photons, with energy $h\nu$. This means a scattering process may be partially described as a collision between two particles, a photon and a molecule. Rayleigh scattering then represents an elastic collision between these particles, as no energy is exchanged between the two. Raman scattering, conversely, represents inelastic collisions since energy between the photon and molecule is exchanged.

Molecules are thus allowed to gain or lose energy in this description, however, they still must obey quantum laws. This means that its energy cannot change by a continuous amount, and instead may only be altered by certain discrete amounts. The energy absorbed or lost from a photon must be equal only to the exact difference between any two of its allowed energy states. This energy change, ΔE, represents the change in the vibration or rotational energy of the molecule. If the molecule gains energy, the scattering photon will leave with an energy of $h\nu - \Delta E$, while a loss in the energy of a molecule will result in the photon to have an energy of $h\nu + \Delta E$ [4].

There are several important results derived from converting the classical model to a quantum model. As will be further discussed in section 2.5, when exploring the selection

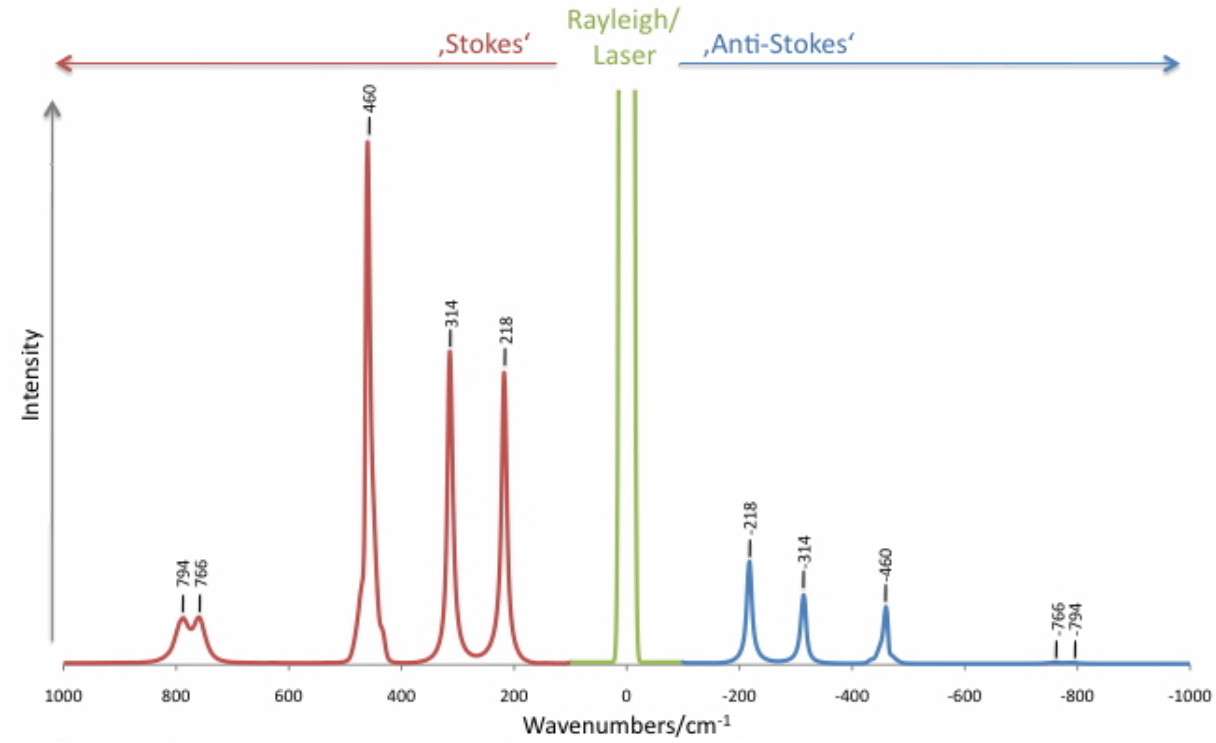

Figure 2.5: An example Raman spectrum plotting wavenumber shift vs. intensity. Both the Stokes and anti-Stokes peaks are visible and are mirror images of each other around the Rayleigh peak of unshifted light. The Stokes peaks have a much greater intensity than anti-Stokes peaks [30].

rules, it can be shown that the intensity of the Raman effect depends on the square of integrals over the displacement such that

$$I \propto |\int \psi_1^* \alpha_{ij} \psi_0 dq|^2 \quad i,j= \text{x, y and z} \tag{2.41}$$

where the vibrational wavefunctions of the initial and final states are ψ_0 and ψ_1, and the integral is evaluated in the molecular coordinate system.

The induced dipole is always in the same direction as the applied electric field for highly symmetric molecules. However, the field and dipole moment point in different directions for less symmetric molecules, and thus matrix notation is used where

$$\vec{\mu}_{Ind} = \vec{\alpha}\vec{E} \tag{2.42}$$

becomes

$$\begin{pmatrix} \mu_x \\ \mu_y \\ \mu_z \end{pmatrix} = \begin{pmatrix} \alpha_{xx} & \alpha_{xy} & \alpha_{xz} \\ \alpha_{yx} & \alpha_{yy} & \alpha_{yz} \\ \alpha_{zx} & \alpha_{zy} & \alpha_{zz} \end{pmatrix} \begin{pmatrix} E_x \\ E_y \\ E_z \end{pmatrix} \tag{2.43}$$

where $\vec{\alpha}$ is a symmetric 3×3 matrix called the polarizability tensor [6]. For normal Raman scattering, this tensor is symmetric, thus $\alpha_{xy} = \alpha_{yx}$, $\alpha_{xz} = \alpha_{zx}$, and $\alpha_{yz} = \alpha_{zy}$. Quantum mechanics dictates that if any one of these components are changed during the vibration, then it is a Raman active vibration.

2.4 Vibrational Spectroscopy

Vibrational spectroscopy includes different techniques such as mid-IR, near-IR and Raman spectroscopy. It can be used to study a wide range of sample types for full qualitative and quantitative analysis [62]. A simple, classical picture of a molecule involves the atoms and the bonds between them as being represented by balls of mass attached by springs. This picture allows for the intuitive concept of the atoms vibrating with respect to each other in different manners. These vibrations will be dependent on the mass of the atoms, the geometry of the arrangement, and the strength of the chemical bonds.

For simple diatomic molecules, the vibrations only occur along the chemical bonds. Polyatomic molecules, however, are much more complicated because each atom contributes their own harmonic oscillation about their bonds. Fortunately, these complex motions can be simplified by expressing them as a summation or superposition of several different *normal vibrations*. The normal vibrations of a molecule are the fundamental motions which

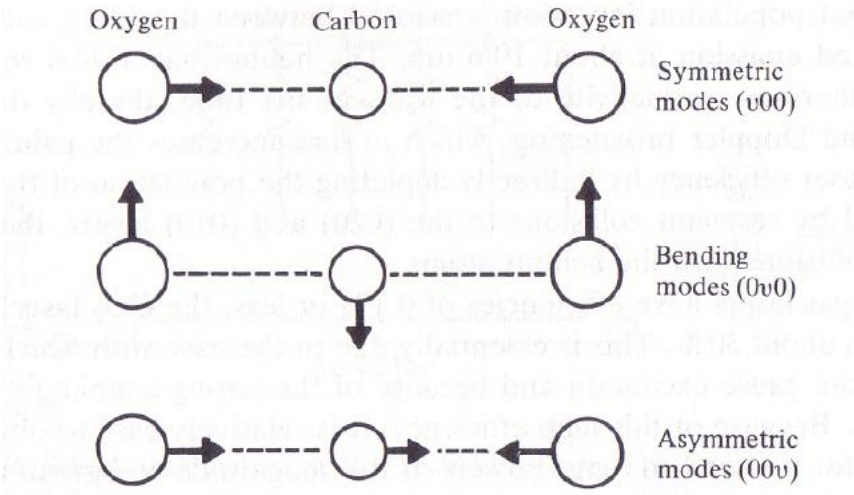

Figure 2.6: The different vibrations of carbon dioxide include symmetric and antisymmetric stretching modes, as well as bending modes [108].

are completely independent from each other in which all the atoms move with the same frequency.

The normal vibrations, for example, of carbon dioxide can be visualized modelling the atoms as masses attached by springs, as shown in figure 2.6. The two oxygen atoms could vibrate simultaneously along the bond direction in phase. This is called the symmetric stretching vibration. The oxygen atoms could be out of phase as they vibrate, causing a mode called the antisymmetric stretching vibration. The third type of motion is when the atoms move in a perpendicular direction to the bonds. This type of normal vibration is called the (symmetric) bending vibration.

These three types of motion can be combined to make any type of complicated vibrational motion that the molecule can undergo, even motion with seemingly little similarity to another one of the normal vibrations. Larger molecules have many more normal vibrations dependent on the number of atoms. The Raman instrument is used to detect only these normal vibrations.

For a molecule with N atoms, each atom being able to move in three directions (x, y, z direction), the total number of degrees of freedom of motion is thus $3N$. However, the entire molecule is free to move in the three directions without changing its shape. This translational motion of the whole molecule uses 3 degrees of freedom of the total $3N$. There are also three degrees of freedom for rotational motion of the entire molecule,

while maintaining its shape. These rotations are about the three principle axes which go through its center of gravity. All remaining types of motion allowed are then strictly internal vibrations. The net total number of vibrational degrees of freedom, and thus number of normal vibrations, is

$$\text{Number of normal vibrations} = 3N - 6 \tag{2.44}$$

However, this is a maximum number of normal modes that may be present for given molecular motions. Some of these normal vibrations in symmetric molecules may produce motion that are identical to each other in all respects except for direction of vibration. This leads to certain normal modes to be degenerate and reduces the overall number of observed separate spectral peaks.

For entirely linear molecules, the number of fundamental vibrations is slightly different. There is no rotation about the bond axis, requiring only two degrees of rotational freedom for the unchanged molecule. Thus, the total number of normal vibrations for a linear molecule is

$$\text{Number of normal vibrations} = 3N - 5 \tag{2.45}$$

The fundamental vibrations of a molecule are not all necessarily Raman active. As previously discussed in section 2.3.1, for a vibrational mode to be Raman active, the polarizability along a direction needs to change during the vibration. For molecules that are considerably symmetric, this is not a trivial task, and may require detailed considerations. However, for molecules with little or no symmetry, it is usually correct to simply assume that all its vibrational modes will be Raman active [35].

The strength of the scattering intensity is also dependent on the type of resulting vibration. As shown in equation 2.39, a larger $\partial\alpha/\partial q$ value means a larger scattering intensity and thus a strong Raman spectra line at that particular frequency shift. The general rule that is a consequence of this feature is that symmetric vibrations give rise to very strong Raman peaks, while non-symmetric vibrations are usually very weak or even unobservable. Bending motions also usually yield very weak Raman signals [4].

Another extremely important general rule in vibrational spectroscopy is called the *rule of mutual exclusion*. It states that the Raman active vibrations are IR inactive, and vice versa, for molecules with a center of symmetry. Some of the vibrations, but not necessarily all, may be both Raman and IR active if there is no center of symmetry. The definition of a center of symmetry is that for every atom in a molecule, there is an identical atom that exists on a straight line through this center, wherein this center is equal distance to

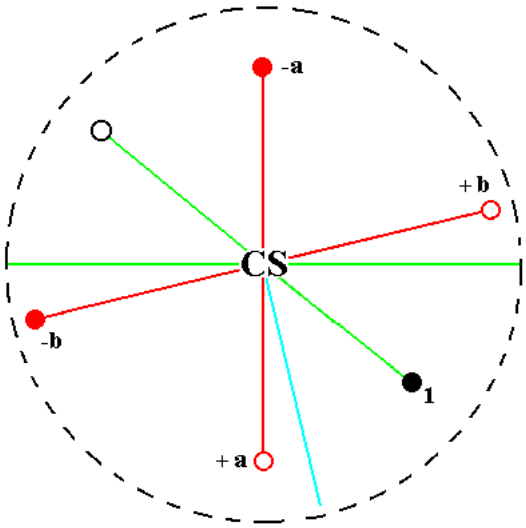

Figure 2.7: This figure shows an example of an arrangement of atoms that have the correct geometry to have a center of symmetry [78].

each of the two atoms. There does not necessarily need to be an atom at this center of symmetry [62]. Figure 2.7 shows an arrangement of atoms with a center of symmetry.

This rule is essentially due to the consequence that vibrations which retain this center of symmetry generate a change in the polarizability but no change in the dipole moment. Conversely, vibrations that do not maintain the center of symmetry will alter the dipole moment while keeping the polarizability constant, thus producing IR active and Raman inactive modes.

This concept also implies that molecules that have no common peaks in their Raman and IR spectra have no center of symmetry (assuming there are no Raman active peaks that are too weak to be observed). The concept and consequences of symmetries will be later discussed in section 2.5 as applied to the activity of molecular vibrations.

2.4.1 Features of Vibrational Spectra

The vibrations of polyatomic molecules, as previously described, can be incredibly complex. However, they may be simplified by separating them into their fundamental vibrational modes. Raman spectroscopy allows for these normal vibrations to be described by the

peaks in a spectra.

In general, the peaks of a spectrum can represent fundamental vibrations from either the functional groups or the skeletal groups. The functional groups are certain groups of atoms or bonds within a molecule that are usually responsible for the specific chemical characteristics of the molecule. These functional groups will produce relatively consistent corresponding spectral peaks regardless of what molecule they are found. The skeletal groups are simply the molecular back bone of the molecule. These frequencies are essentially dependent on the mass of the atoms, geometric arrangement, and strength of the chemical bonds involved in the vibrations.

The peaks may also, in general, be regarded as having an origin from either stretching vibrations, which involve changes in bond length, or deformation (bending) vibrations, which include the change of bond angle of the group. Each of these types of motion may arise from symmetric or asymmetric vibrations. The vibrational modes from stretching of a given functional group occur at higher frequencies than deformational motions. This is usually a result from requiring more energy to stretch the group than to deform or bend the bonds due to the bonding forces opposing the change directly (along the bond length) [96].

There are two other causes for certain spectral peaks, called overtone and combination bands. Overtone peaks are measured at approximately twice the frequency of strong fundamental vibrational peaks. The intensities decrease rapidly for higher order overtones, usually producing signals much too weak to be observed. Overtones are mostly due to the fact that the bonds between atoms do not act as perfect springs that vibrate as simple harmonic oscillators. The inclusion of anharmonic and other higher order corrections leads to this effect. Interestingly, a fundamental vibration and its overtone are not necessarily both Raman (or IR) active.

Combination bands that occur are from the addition or subtraction of two fundamental frequencies. These peaks are a result from the selection rules, as discussed in section 2.5, that occur from the addition of the higher order terms for the harmonic bonding characteristics. The occurrence of the specific overtone and combination bands are based on detailed considerations of the symmetry and modes of vibration of a molecule.

The frequencies of specific groups and bonds are relatively similar for different types of molecules, however there are many factors that may alter these frequencies in varying degrees. Spectral peaks may be affected by interactions between molecules, such as hydrogen bonding, as well as by lattice vibrations. The specific chemical composition of the rest of the molecule may also cause changes in the peaks of certain functional groups. Even the phase of the material, whether it be a solid, liquid or gas, can be a factor of alteration [96].

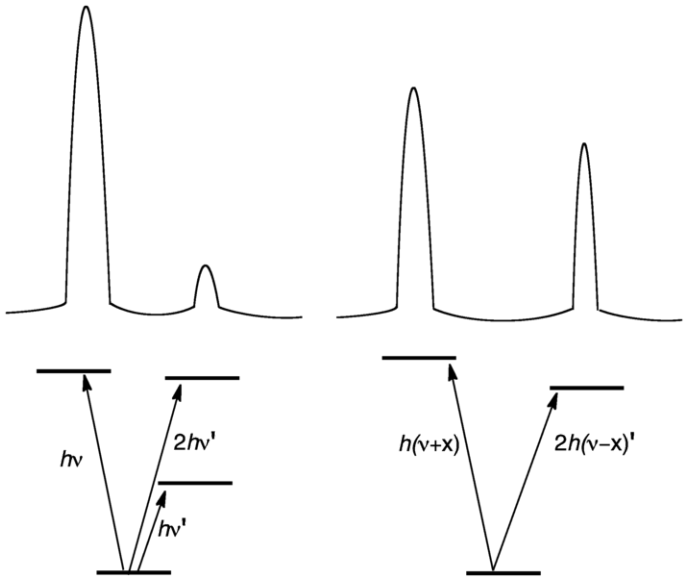

Figure 2.8: Fermi resonance causes for the higher frequency and lower frequencies to shift to higher and lower frequencies, respectively. The intensity of the weaker mode is increase, while the stronger mode decreases [80].

There are coupling effects between frequencies that can cause slight modifications to spectra. This mostly occurs between frequencies that are very close to each other, even with origins from vibrations of distinctly unrelated motions in molecules. A phenomenon known as Fermi resonance usually occurs between a fundamental vibration and an overtone or combination mode. When the frequencies of these molecular vibrations are similar, they may begin to resonate and exchange energy. Quantum mechanics mostly governs this effect, allowing for these bands to interfere with each other. The modes will diverge such that the higher frequency is shifted to even higher energies, while the lower frequency mode is shifted to a lower frequencies. The weaker mode (usually the overtone or combination band) will also gain intensity, while the stronger mode (usually the fundamental frequency) will have a decreased intensity [4]. This spectral effect is depicted in figure 2.8.

2.5 Selection Rules

As discussed in section 2.4, the maximum number of normal vibrations (and thus the number of spectral peaks) for a given molecule is determined by equation 2.44. In order

to determine which of these modes are Raman active and which are IR active, certain selection rules must be applied. For a mode to be Raman active, the vibration must cause a change in the polarizability, as shown in section 2.3.1, whereas the dipole moment must change during a vibration in order for it to be IR active [62].

For simple molecules, the activity of a certain vibration can be determined by inspection, looking at the different stages of its normal vibration and the corresponding polarizability. However, for large and complex molecules, these selection rules are much more involved. The concept of symmetry and group theory, as discussed in the next section, provide the theoretical backbones to finding the most general selection rules.

2.5.1 Group Theory and Symmetries

Group theory is essentially the language of spectroscopy, and its application to molecular symmetries has become incredibly valuable. Group theory can give qualitative information concerning the possibility of transitions between energy levels. It allows these transitions to be categorized into electric-dipole allowed and electric-dipole forbidden, thus providing insight to whether a vibration is Raman or IR active.

The concept of symmetry has an objective mathematical and geometrical definition. The symmetry of an object refers to having corresponding identical components on the opposite side of a point, line or plane called the center, axis or plane of symmetry. This is most easily understood by the use of symmetry operations, which are defined as a geometric action that can be done on the molecule to transform its configuration to one that is identical to its original configuration. This requires that the molecule is superimposable onto the original one, and thus would be indistinguishable from it, despite a possible change in its orientation.

All symmetry operations can be classified into the four types called reflections, rotations, rotation-reflections, and inversions. A symmetry element is then defined as the point, line, or axis about which this symmetry action occurs. The first symmetry is the trivial identity operation, E. This operation is a transformation of a molecule that leaves it super-imposable onto the original in which each atom goes into itself, essentially leaving the molecule unchanged.

The rotation operator, C_n, rotates the molecule about a C_n-axis by an angle $2\pi/n$ radians in a clockwise direction. A molecule with this symmetry has an n-fold axis of symmetry. The reflection operator, σ, reflects a molecule through a plane dissecting the molecule. Both planes of symmetry and an axis of symmetry are depicted in figure 2.9.

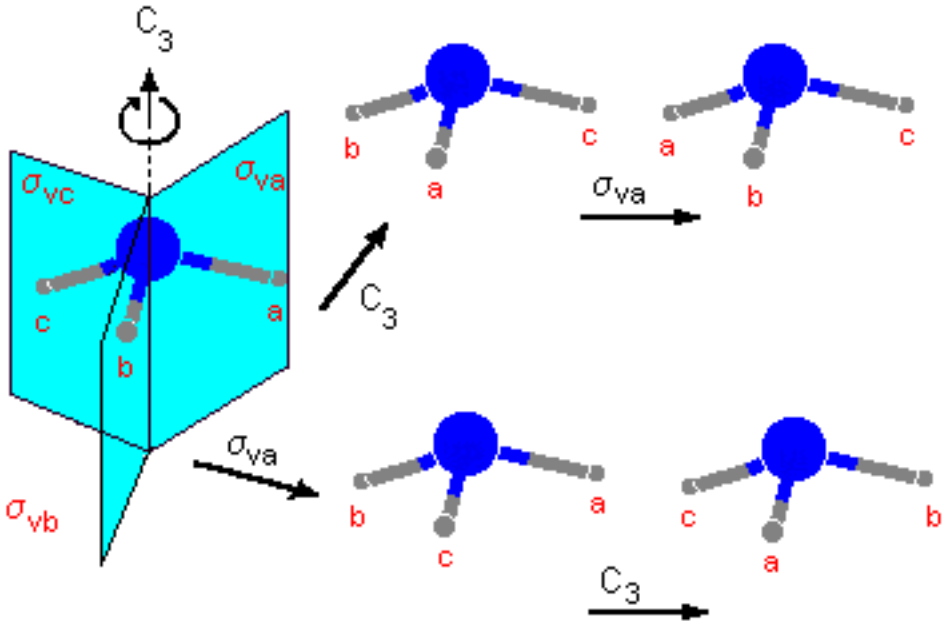

Figure 2.9: This figure depicts reflections about three planes, σ_{va}, σ_{vb}, and σ_{vc} and rotations about the axis C_3 [40].

The rotation-reflection operator, S, is simply a clockwise rotation followed by a reflection in a perpendicular plane to that axis. The last type of symmetry operation is called an inversion, i, which inverts all atoms of a molecule through a point. If this inversion process produces an indistinguishable molecule, then there exists a center of symmetry at this point [6, 35]. This symmetry property is important with regards to the rule of mutual exclusion, as discussed in section 2.6.

The general concept of a group is that it consists of a set of elements with a combining operation. These elements follow the four rules:

1. *Closure*: The combination of any two elements in the group must also be a part of the group.

2. *Associative Law*: The order of combining elements under the specific operation does not change the outcome of the created element.

3. *Identity element*: The identity element, E, is in the group.

4. *Invertibility* All elements of the group, R, have an inverse, $R^{-}1$, that is also in the group that will return the molecule back to its original configuration.

This is a broad definition of a group, in which the elements could be objects such as numbers or matrices with combining operators such as multiplication, addition, or subtraction [6].

A specific type of group in which the elements are symmetry operations of molecules for a given symmetry element is called a point group. The combining operation is to simply perform symmetry operations one after another in succession. This is due to the fact that the center of mass of the molecule does not change under all the symmetry operations, and the symmetry elements of these operations all meet at this point [35]. There are many ways to classify molecules into different point groups, but the details of this classification are beyond the subject of this thesis.

Without a great deal of mathematical rigour, it is important to note that the symmetry operations of a molecule can be represented mathematically by matrices. However, there are infinitely many different matrices that could represent a certain symmetry operation, in which a matrix is called a *representation* for that symmetry operator. These matrices are all equivalent with the same eigenvalues, traces, and determinants and may be transformed into each other by certain procedures. Each representation will have a basis formed by the basis vectors used to represent the coordinates of the atoms of a molecule in space [6].

All representations, or matrices, can be transformed to a block diagonal of the form

$$\left(\begin{array}{c|cc} 1 & 0 & 0 \\ \hline 0 & A & B \\ 0 & C & D \end{array}\right)$$

for some constants A, B, C, and D, and thus are all deemed *reducible representations*. The matrix may be any size, depending on how many atoms there are in the molecule. These new 2×2 and 1×1 matrices(depicted by the separating solid lines) are then called *irreducible representations*. This is useful because the number of reducible representations of a group is infinite, while the number of irreducible representations is always finite and usually small. The reducible matrix representation can be written as a combination of irreducible matrix representations [35].

The *character*, χ, of a matrix that acts as the reducible representation of a symmetry operator is defined as the sum of its diagonal (trace of the matrix). This allows for a single number to be used in place of an entire matrix. All symmetry operators in a molecule of the same type (called 'class'), such as reflections or rotations about different planes and axes of symmetry, will have the same character. The character of the irreducible representations can be organized into a *character table*. For example, a particular point group, called the $C_{3\nu}$ point group (which is the group of a molecule such as NH_3), has a character table of

$C_{3\nu}$	E	$2C_3$	$3\sigma_\nu$
A_1	1	1	1
A_2	1	1	-1
E	2	-1	0

The column headings E, $2C_3$, and $3\sigma_\nu$ are the types of symmetry elements in the group (2 different axes of symmetry and 3 different planes of symmetry). The row headings E (not related to the identity operator), A_1, A_2 are the different symmetry species,with a labelling scheme that will not be described in this thesis. These are essentially the irreducible representations of each of the symmetry operations. The numerical values in the table are thus the characters, or traces, of the irreducible matrix representations. Character tables are incredibly important in classifying normal vibrations by their symmetry properties [35], and are useful in determining if these normal modes are Raman active or not, as explained next in section 2.5.2. This character table, for example, gives information for a molecule to which this table corresponds to, such as NH_3. There are three sets of characters, represented by the A_1, A_2, and E species.

The A_1 symmetry species is called the totally symmetric representation and can be particularly important. It is present in all groups and its characters consist only of ones for

all symmetries (as seen in the above character table). The totally symmetric representation for the previous diagonal matrix is the 1×1 matrix of the top left corner (The E symmetry species of this matrix would be the 2×2 matrix of the bottom right) [6].

2.5.2 Vibrational Selection Rules

Quantum mechanics describes a system that can emit or absorb radiation as they make transitions between two states of different energy. This model requires the radiation and molecule to be treated as a complete system, as described in section 2.3.2, with energy being transferred through their interaction with each other. For a transition between two energy states of molecular system to take place, the transition dipole moment associated with the two molecular states must be nonzero, as shown in section 2.2.3. The intensity of the Raman transition between a final and initial state is proportionate to the square of the transition dipole moment, $M_f i$, given by equation 2.30 in which

$$M_{fi} = \langle \psi_f | \vec{\mu} | \psi_i \rangle. \tag{2.46}$$

Combining this result with the definition of the dipole moment operator, $\vec{\mu}$, using the equation $\vec{\mu} = \vec{\alpha} \cdot \vec{E}$, then

$$\begin{aligned} M_{fi} &= \langle \psi_f | \vec{\alpha} \cdot \vec{E} | \psi_i \rangle \\ &= \langle \psi_f | \vec{\alpha} | \psi_i \rangle \cdot \vec{E}. \end{aligned} \tag{2.47}$$

Thus, quantum theory gives the selection rules for the Raman spectrum being dependent on having a nonzero value for

$$\begin{aligned} [\alpha_{xx}]_{fi} &\equiv \langle \psi_f | \alpha_{xx} | \psi_i \rangle \\ [\alpha_{xy}]_{fi} &\equiv \langle \psi_f | \alpha_{xy} | \psi_i \rangle \\ &\vdots \end{aligned} \tag{2.48}$$

in which α_{xx}, α_{yy}, α_{zz}, α_{xy}, α_{xz}, α_{yz} are the six unique components of the polarizability tensor introduced in equation 2.43. If one of the six integrals of equation 2.48 is nonzero, the vibration is Raman active. If all of the components are zero, the vibration is Raman inactive.

To determine if one of the integrals of equation 2.48 is nonzero, the polarizability can be Taylor expanded, as in section 2.3.1, in terms of a normal coordinate, q_a,

$$\alpha_{xx} = (\alpha_{xx})_0 + \left(\frac{\partial \alpha_{xx}}{\partial q_a} \right) q_a + \cdots \tag{2.49}$$

A normal coordinate represents a single coordinate along which a single normal vibration can proliferate. The vibrational wavefunctions, $\psi_i(q_a)$ and $\psi_f(q_a)$, are functions of the normal coordinate, q_a, of a normal vibration, a. Then substituting equation 2.49 into equation 2.48 for an element of the polarizability tensor, results in

$$[\alpha_{xx}]_{fi} = (\alpha_{xx})_0 \langle \psi_f(q_a) | \psi_i(q_a) \rangle + \left(\frac{\partial \alpha_{xx}}{\partial q_a} \right) \langle \psi_f(q_a) | q_a | \psi_i(q_a) \rangle + \cdots \tag{2.50}$$

Since the two vibrational states, ψ_i and ψ_f, are orthogonal, the first term is zero. The terms in this equation can be assessed by assuming a quantum harmonic oscillator representing the vibrations of the molecule. This means the $\psi_i(q_a)$ and $\psi_f(q_a)$ functions are the well known harmonic oscillator wavefunctions associated with the normal coordinate, q_a, and the vibrational quantum number, ν_a^i and ν_a^f, for each state, respectively. Then these harmonic oscillator functions result in

$$\langle \psi_f(q_a) | \psi_i(q_a) \rangle = \begin{cases} 0 & \text{for } \nu_a^i \neq \nu_a^f \\ 1 & \text{for } \nu_a^i = \nu_a^f \end{cases} \tag{2.51}$$

and

$$\langle \psi_f(q_a) | q_a | \psi_i(q_a) \rangle = \begin{cases} 1 & \text{for } \nu_a^i = \nu_a^f \\ (\nu_a^i + 1)^{\frac{1}{2}} b_{\nu_a} & \text{for } \nu_a^f = \nu_a^i + 1 \\ (\nu_a^i)^{\frac{1}{2}} b_{\nu_a} & \text{for } \nu_a^f = \nu_a^i - 1 \end{cases} \tag{2.52}$$

in which

$$b_{\nu_a} \equiv \sqrt{\frac{h}{8\pi^2 \nu_a}} \tag{2.53}$$

The conditions in which the transition dipole moment is nonzero can be now considered. When $\nu_a^f = \nu_a^i$, the initial and final quantum state numbers go unchanged, and only the first term of equation 2.50 is nonzero. This represents Rayleigh scattering, and thus the result from this quantum mechanical model is the same as the classical model discussed in section 2.3.1.

Raman scattering would be characterized as a transition between two different states, and thus $\nu_a^f \neq \nu_a^i$, which results in the first term in equation 2.50 to always be zero. The second term, however, is only nonzero, and thus Raman active, for when $\Delta\nu_a = \nu_a^f - \nu_a^i = \pm 1$ (Stokes and anti-Stokes scattering). This represents a change in the vibrational quantum numbers by only one unit, which is a result of the harmonic oscillator wavefunctions. However, when higher order terms are considered in addition to the harmonic approximation, the cases in which $\Delta\nu_a = \pm 2, \pm 3, \ldots$ are allowed and are called the overtones for the a vibrational mode [35].

The concepts of group theory, as explained in section 2.5.1, can now also be applied to determining if any one of the six integrals of $\langle\psi_f|\vec{\alpha}|\psi_i\rangle$ is non-zero (since α is a matrix with six components). It can be shown with group theory that this integral will only be nonzero if the direct product of the integrand, $\psi\alpha\psi$, (for a given α component) contains the totally symmetric representation, A_1, of the point group of the molecule [35].

For the fundamental transition, in which the initial quantum state has all vibrational quantum numbers of zero, ψ_0, and the final state in which an n^{th} vibrational mode has changed to one, ψ_1, then the integration becomes $\langle\psi_1|\alpha|\psi_0\rangle$. The initial state, ψ_0, will be totally symmetric, and according to group theory, this integral will only be nonzero if the representation of the product $\alpha\psi_1$ is also totally symmetric. This would require that α and ψ_1 belong to the same symmetry species. This is generalized from the fact that the integral over all space of an odd function is zero, thus

$$\int_{-\infty}^{\infty} f(x)dx = 0$$

for any odd function, $f(x)$, such that $f(-x) = -f(x)$ [6].

In general, a given transition between an initial state, ψ_i, and final state, ψ_f, is only Raman allowed when at least one of the six triple products of the form $\psi_f\alpha\psi_i$ belong to a representation that contains the totally symmetric species. More specifically, as shown, a vibration is Raman active if at least one of the components of the polarizability belong to the same symmetry species as the vibration [35]. This is most easily determined with the use of character tables. A given molecule may have symmetries that relate to a certain point group, each corresponding to a specific well known character table that are readily available from variety of different sources.

Following the previous example of section 2.5.1, the full character table for the $C_{3\nu}$ point group is

$C_{3\nu}$	E	$2C_3$	$3\sigma_\nu$		
A_1	1	1	1	T_z	$\alpha_{xx}+\alpha_{yy}, \alpha_z z$
A_2	1	1	-1	R_z	
E	2	-1	0	$(T_x, T_y), (R_x, R_y)$	$(\alpha_{xx}-\alpha_{yy}, \alpha_{xy}), (\alpha_{yz}, \alpha_{xz})$

The third column from the left lists the symmetry species of the translational motions along the x, y, and z axes, which are T_x, T_y, and T_z, respectively. The rotational motions around the three axes are R_x, R_y, and R_z. This column in character tables represents the IR activity. The certain vibration will be IR active if it belongs to a symmetry species that has any T components.

The last column on the right gives the information involving Raman activity. If a vibration belongs to a symmetry species that contains any α components then that vibration is Raman active. There may be pairs of components that are degenerate species that are listed in parentheses. It can be seen that for a NH_3 molecule, which belongs to the $C_{3\nu}$ point group, all six normal vibrations are Raman active. This is because $\alpha_{xx} + \alpha_{yy}$ and $\alpha_z z$ belong to the A_1 species, while the pairs $(\alpha_{xx} - \alpha_{yy}, \alpha_{xy})$ and $(\alpha_{yz}, \alpha_{xz})$ belong to the E species. This information from the character table, combined with the characteristic vibrational frequencies of certain bonds can be used to predict which peaks will appear in a give spectra.

2.6 Raman vs IR Spectroscopy

Raman and IR spectroscopy are two techniques that are quite similar, however, each has its own very unique set of advantages and disadvantages. IR spectroscopy differs from Raman spectroscopy in that the molecules of interest absorb the incident infrared photons at characteristic frequencies relating to the IR active vibrational modes. There are a number of factors that must be first considered before deciding which of these two methods is best suited for a given experiment, or even if they need to be used in combination.

Both techniques provide information on vibrational frequencies. However, for a vibration to be Raman active, the polarizability must change during the vibration, as discussed in section 2.3.1. IR active modes, conversely, are ones in which the electric dipole changes during the motion. Vibrations for molecules which obey the mutual exclusion rule (molecules with a center of symmetry) are thus only either Raman or IR active, and not both.

In general, this results in Raman active modes to be symmetric or in-phase vibrations and mostly in non-polar groups. IR active modes are usually due to asymmetric or out-of-phase vibrations and polar groups [62]. This results in Raman spectra giving characteristic peaks of medium to strong intensity for skeletal vibrations, whereas these usually have weak in IR spectra [96].

There are many vibrations, however, that are not exclusive to only one type of spectroscopy, but are instead weakly active in one type, while strongly active for the other. Usually vibrations that give strong Raman signals arise from covalent bonds, while strong IR modes are produced by ionic bonds. Stretching vibrations are also generally stronger than bending motions in Raman spectra [96, 62]. It is clear that IR and Raman usually provide complimentary information, and spectra from both techniques may be needed to fully characterize the entirety of individual vibrations in a molecule.

2.6.1 Advantages of Raman Spectroscopy

Raman spectroscopy can provide several important advantages over IR spectroscopy. One advantage is that measurements of the polarization of the scattering light can provide information about the symmetry of a normal vibration for samples in solution. For these solutions in which the molecules are randomly orientated, IR spectra cannot be use to obtain any of this information.

Raman spectroscopy, unlike conventional IR spectroscopy, requires only a small sample area due to the fact that normal laser beam diameters are on the order of 1-2 mm. This is greatly advantageous when only a small quantity of the sample is accessible. Raman also allows for certain compounds that require them to be isolated from the air in glass tubing. This is not possible using IR since the glass will absorb the IR radiation.

In many cases, the sample preparation is much simpler for Raman than IR spectroscopy. The actual Raman spectrometers also allows for a very large region of the spectrum (about 50 to 4000 cm^{-1}) in a single measurement. IR spectrometers instead require for the gratings, beam splitters, filters and detectors to be changed in order to scan a large area of the spectrum [35]. Raman spectrometers can even scan at lower wavenumbers than IR spectrometers. Raman spectra may record at 100 cm^{-1} or lower, while IR spectra typically only reach to 400 or 200 cm^{-1} [96].

Raman spectra can be particularly useful when studying biological samples for several different reasons. Using the technique of resonance Raman [99], the vibrations of particular chromophoric groups (the part of a molecule responsible for its colour) in large biological molecules can be selectively enhanced. One of the most beneficial aspects of Raman spectra is that water has a very weak Raman absorption. This means that biological materials in aqueous solutions can be studied without interference. In contrast, water results in a very high absorbency in IR spectroscopy [35], thus preventing the detection of spectral signatures from other molecules of interest.

2.6.2 Disadvantages of Raman Spectroscopy

Despite the incredible potential of Raman spectroscopy to study the properties and structures of molecules, there are several disadvantages of using this technique, particularly with respect to IR spectroscopy. One such difficulty with Raman spectrometers is its ability to obtain high resolution rotational and rotation-vibrational spectra. Instead it is much easier to obtain these spectra using IR spectrometers. This problem can be mostly attributed to

the fact that Raman spectra are measured in the UV-visible region of the electromagnetic spectrum in which it is difficult to achieve high resolving power.

The instrumentation required for Raman spectroscopy usually costs more than a conventional IR system (although there are some smaller, less expensive versions [96]). This results in IR systems to generally be more available and versatile for routine analysis. The Raman system also involves a laser source to observe Raman scattering. This can cause problems such as heating, chemical breakdown or even phase changes of the sample due to the excitation radiation.

Unfortunately, quantitative measurements for a sample can be more complicated using Raman spectra. It is often the case that in order to obtain a good quality Raman spectra it requires slightly more skill by the operator than for IR spectra. However, both techniques have become more automated in recent years. Although the acquisition of Raman spectral data can be a relatively slow process compared to IR spectra.

The collection of databases and literature references for IR spectra are far more numerous than Raman references. The number of references for Raman spectra has become much better over the years, however, it still does not compete with the plethora or resources available for IR measurements.

One of the main problems that may be encountered while obtaining Raman recordings is that some samples may fluoresce when exposed to the excitation source. This results in a large background in the Raman spectra that may mask the actual peaks of interest. However, modern techniques have been able to address this problem and minimize its effects [96, 62]. Some of these methods including using computational fitting algorithms [13], as well as instrumental techniques such as excitation wavelength shifting, photo bleaching, and time-gating [92].

2.7 Surface Enhanced Raman Spectroscopy

The Raman signals of certain samples may be too weak to produce a clear spectrum, due to various reasons, including low concentrations and large background noise (including fluorescence). These issues may be overcome by increasing the sensitivity of the Raman spectra of a sample by means of Surface Enhanced Raman Spectroscopy (SERS). The Raman scattering signal can be enhanced by multiple orders of magnitude (a factor 10^{10} can be achieved for single molecules SERS) [48]. This technique involves the absorption of the analyte onto a SERS active substrate. These surfaces are composed of embedded metal nanoparticles, usually either gold or silver particles, creating a roughened surface.

The laser is then focused onto the molecules of interest that have become bound to the SERS surface, creating 'hot spots' of enhanced Raman signal [69]. The different shapes of these nanoparticles can have various enhancement effects.

The basic principles that cause the enhancement of the Raman signal can be reduced to two main effects. The first and most prominent mechanism is called the 'electromagnetic effect' and it is due to surface plasmons which are caused by the interaction of the excitation radiation and the surface electrons of the metal nanoparticles [48]. Surface plasmons are simply the quantized quasi-particle of plasma oscillations (essentially the oscillation of electrons on the surface of the substrate in response to the incident radiation) [69]. They are formed on the surface of the metal nanoparticles, which can be either spherical or elongated in nature, and are excited by the incoming light.

The energy from these surface plasmons are then transferred to the bound analyte, in which the Raman scattering process occurs on these molecules of interest. The energy is then transferred back to the nanoparticle and to the surface plasmon and the light is scattered off. Since the energy transferred to the analyte is different than the energy received back to the plasmon, the scattered light has a characteristic wavelength shift. If a resonance between the plasmons and the particular frequency of the incident photons is established, the strength of the electromagnetic fields of the scattered Raman photons from the specimen may be increased, generating a stronger Raman signal. This resonance can be achieved by choosing the correct type of metal nanoparticle that corresponds to a certain frequency and polarization of laser light used. [3, 48].

The other effect, called the chemical (or charge) transfer effect, only applies to the first layer of the specimen effect. The polarizability of this layer of molecules is amplified due to a transfer of charge between the specimen molecules and the metal nanoparticles. When the sample molecules are absorbed onto the metal, this effect can cause substantial band shifts in the Raman spectra [3, 48, 69]. This charge transfer effect contributes to the increase in signal sensitivity far less than the electromagnetic effect and only occurs when certain types of molecules (usually ones with a lone electron pair) are in contact with the metal nanoparticles.

Chapter 3

Proteins

This thesis involves the investigation of the state of proteins, specifically lysozyme, in different contact lens solutions. In order to fully understand the results presented in this thesis, background knowledge on proteins is first required. This chapter is dedicated to providing this information.

The structures of proteins will first be described, including a basic overview of what proteins are and their function in biological systems. The proceeding section will involve the concept of denaturation of proteins and the varying means by which proteins can become denatured. The forces involved in altering the configurations are also explored. The process of aggregation will then be explained and its relevance to denatured proteins. The final section of this chapter will give information on the particular protein that will be investigated in this thesis: lysozyme.

3.1 Protein Structure

Proteins are large biological macromolecules found in living organisms. They are incredibly important to living systems and can perform a variety of different functions, including performing catalytic interactions, replication of DNA, structural support of cells, transportation of other molecules, immunological and stimuli responses [89]. Most enzymes can be classified as proteins. Enzyme are the biological molecules that can act as catalysts for a certain metabolic process, increasing the rate at which these reactions occur.

All proteins have a similar structure. Fundamentally, they are copolymers, consisting of chains of different monomer species that are unbranched. They are comprised of long

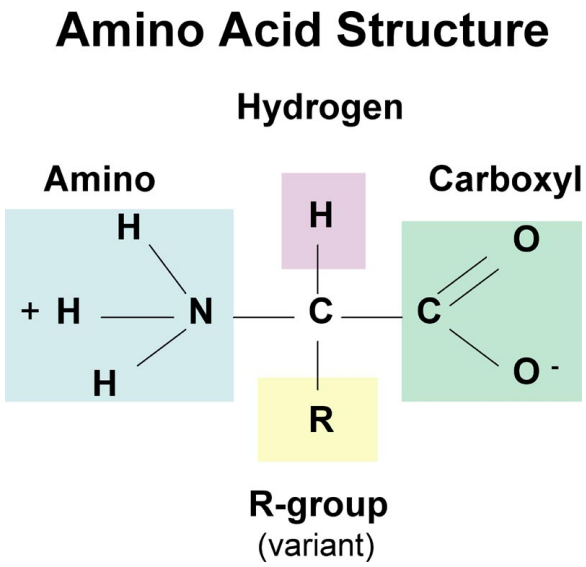

Figure 3.1: This figure depicts the general form of an amino acid. The R group is a certain combination of atoms that specify the type of amino acid [74].

chains of amino acids linked together. Figure 3.1 is a chemical diagram depicting the general composition of an amino acid. Amino acids consist of an amino group, a carboxyl group, a hydrogen atom and a variant R group, all joined together by a central carbon atom. The R group represents multiple different side groups that define the specific type of amino acid. There are a total of twenty different amino acids that the cells of all organisms use as the basis from which to construct proteins. Nineteen of these amino acids have the same general structure, with a variable R group. The exception is proline, which differs slightly in its chemical composition by having a ring structure which includes the central carbon atom.

All amino acids can act either as a base or acid, depending on the particular environmental conditions. The different R side groups provide each amino acid with their individual properties. Some side groups can be either nonpolar or polar, the latter of which can have a net positive or negative charge. Some side groups contain functional groups that may react with other regions located in the same protein, or they may react with external molecules. The variety of properties and functions that proteins can have are dependent on the kinds of amino acids present. The locations of these amino acids within the protein structure also affect the molecular properties. The variability in the specific arrangement of the amino acids to form a protein allows for a large amount of different proteins to exist.

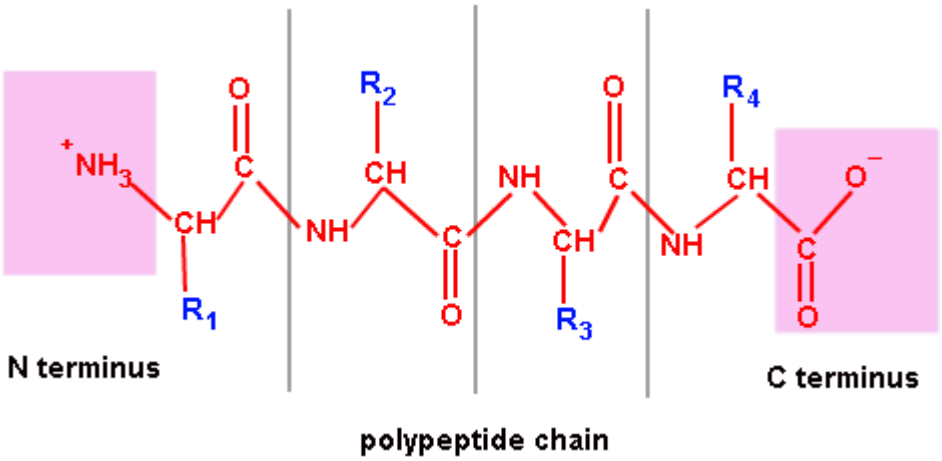

Figure 3.2: Diagram of a polypeptide chain, with N-terminal and C-terminal ends, made of amino acids joined together by peptide bonds [76].

The amino acid chains in proteins can combine and fold into three dimensional structures that determine the properties of the protein. These structural components of a protein molecule can potentially have four different levels of organization, called the primary, secondary, tertiary, and quaternary structures. All levels of structure are used to define the properties of the protein. Each level can produce separate characteristics in the protein and add to the complexity of the structure.

The primary structure is defined simply as the unique sequence of amino acids linked in a particular chain. Amino acids are linked together by covalent bonds, called peptide bonds, between the carboxyl group of one amino acid and the amino group of another. The chain formed is called a polypeptide chain and will have an amino group at one end, called the N-terminal end, and a carboxyl group at the other end, called the C-terminal end, as shown in figure 3.2. The repeating sequence of the amino group, central carbon atom, and carboxyl group make up the backbone of polypeptide chains.

This sequence of amino acids is incredibly important to the function of the protein. The alteration of even a single amino acid in a polypeptide chain can affect the higher structural properties and completely destroy the biological activity of the protein. The primary structure is the fundamental factor that will allow the protein to fold into different three dimensional structures and interact with other molecules [89].

The secondary structure of a protein involves the folding of segments of the primary structure into stable arrangements. A single polypeptide chain may contain several types

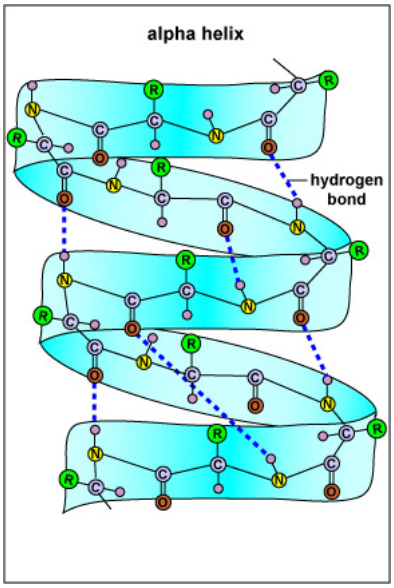

Figure 3.3: Diagram of an α helix structure. The side groups extend outward from the twisting shape of the backbone [77].

of secondary structures at different locations in the chain, depending on its amino acid sequence. Two important secondary configurations are the alpha (α) helix and the beta (β) sheet. These are very stable structures that are resistant to bending. Another secondary structure is called the random coil or loop, and allows the chain to bend at certain flexible regions.

The geometrical arrangement of an α helix involves the backbone of the amino acid chain twisting into a spiral, as shown in figure 3.3. These structures act like rigid rods with the side groups extending outward from the helix. They can behave in either a hydrophobic or hydrophilic manner depending on the particular amino acids that comprise the α helix. The helical structure is stabilized by hydrogen bonds between backbone amino and carboxyl groups in a periodic fashion.

A β strand configuration occurs when the amino acids are arranged in a zigzag pattern in a flat plane. Multiple β strands, either from different regions of a polypeptide chain or from a complete separate chain, may become aligned, side by side, with each other to form a β sheet structure. Figure 3.4 shows a β sheet, in which β strands are stabilized together by hydrogen bonds between the adjacent β strands. The side groups then extend above or below the sheet.

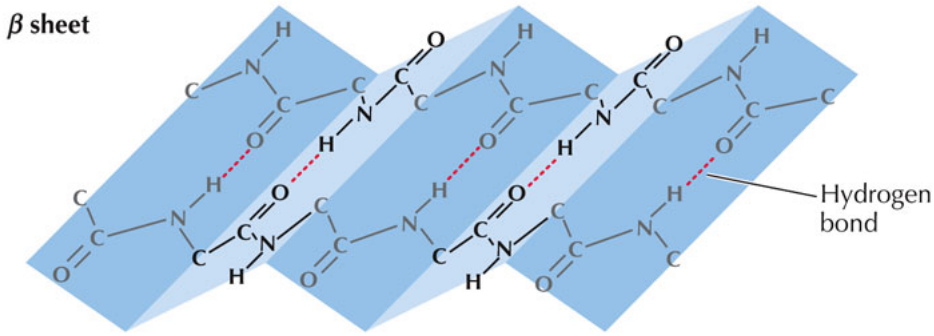

Figure 3.4: Diagram of a β sheet structure, comprised of adjacent β strands joined together by hydrogen bonds [23].

There are two types of sheets that may form: parallel and anti-parallel. Parallel sheets are formed from β strands that are in same direction, with respect to the C-terminal and N-terminal ends of the amino acids. Anti-parallel sheets, conversely, are comprised of β strands oriented in the opposite direction as one another. These β sheets may form into a flat plane or twist into a barrel structure [65].

A random coil arrangement is the irregular folding of the polypeptide chain. This results in the amino acids being randomly orientated, while still bonded to adjacent amino acid units. This definition implies that a random coil is not a particular pattern or shape, but rather a statistical distribution of all the possible arrangements of a chain. However, since amino acids between different segments of the proteins may interact, the statistical distribution of arrangements will be energy dependent. This means the system will favour configurations with lower energies associated with them.

Random coils allow for flexibility and can provide sites for α helix and β strand segments to bend and fold onto themselves. The random coil fragments can also act as hinges in which large portions of the protein can move relative to each other. Loops of random coils can frequently appear at the surface of proteins at locations that link α helix or β sheets that are within the bulk of the protein [89].

The tertiary structure of a protein refers to the specific three dimensional conformation of the amino acids of a polypeptide chain. The α helical, β sheet, and random coil segments of the chain may fold into a unique three dimensional shape which is essentially dependent on the primary structure of the chain. The higher order structure of a protein and the chemical properties of the amino acid side groups are mostly responsible for many of the unique properties a protein may possess.

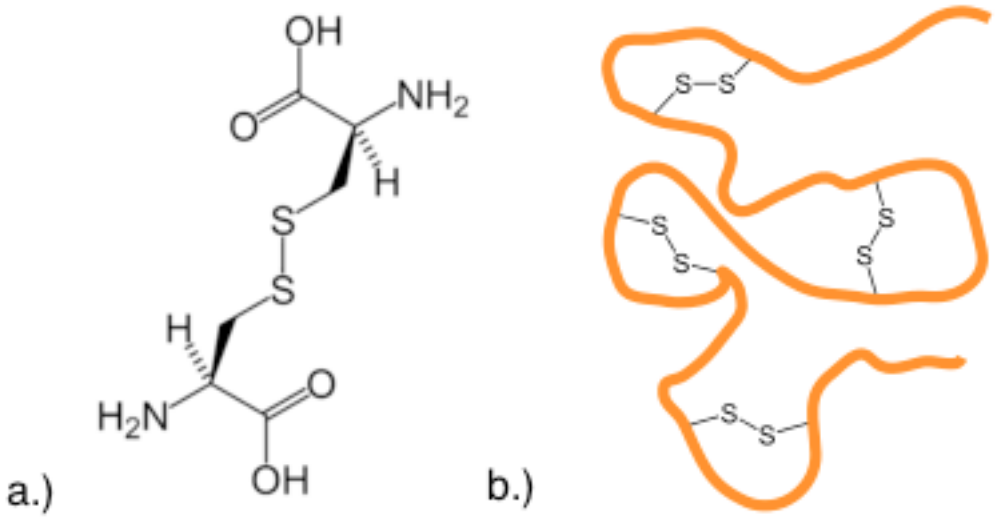

Figure 3.5: Diagram a.) depicts a disulfide bridge between two cysteine amino acids and b.) shows multiple disulfide bridges connecting different regions of a protein together [79].

The tertiary structure is stabilized mostly by different non-local interactions between differently charged amino acids and polar or nonpolar side groups. However, these forces can be complimented by hydrogen bonds as well as salt bridges and disulfide bridges. Disulfide bonds can occur in some proteins between the thiol groups in the side chain of an amino acid called cysteine. Typical disulfide bonds between two cysteine groups, as shown in figure 3.5, are covalent bonds that link separate segments of a protein together. These bonds help to stabilize the protein structure, and thus minimize its mobility. [65].

The interactions that form the tertiary structure can cause for some amino acids to be pushed deep into the bulk of the protein, while others may be forced to its surface. These factors can determine the solubility of a protein. Proteins that are soluble in water usually have polar amino acid side groups congregated at the surface of the protein structure. A common consequence of this phenomena is that the protein will then develop a tertiary structure with a hydrophobic core [89].

This three dimensional configuration of amino acids impacts the biological functionality of proteins. However, the interactions that stabilize tertiary structures are weak. This results in a structure that is not fixed, but instead is flexible and may undergo conformational changes. This variability in the structural configuration can greatly affect the function and activity of proteins [65]. Some proteins may even require a regular alteration in their three dimensional shape in order to properly perform their function. However, under extreme

conditions, a protein may undergo a denaturation process, as discussed further in section 3.2, in which the structural change diminishes the functionality of a protein [89, 65].

The primary, secondary and tertiary structures all describe the configuration of an individual polypeptide chain. The quaternary structure describes how multiple amino acid chains may combine in a specific arrangement to form a single protein complex. A type of protein found in many living cells, called chaperonins, help to guide the assembly of multiple chains in the formation of some proteins. The bonds and interactions that allow this higher order structure to occur are the same forces that determine the tertiary structure. These mainly include hydrogen bonds, disulfide bridges, as well as polar and non polar interactions [89].

The occurrence of large distinct structures formed by the folding of amino acid chains are common amongst a variety of different proteins. These subdivisions of the protein complex are called domains. Usually the domains of a protein are connected by flexible random coils. This allows the domains to freely move with respect to each other, with these random coils acting as hinges. This property is common in enzymes and other motor proteins. The individualistic nature of domains can be very important in the function of proteins. Some proteins can have multiple distinct functions, each of which correspond to a separate domain in its structure.

3.2 Denaturation

It is well established that the biological activity of a protein is not just dependent on its chemical composition, but also its three dimensional configuration of its constituents. Most proteins will naturally exist in a very limited number of closely related stable conformations, called the native state, in which their activity is preserved. This native state is usually the one with the lowest energy, thermodynamically, which is determined by the primary structure of the protein. However, even slight changes in the structural conformation of a protein may result in a complete inability to perform any of its normal functions [65].

This leads to the important concept of denaturation. A protein can become denatured when it is subjected to certain environmental conditions that cause for structural changes, and thus a loss of functionality. Biological molecules will lose their activity when denatured. Enzymes, for example, have particular regions in their structure, called the active sites, in which a substrate will bind in order for the enzyme to perform some interaction. The substrate of an enzyme is simply the particular chemical species onto which the enzyme will perform its unique function. If the structure of an enzyme is altered, the active site

may change enough so that the substrates cannot bind. This, of course, means the specific amino acids that are involved in the enzymatic reaction can no longer interact with the substrate.

Denaturing can result in changes of the quaternary, tertiary or even secondary structures of a protein. The subunits of a protein may become misaligned, resulting in changes in its quaternary structure. Further denaturation may result in alterations to the tertiary structure. These changes are a consequence from disruption of the covalent bonds between amino acids such as disulfide bridges. Non-covalent interactions between the polar side groups of amino acids and the surrounding solvent can also cause for these structural alterations. The van der Waals forces between the nonpolar side groups may even be interrupted. The damages to the secondary structure of a protein as a consequence of denaturation results in the ordered patterns of α helices and β sheets to instead form random coils. Denaturation, conversely, does not affect the primary structure of a protein.

One factor that may result in the denaturation of proteins is an exposure to large amounts of heat or radiation. High temperatures may break down the hydrogen bonds that bind a protein to its native configuration. The protein may then unfold preventing any biological activity. This is one of the main reasons that most living organisms cannot survive at even relatively warm temperatures [65].

The denaturing of a protein may also result from another important cause, in which the protein is exposed to different chemical environments. Chemicals, including organic solvents such as alcohol or chloroform, concentrated inorganic salts, or acids and bases can all have great effects on a protein. A change in pH can result in an alteration of the charges of the amino acid side groups, as well as disruption of ionic bonds in a protein. Many chemicals can denature proteins by weakening the non-covalent interactions that are responsible for stabilizing the native state of the protein. Certain reducing agents, in particular, can be used to break disulfide bonds. A collection of highly ordered and identically folded proteins may be reduced to an entropically favoured ensemble of different unfolded states that are biologically inactive [89, 65].

The process of denaturation may be either reversible or irreversible. Many proteins, once denatured, become permanently inactive and cannot resume their native state when removed from the source of denaturation. A common example of this phenomena is the cooking of an egg white. The native form of the proteins present in the egg white (mostly albumin) form a clear solution. However, when heated, the substance is converted to a white, insoluble solid which will not return to its original state after the heat is removed (although egg whites may be uncooked when vitamin C or sodium borohydride is introduced). This is because the proteins have unfolded and interacted with each other causing

for large clumps of protein to form. The egg turns from a transparent gel to a white substance because these larger protein clumps scatter light more effectively than the original protein molecules, which were initially smaller than the wavelength of light.

There are some proteins, in contrast, that may return to a native state when the denaturing factor is removed, such as a return to a normal temperature or pH value. This process, called renaturation, of spontaneously refolding back to a biologically active state is somewhat curious when entropy is considered. This seems to indicate that all of the information required for the specific folding of the polypeptide chains of a protein are encoded into its primary structure. It has also been shown that this folding pathway may occur in a series of steps [65]. A main element that allows for renaturation are the disulfide bonds in enzymes, which help to inhibit the degree to which the proteins unfold [89].

Theoretically, all individually isolated protein molecules should be able to refold back to the native state because this represents the lowest energy configuration. Any denaturing that occurs results in an energetically unfavourable conformation. However, irreversible denaturing essentially occurs due to protein-protein interactions that prevent the refolding of the molecules, as discussed further in section 3.3.

3.2.1 Forces Affecting Protein Configuration

There are several different mechanisms by which a protein can interact with itself as well as its environment. These means of interaction provide forces that will encourage different folding configurations of the protein molecule. Some of the mechanisms include hydrogen bonding, van der Waals forces, electrostatic interactions, covalent bonding and thermal fluctuations. These factors are all essential to protein-protein, residue-residue (protein-self), and protein-solvent interactions. Most intermolecular forces have electromagnetic foundations, however, entropic considerations can also play an important role.

One of the factors that contributes to the uniqueness of each protein complex is the variety of non-polar, polar groups, and charged side groups of the amino acids. These groups can be present at different regions of the same protein molecule and help to provide intermolecular and intramolecular forces [26]. Charged amino acid residues usually inhabit the exteriors of the protein complex, allowing for association with the surrounding environment. Many of the charged groups may act as a buffer due to their weak acid and base capabilities.

Water is an excellent solvent for proteins that have exposed charged and polar groups on their surface. When these proteins are instead introduced to electrolytes, electrostatic interactions are minimized. This is a result of an ionic double layer that forms, which

causes the expansion of the protein by reducing ion-ion interactions. Ions that are within the interior of the molecule, as well as on the surface, will commonly help to stabilize the protein configuration by pairing with other ions of opposite charge [105].

This internal charge pairing, however, does not dictate the structural conformation due to hydration of the ions from surrounding water molecules. The non-ionized groups that reside in the interior of the molecule will strive to become ionized, and will thus assist instead in the unfolding of the protein. The final effect of charged groups to favour either the folding or unfolding of the complex will be dependent on the pH, concentration of electrolytes, and charge distribution among the molecule [102].

The van der Waals forces involved in the high density of proteins when packed together are considered to be favourable to folding. This is also the case for hydrogen bonds, which occur between the external water molecules and particular side groups in the protein. The general conclusion made is that both of these types of forces are complementary and supportive in the stabilization of the folded protein. They are not, however, the primary causes for the compaction of the molecule [105].

The folding of proteins may result in the bending of bonds in an unfavourable manner. Entropy is of course reduced due to the restrictions of the bond rotations when folded. The bond angles and lengths may also be constrained to an energetically unfavourable position. These mechanisms will result in a tendency for the unfolding of the molecule. The hydrophobic interactions of the protein are usually assumed to be the main forces that cause folding. Non-polar groups in the protein can result in a disturbance of the hydrogen bonding between water molecules. These groups do not participate in hydrogen bonding with water, and thus the water molecules are forced to reorganize around the protein to still maximize the possible hydrogen bonds made (on small scales). The amount of order caused by water molecules having to rearrange around the non-polar groups is much more than the order gained by the non-polar groups folding to the interior of the protein. This means the loss in entropy caused by reordering the water molecules greatly surpasses the loss from compacting the non-polar groups. Thus, by entropic considerations, the folding of the protein in an aqueous solution into a more compact arrangement is favoured [105].

3.3 Aggregation

Protein aggregation, as a biological concept, is the accumulating and clumping together of unfolded proteins. This is depicted in figure 3.6. The aggregation of proteins can be extremely toxic in living organisms and has even been linked to numerous diseases

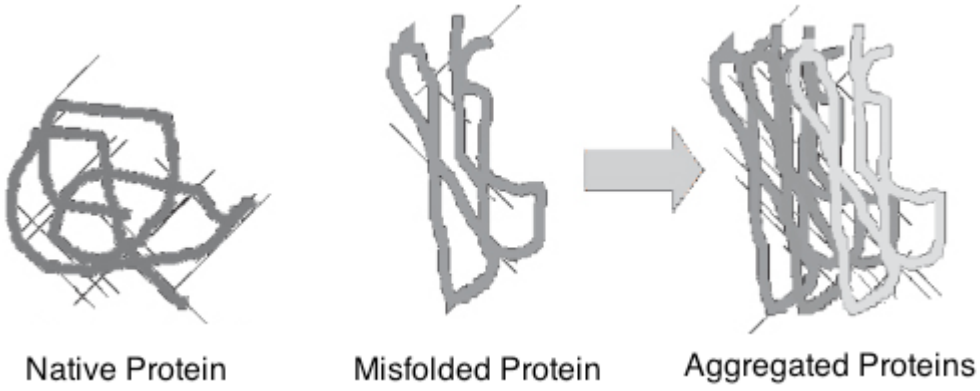

Figure 3.6: This figure shows protein aggregation. This occurs when several protein molecules clump together after they have unfolded [85].

[27]. As discussed in section 3.2.1, the three dimensional folding of the polypeptide chains that a protein consists of usually fold due to a hydrophobic effect. This occurs when the hydrophobic (non-polar) regions of the chains are forced to the interior of the structure, while the hydrophilic (polar) sections of the protein are left exposed to the exterior of the molecule.

However, under certain conditions, the proteins may not fold properly when first produced. They may even become misfolded after already being correctly formed to the native state. This is a result of the protein being denatured by a variety of causes, as discussed in section 3.2. When multiple proteins become unfolded and denatured, they may aggregate together. High salt concentrations can possibly cause for the screening, or minimization, of the charged regions of proteins. This decreases both the attractive and repulsive forces amongst proteins which may lead to aggregation.

Aggregation can be generally attributed to the fact that when most proteins become unfolded, the normally hydrophobic interior becomes exposed to the environment. These portions of the protein may then interact with the exposed hydrophobic regions of other proteins that have also become denatured. This can consequently lead to the spontaneous clumping of denatured proteins [41].

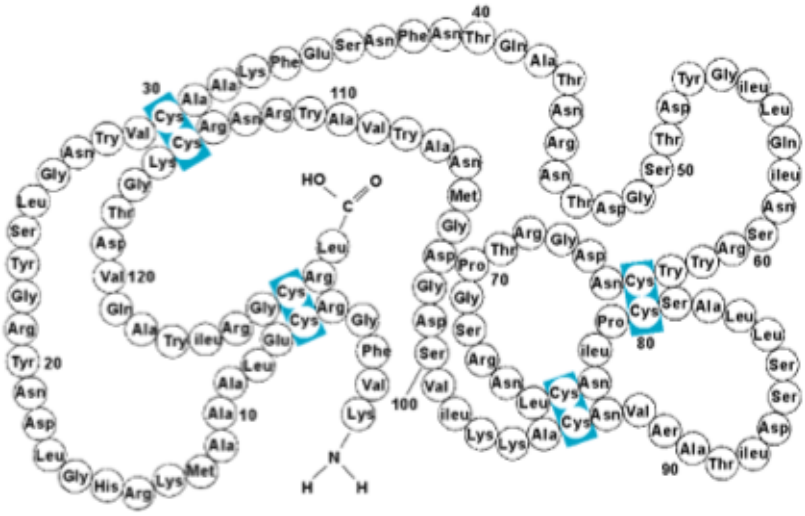

Figure 3.7: This figure depicts the primary structure of lysozyme. The locations of the four disulfide bridges are indicated by the blue boxes [82].

3.4 Lysozyme

Lysozyme is a common mammalian enzyme and can be found in most biological secretions, such as milk, saliva, tears, kidneys, urine, and cervical mucus [34]. One of the main purposes of lysozyme is to act as a digestive enzyme in immunological responses and can help to destroy the cell walls of certain bacteria.

3.4.1 Structure

The three dimensional structure of lysozyme slightly resembles an ellipsoid with a molar mass of approximately 14.5 kDa [11]. It is composed of a polypeptide chain of 129 amino acids that fold into a relatively small, compact shape with dimensions around $4.5 \times 3 \times 3nm$. There are four disulfide bridges that cross link the amino acid chain [89]. Lysozyme has a large net positive charge accumulated on its surface. This charging is due to three separate collections of closely positioned basic amino acids. The primary structure, as well as the disulfide bridges of lysozyme, are shown in figure 3.7.

There are five helical segments that are formed by the folding of the polypeptide chain. An anti-parallel β sheet, made of three β strands, act as one wall of the active site. This active site is a deep cleft that is used to mark the division of the molecule into two different

domains. One domain has helical structures, while the other has β sheet regions. These two domains are connected by α helical residues [34]. Figure 3.8 shows a diagram of the three dimensional structure of lysozyme in which the secondary structures are visible.

There are two separate regions of lysozyme that have activity dependent on two different antigens. Antigens are molecules that generate an immune response in a living organism. Lysozyme thus has two different fragments that may bind to antibodies which are involved in destroying the lysozyme in an immune response. One of the segments which has immunological activity involves the two amino acids that comprise the N-terminal and C-terminal ends of the lysozyme amino acid chain. These two peptides are bonded by a disulfide bridge. The other fragment of the lysozyme that is independently immunologically responsive contains two different disulfide bonds. This region is located in between the Leucine 57 and Arginine 107 amino acids in the lysozyme polypeptide chain [2].

3.4.2 Function

As previously mentioned, lysozyme has multiple functions, that include immunological activity. A particularly important function of lysozyme is its ability to destroy certain types of bacteria. A common feature of these bacteria is the presence of a thick outer cell wall comprised of peptideglycan. This is a polymer made of sugars and amino acids that form a network that encompasses the cell membrane. The tertiary structure of antibacterial lysozyme has an active site formed by a cleft in the structure [89]. The peptideglycan of the bacteria cell walls can bind to this active site in the lysozyme molecule, in which this polysaccharide can be broken apart.

The activity of this enzymatic reaction is due to the presence of two amino acids in the active site, glutamine and aspartic acid. The carboxylate groups in these amino acids can trigger the hydrolysis of the substrate. This catalytic reaction involves several steps that eventually leave the lysozyme molecule unchanged, while bonds of the bacterial polysaccharide are broken. This results in the substrate to be cut into smaller portions and thus the integrity of the bacteria cell is destroyed [100, 34].

3.4.3 Human and Hen Egg-White Lysozyme

Fortunately for the convenience of lysozyme studies, human and hen egg lysozyme have secondary structures that are very similar. Both x-ray crystallography [8] and far-UV circular dichroism [42] techniques have been used to show this relationship. These two types of lysozyme do not, conversely, have the exact same sequence of amino acids in their

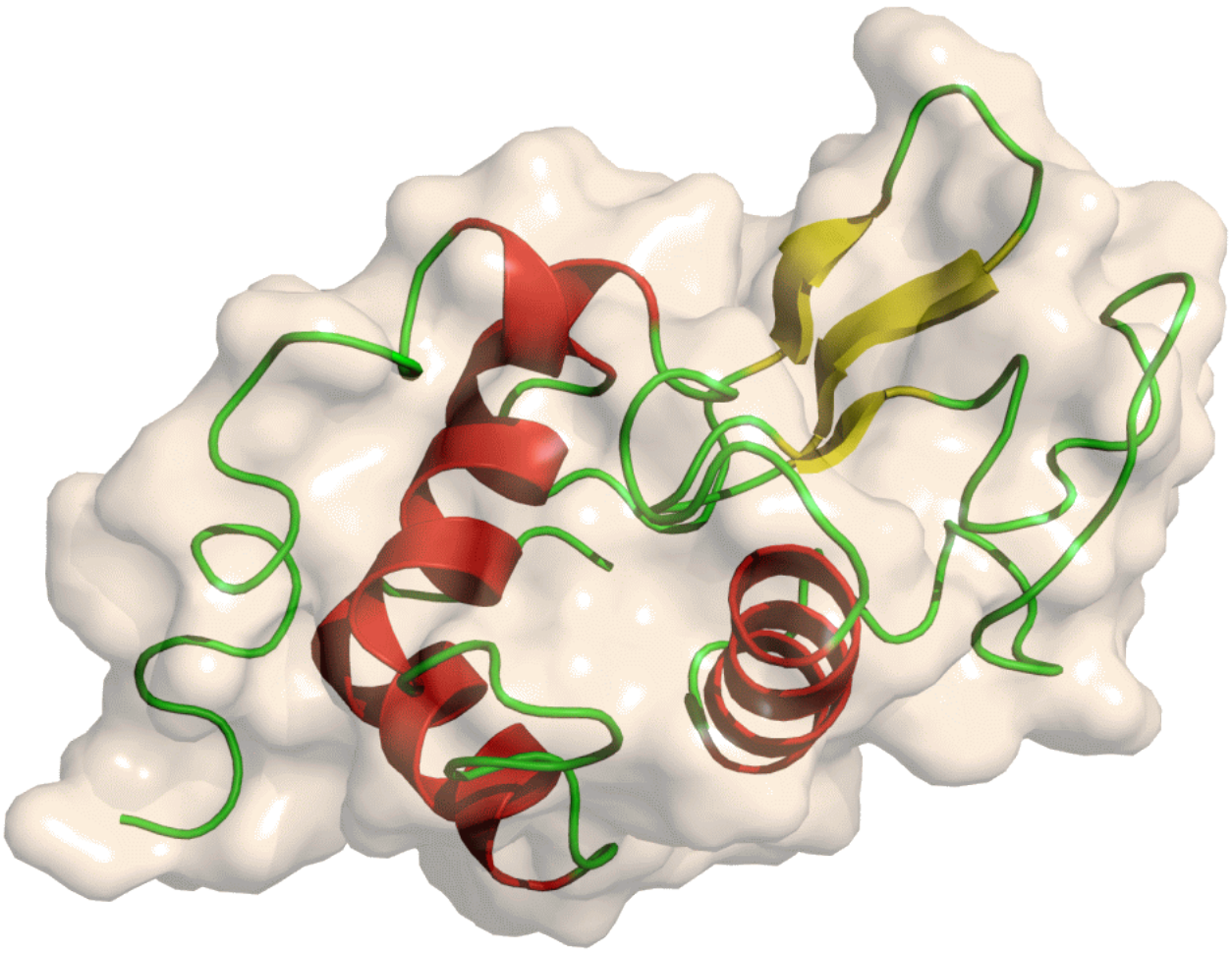

Figure 3.8: This figure depicts the three dimensional structure of lysozyme, in which the secondary structures are visible [111].

primary structure. In fact, hen egg-white lysozyme has 129 amino acids that make up its polypeptide chain, while human lysozyme only has 125 amino acids [42].

However, there are large portions of the amino acid sequence that are identical between the two. The alterations of amino acids in the chain sequences of the two molecules are also mostly conserved. This essentially asserts that the substituted amino acids have a similar polarity in their side groups. Consequently, the structure and functionality of the two lysozyme molecules are comparable [34]. The activity of these enzymes were also found to be highly similar in solutions with a constant ionic strength within a pH of 5 to 9 [100]. These factors all contribute to the general consensus that hen egg-white lysozyme is a suitable substitution for modelling human lysozyme in research applications.

3.4.4 Denaturation of Lysozyme

Lysozyme is a relatively robust and stable protein that does not denature easily. There does not seem to be a singular unique denatured state of lysozyme, in which the alteration of its native state may result in a variety of different configurations. However, most modifications due to the denaturing process result in a random coil configuration of the molecule [87]. A common factor that is exploited in chemical denaturing mechanisms is the breaking of disulfide bonds, allowing the structure to unfold [18].

Its properties are mostly consistent at a range of acidity from a pH of 1 to 8 [84]. Studies have also shown that the denaturing of lysozyme only occurs at values greater than a pH of 12 [46]. A variety of different chemicals have also been shown to denature lysozyme at different concentrations, such as dimethyl sulfoxide, LiBr, guanidine HCl, sodium dodecyl sulfate, and urea [87]. However, high concentrations of organic salt does not seem to not effect the helical part of the molecule [100].

Lysozyme may also be denatured by means of thermal heating. Studies have shown that the possible denaturation temperature of lysozyme in an aqueous solution occurs at approximately 76°C in which the disulfide bonds begin to rupture. For temperatures below 76°C, the only conformational changes that occur are attributed to the side groups and the internal folding of the molecule [100, 17]. Optical rotatory dispersion as well as proton magnetic resonance has been used to show that lysozyme may undergo reversible denaturation between the temperatures of 68 and 76°C in an aqueous solution of pH 5-6.

It is also known that above a temperature of 80°C, lysozyme will undergo irreversible denaturation. The reaction rate of this process will depend on other factors in addition to the temperature. This denaturation has been observed to involve disordering of the

backbone of the polypeptide chain [17]. All four disulfide bridges have also been shown to be destroyed at temperature greater than 76°C [12].

Chapter 4

Motivations for Contact Lens Research

The research performed in this thesis involves investigating the denaturation of lysozyme when exposed to several contact lens solutions. This chapter will be devoted to explaining the importance of studying the state that protein is present in while dissolved in these solutions. The first sections of this chapter will give a brief overview of contact lens materials presently used, as well as some of the contact lens solutions available. The latter parts of this chapter will explain why certain solutions may not be optimal, in addition to clarifying the hazards involved when lysozyme becomes denatured and reintroduced to the eye. The final sections will describe the relevance of lysozyme, in particular, to the research in this thesis.

4.1 Contact Lens Materials

Contact lenses have become one of the most prominent applications of biomaterial technology to date. This assertion has provoked a great amount of research into the different materials used for eye care, as well as their effect on the body [53, 50, 100]. Contact lens materials can be broadly divided up into two main types, soft, water-containing, hydrophilic materials called 'hydrogels', and non-water containing rigid gas permeable (RGP) materials.

Hydrogel contact lenses account for the material of choice for about 90% of consumers due to their ease of fit for practitioners and initial greater comfort [83]. The polymers that

comprise the hydrogel materials are hydrophilic. This allows for the lens to absorb large amounts of water, making them flexible and permitting the rapid adaptation. Oxygen transport though the material to the cornea occurs through this water phase and is an important feature of a lens material. However, oxygen is not an efficient transporter of water and some of the early hydrogel materials suffered from low oxygen transport capabilities [36]. These lenses may cause hypoxia and corneal edema effects in the eyes of patients, particularly ones with higher metabolic requirements in the cornea [60].

The relatively recent introduction of a new family of hydrophobic lens materials termed "silicone hydrogels" (SiH) lenses have allowed for a combination of the comfort, wettability, and vision advantages of hydrogels with an increase in oxygen permeability due to the incorporation of siloxane macromers. The use of SiH lenses has continued to grow over recent years and they now represent approximately 66% of all soft lenses prescribed (while about 24% of lenses are the conventional hydrogels) [83]. SiH lenses do not rely on the water content for oxygen delivery, but rather transmit oxygen through the siloxane components of the material.

The problem of not providing enough oxygen to the corneal surface has been mostly resolved with the introduction of SiH lenses. SiH lenses have been shown to transport 5 or 6 times more oxygen than the conventional hydrogel lenses that based on Polyhydroxyethyl methacrylate (polyHEMA) material [49]. This increase in oxygen availability is particularly beneficial for patients with long periods of wearing contact lenses and ones who have prescriptions with thicker lenses [36]. These factors have all contributed to the wide use of SiH lenses and its overwhelming preference over other competing materials. The advantages of using SiH will mostly likely see continued growth in their prescribing rates. The problems that arise with these lenses, however, will be discussed in sections 4.3 and 4.4.

4.2 Contact Lens Solutions

A great deal of research has been undertaken on contact lens solutions. There are many different solutions available, and their selectivity can depend on a variety of factors, such as the lens type used, cost, as well as patient and practitioner preference.

The primary function of these solutions is to disinfect the contact lenses. This process is required in order to destroy any harmful micro-organisms so that the lens may be safely reinserted into the eye [50]. This role is undertaken by an antimicrobial agent or biocide that is included in the composition of the solution. The specific agent used must take into account efficacy, safety and convenience [53]. There are multiple pathogens that need to be killed by this agent, however, it must also not be harmful to the ocular tissue.

The other main function of any contact lens solution is to clean the surface of the lens from any components from the tear solution that are deposited, such as proteins and lipids. This function is usually achieved by the surfactants that are present in the contact lens solution. Surfactants are molecules with a polar hydrophilic (head) and nonpolar hydrophobic region (tail). These act as detergents to remove deposits and debris on the lens. This mechanism of cleaning the lens involves the surfactant molecules combining with the deposit to form a micelle (a spherical aggregate) which can then become suspended in the surrounding solution. The secondary function of surfactants is to increase the wettability of the lens, which is particularly important for the relatively hydrophobic silicone hydrogel lenses.

In addition to these functions of a contact lens care regimen, there are many other characteristics that will make a particular solution ideal for lens care. These factors include the need for the solution to be biocompatible when in contact with the ocular tissue, as well as increase wettability and comfort of the lens [53].

The two main types of contact lens solution that are readily used by patients are the preserved multipurpose (MPS) disinfecting solutions and the non-preserved hydrogen peroxide-based solutions. In the mid-1990s hydrogen peroxide systems represented almost 45% of all solutions prescribed [50]. However, this figure has rapidly decreased as many new MPS were developed and they accounted for >90% of prescribed solutions while hydrogen peroxide systems were <5% in the UK for 1996-2005 [75]. However, recent years hydrogen peroxide-based systems have increased in prevalence and currently represent about 24% of the solutions prescribed, while MPS have dropped to about 76% [83]. This apparent shift towards a higher usage of hydrogen peroxide systems over MPS may be due to ocular health concerns seen as corneal staining, which will be further discussed in section 4.3.

4.2.1 Hydrogen Peroxide Systems

Hydrogen peroxide systems disinfect soft lenses by utilizing a 3% (30,000 ppm) concentration of peroxide. The main benefit of these systems are their incredibly high efficiency rates at destroying micro-organisms found on lenses and that they are 'preservative-free' following their neutralization. These hydrogen peroxide systems are considered the 'gold standard' for the disinfection of lenses [50].

There are many different microbes on the surface of the lens that may need to be killed before lens reinsertion. This is accomplished by hydrogen peroxide due to its strong oxidizing capabilities. This allows for many different components of the microbial cells to be disrupted, such as its proteins, lipids, and DNA, which will result in cell death.

Following lens disinfection and prior to insertion of the lens, the solutions has to be neutralized to prevent the peroxide damaging the ocular tissues. This can ensue even at the relatively low concentrations of these hydrogen peroxide systems and must be neutralized, depending on the method, to a concentration of approximately 50 to 300 ppm. There are natural mechanisms in the cornea that can convert these remaining low concentrations to water and oxygen [16].

Originally, hydrogen peroxide systems used a two-step process to neutralize the solution. This system involved exposure of the lens to the 3% peroxide solution overnight, followed by neutralizing the lens only just prior to usage. The neutralization was performed by extensive rinsing in dilution agents (such as saline) or a neutralization solution. This system provided very high efficacy for microbial kill, as the lenses were left in 3% peroxide for many hours. However, several factors have lead to their decline in use, such as cost, lack of convenience, and patient failure to remember to neutralize before insertion [53, 50].

Within the past 10 years, one-step hydrogen peroxide systems have become the most popular means of neutralization worldwide. There are two methods that have been developed for one-step systems in which a neutralizing agent is added at the beginning of the disinfection cycle. One system involves using a catalytic platinum disc to slowly neutralize the solution by a chemical reaction over time, such in the produce ClearCare®. The platinum-coated disc breaks down the hydrogen peroxide into water and oxygen. This reaction results in an initial neutralization that is rapid, occurring within the first few minutes. This is followed by a slow transition to a concentration of approximately 15ppm of peroxide after 6 hours [21].

The other method of neutralization introduces a tablet that uses a time dependent release of an enzyme, called catalase, which neutralize the solution. This method is utilized in the peroxide-based system called UltraCare®. This tablet is coated with hydroxypropyl methyl cellulose (HPMC) and will slowly dissolve away when added to the solution. The catalase it encloses can then be released to neutralize the solution after a certain amount of time. This coating is designed to dissolve at such a rate that will ensure the hydrogen peroxide is greater than 1% during the first 20 minutes. After approximately 2 hours the peroxide concentration is reduced to 1ppm. The HPMC also may act as a surface wetting agent for the lens. There is a pink dye incorporated to the tablets in order for the patient to confirm that it has been added to the contact lens solution [50].

The two brands of hydrogen peroxide systems investigated in this thesis are ClearCare and UltraCare, which are both 3% peroxide solutions. However, prior to neutralization UltraCare is at a lower pH of about 3.33, while ClearCare is at a pH of approximately 6.53. Interestingly, the pH of the two systems following neutralization is about 6.67 for

ClearCare, and 7.18 for UltraCare [25].

These one-step systems have a theoretically decreased ability for disinfection over the two-step systems, as the lens is exposed to the peroxide solution with the two-step systems for much longer. However, one-step systems are still considered safe and efficient at disinfection, with little or no apparent reduction in efficacy [53].

4.2.2 Multi-purpose Solutions

All multi-purpose solutions (MPS) contain a disinfecting agent or biocide that have generally the same mode of action when destroying microbes. These agents cause cell death by interacting and disrupting the cellular membrane. The biocides in most MPS are biguanides, polyquaternium-1 or other disinfectants such as myristamidopropyl dimethylamine. Tests have shown that hydrogen peroxide is almost always more effective at destroying microbes than MPS systems [45]. However, the antimicrobial agents in MPS are not eliminated or neutralized following the disinfection cycle, as in hydrogen peroxide systems, and thus can provide disinfection over long periods of time which otherwise may allow for regrowth of micro-organisms. Thus, MPS are the only viable option for patients who wear their lenses on a part-time basis.

Polyhexamethylene biguanide (PHMB) is an active disinfectant in many MPS such as ReNu® and BioTrue®. Currently, the lowest concentration of PHMB in an MPS available is in B&L's ReNu® Multipurpose, which also has a Tetronic-based surfactant. The chemical PHMB can bind to the negatively charged phospholipids in the plasma membrane of the microbe, which can weaken or rupture the membrane [53]. Fortunately, PHMB has no damaging effect on the ocular cell membranes [50].

There are several different chemicals present in contact lens solutions that may interact with each other to either improve disinfection effectiveness or increase the removal ability of tear film components, such as proteins, from the lens. Many MPS products contain high concentrations of surfactants that reduce the surface tension of the liquid considerably. Many of these MPS agents require a rubbing and rinsing procedure before insertion to reliably remove deposits on the lens.

Another important chemical present in most MPS products is ethylenediamine tetraacetic acid (EDTA). EDTA is a cationic agent that can enhance the activity of disinfectants by binding free metals. This mechanism of enhancement involves aiding ions, such as calcium and magnesium, to bind to active sites of the microbial cell wall. These ions compete against other positively charged preservative molecules and thus the cell walls become more easily penetrated by these preservatives [53].

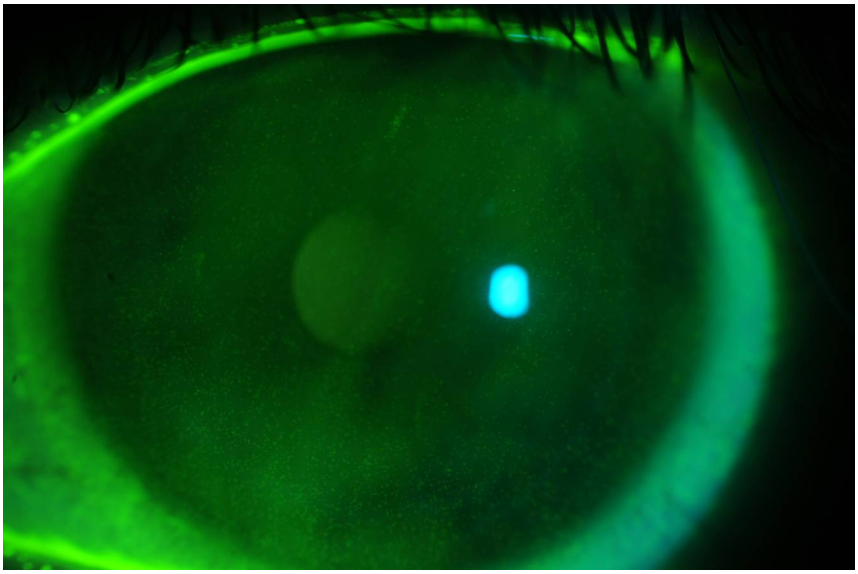

Figure 4.1: This is an image of a patient with corneal staining induced by a multipurpose solution [68].

4.3 Corneal Staining

One of the main concerns currently related to contact lens research and solution systems is the issue of solution-induced corneal staining (SICS), as shown in figure 4.1. Corneal staining occurs when a synthetic organic compound used to investigate the integrity of the cornea, called fluorescein, either penetrates the membranes of damaged ocular cells or enters gaps between the epithelial surface [63]. These gaps are due to dislodged cells or cells that have been somehow disrupted.

There are different degrees of corneal staining that may occur. The staining is mainly attributed to causes such as dryness, dehydration, tear film deposits, foreign substances, lens surface abnormalities, hypoxia and contact lens solutions [50].

The first cases showing a difference in corneal staining due to contact care regimens occurred in the mid-1990s. It was shown that there was less staining caused by hydrogen peroxide systems than for PHMB-based preservative systems with the use of conventional polyHEMA-based lenses [98]. It was additionally shown that patients who used contact lens care systems that involved the highest levels of preservatives showed the greatest amount of corneal staining. Some of these findings discovered links between the staining occurrence and both the lens material used as well as the care regimen [52].

Research investigating the link between corneal staining and solutions has become incredibly important in the recent decades. This is partly due to the rise in the usage of SiH lens materials, as discussed in section 4.1, which can provide a number of benefits over conventional hydrogels. However, several studies have suggested that the use of SiH with particular lens care systems can result in excessive corneal staining, compared to other conventional lens material [28, 33, 39, 49, 112].

There are several sources that have investigated corneal staining for the variety of combinations of contact lenses and contact lens solutions. One of the clear results is the increase in staining when using SiH lenses with MPS rather than hydrogen peroxide [37]. MPS systems have also been shown to produce corneal epithelial damage when exposed to the eye [20, 39]. This is simply attributed to the ability of the SiH lens to uptake the MPS preservatives and thus introduce these chemicals to the ocular tissue, potentially causing toxic and allergic effects in the cornea [37]. These results may explain the steady increase in the prescribed usage of hydrogen peroxide systems rather than MPS in the recent years.

4.4 Relevance of Lysozyme in Contact Lens Research

A major disadvantage of soft lens materials over rigid materials is that there can be a substantial uptake of tear solution components onto and into the lenses, such as proteins, lipids and mucins [100, 36, 37]. Large accumulations of the substances on the lenses can result in a reduction of vision clarity, increased dryness, discomfort and hypersensitivity [51]. These deposits can also increase the potential harm done by bacteria, by operating as a shelter and microbes may attach to the substrate [100]. There are several complex interactions that determine the amount and types of tear film deposits that may be absorbed by a lens.

The source of protein deposition on contact lenses is from the tear film. The proteins originally form a thin invisible film on the surface of the lens, which may become a thin, opaque, whitish film as the proteins denature over time. There are many different types of protein that are in the tear solution, and each are capable of depositing onto the lens. However, the degree to which these proteins can bind can depends on several factors, such as the charge and size of the protein, pH and water content environment, as well as competition between other tear film constituents [9]. The main proteins that have been detected on hydrogel contact lenses include lysozyme, lactoferrin, and albumin [67]. Table 4.1 lists the most important proteins in tear solution and their average concentrations. Lysozyme, however, is the most prominent protein present in tear solution [5] at a concentration of

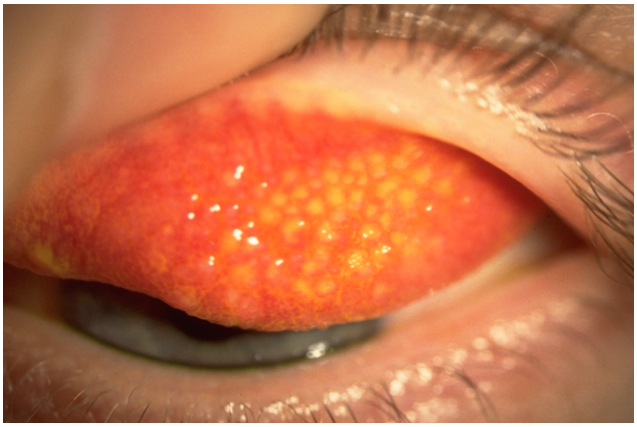

Figure 4.2: This is an image of a patient with giant papillary conjunctivitis (GPC) [37].

roughly 2 mg/ml, and extensive research has been done on the deposits of this protein on contact lenses [14, 100, 67].

Protein	Average Concentration (mg/100ml)
Lysozyme	236
Lactoferrin	184
Tear Specific Pre-albumin	135
Albumin	130
Immunoglobulin A	30
IgG	12.6
IgM	0.086
IgE	0.01

Table 4.1: This table gives the average protein concentrations in tear solution [5].

If protein, particularly lysozyme, is deposited onto the lens, then over time the ocular tissue is exposed to this. Problems with this exposure arises when the protein is denatured. Proteins that are denatured are not only harder to removed from the surface of the lens, but they may cause an immunological response called 'giant papillary conjunctivitis' (GPC) [32], as shown in figure 4.2. GPC is essentially an allergic response of the under-surface of the eyelid in which the body treats the denatured proteins as foreign objects and triggers an immune response. This is a syndrome that occurs on the upper tarsal conjunctiva (inside of the eyelid) in which the tissue may be roughened and the conjunctiva may become dilated and inflamed. GPC can be characterised by complex symptoms related to inflammation

and certain anatomical changes [31]. Specific symptoms of GPC can include discomfort, itching, and increased production of mucus which may result in vision impairment [37].

It has been shown that SiH lenses uptake lower levels of protein than conventional hydrogels [54]. However, studies have shown that a large proportion of proteins deposited on surface of SiH materials become inactive or denatured [101]. The use of SiH lenses has been associated with an increased number of patients developing GPC, potentially due to their increased modulus (or stiffness) and the fact that they deposit increased amounts of denatured lysozyme [94].

4.5 Objectives

As previously discussed in this chapter, SiH lenses are now the most widely used type of contact lens materials and are usually used with MPS or hydrogen peroxide systems. The use of SiH materials with MPS can cause corneal staining due to the uptake of the preservatives in the contact lens solution. This has resulted in an increasing trend of hydrogen peroxide systems being used with SiH lenses, instead of MPS, due to the lack of these preservatives. However, there is a risk of giant papillary conjunctivitis when proteins that are deposited onto the lens material become denatured. SiH materials have already been shown to denature these proteins, and in particular the protein lysozyme, as it is the most common protein in tear solution.

To date, there is a lack of research that investigates the denaturing capabilities of contact lens solutions, and in particular the hydrogen peroxide solutions. If denaturation can be caused by these solutions there is a much larger risk for patients to develop GPC, especially with the use of SiH lenses. Thus, studies investigating the potential for peroxide-based systems to denature lysozyme would be valuable to understand the potential for SiH lens materials to produce an even worse situation than occurs currently when SiH materials are used with MPS.

The research presented in chapter 6 will focus on studying the denaturation of lysozyme in both MPS and hydrogen peroxide contact lens solutions. This will be achieved by using Raman spectroscopy to investigate the structural configuration of lysozyme, which can be used to directly determine if a denatured state is present. There will also be a discussion of data that will determine the functional activity of the lysozyme, which again can indicate if denaturation has taken place. This data will be collected using a micrococcal activity assay, which will be further explained in chapter 5.

Chapter 5

Experimental Techniques

The purpose of this chapter is to explain the experimental methods employed in the research presented in this thesis. There are two main types of experiments that were performed to obtain the relevant data.

The first experimental technique that will be discussed is Raman spectroscopy. This will include an overview of the experimental setup and schematic overlay of the spectrometer. This section will demonstrate the basics of how this system operates by explaining the optical pathway. The particular system configurations and their affects on the data will also be explained. The procedure done to create samples that can be scanned by the spectrometer will also be discussed. The Raman spectroscopy methods will conclude with an explanation of the data analysis conducted on each lysozyme spectra. There is also a description of the lysozyme Raman spectrum and its features, as determined by the literature.

The final section of this chapter will explain the micrococcal assay, which was used to determine lysozyme activity. This will include a brief discussion about the general concept behind the experiment, as well as the different methodologies and sampling procedures used.

5.1 Raman Spectrometer

5.1.1 Optical Path in the Raman Spectrometer

The recorded Raman spectra were obtained using a Horiba Jobin Yvon HR800 series Raman spectrometer (Mississauga, ON, Canada) with Labspec 5 software. This system is coupled with an Olympus inverted microscope with a 20× long working objective with a 0.35 numerical aperture. The excitation source is an external Yag doubled, diode pumped 532 nm laser purchased from Coherent®.

Figure 5.1 shows a schematic overview of the Raman spectrometer. The external laser beam is directed by the M1 and M2 mirrors to enter the system at E1 and pass through a 6-filter wheel at F3. This filter is controlled by the software, and is designed to absorb different fractions of the laser intensity. There are 6 neutral filters with optical densities of 0.3, 0.6, 1, 2, 3, and 4. The M7 mirror then reflects the beam, after being focused by lens L1, onto the notch filter F4 at a particular angle which allows for a complete reflection towards the sample. The L2 lens creates a parallel beam focused on the sample.

The collected Raman and Rayleigh light is backscattered light produced by the interaction of the beam with the sample. This light follows back through the same configuration as the excitation radiation took to interact with the sample. The scattered light enters the F4 notch filter again, in which the Rayleigh scattered light is filtered out, while the Raman scattered light is allowed to pass straight through. The L2 lens focuses the scattered beam through this notch filter and onto the confocal hole H2.

The M10 mirror finally directs the Raman scattered light to the spectrograph. Figure 5.2 shows a side view of the spectrograph used, with the Raman scattering light entering at the Ms1 mirror. The light is then reflected to the grating system and focused into a CCD array, in which the data collected can be transferred to the computer system [43].

A diffraction grating allows for the scattered light to be spatially separated into its different wavelengths. It performs this function by consisting of many parallel reflecting grooves, as shown in figure 5.3. These grooves are spaced a distance similar to the wavelength of analyzed light. The incident radiation that is reflected by two adjacent grooves will have a particular path length difference. There are three variables that this path length difference is dependent on, which are the groove spacing, incident radiation angle (α) and the reflected angle (β). All light of a certain wavelength will constructively interfere when the path length difference is an integer value of that particular wavelength. This results in each wavelength to constructively interfere at a specific reflection angle, β, while others destructively interfere, and thus the light is spatial separated by wavelength [62].

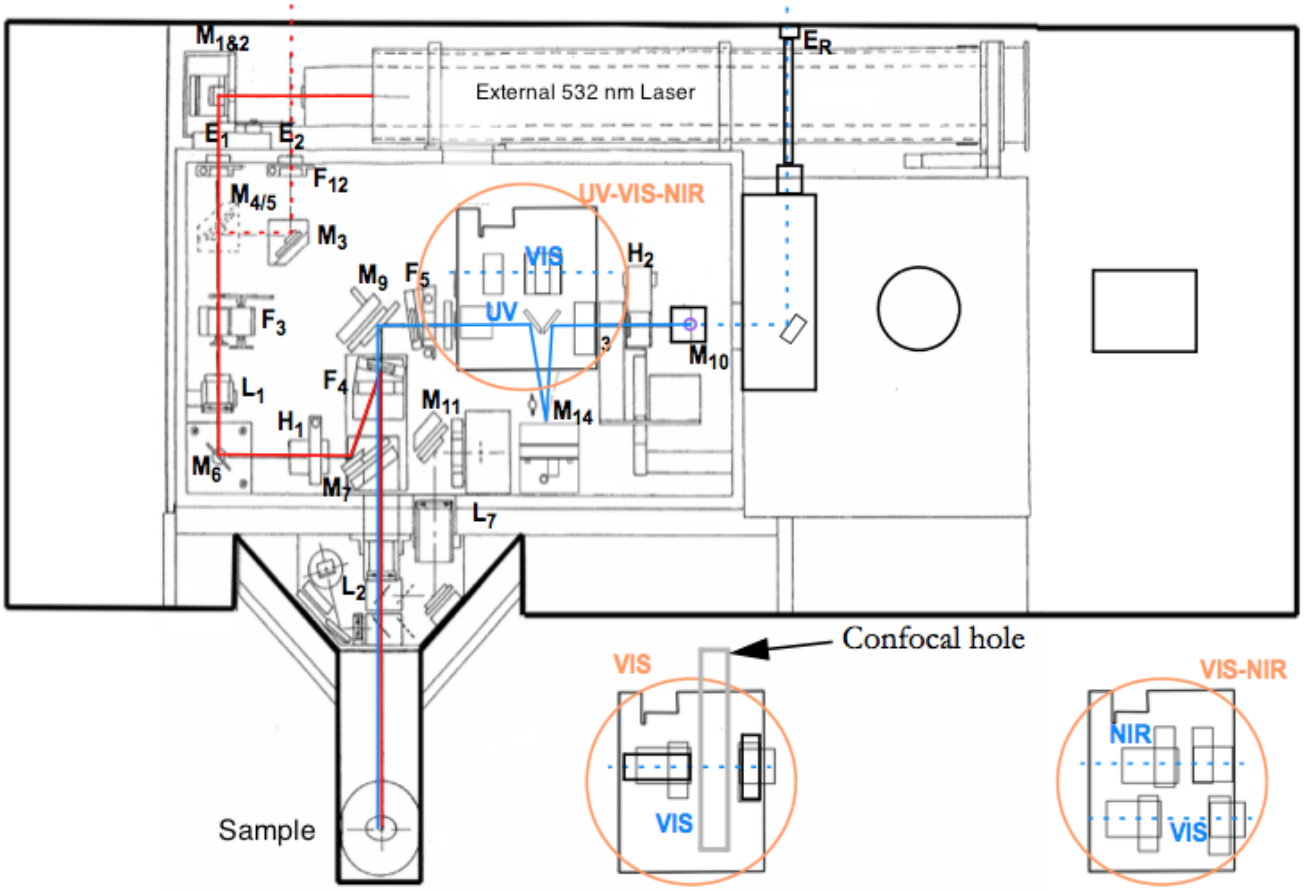

Figure 5.1: Schematic overview of the Horiba Jobin Yvon HR800 series Raman spectrometer [43].

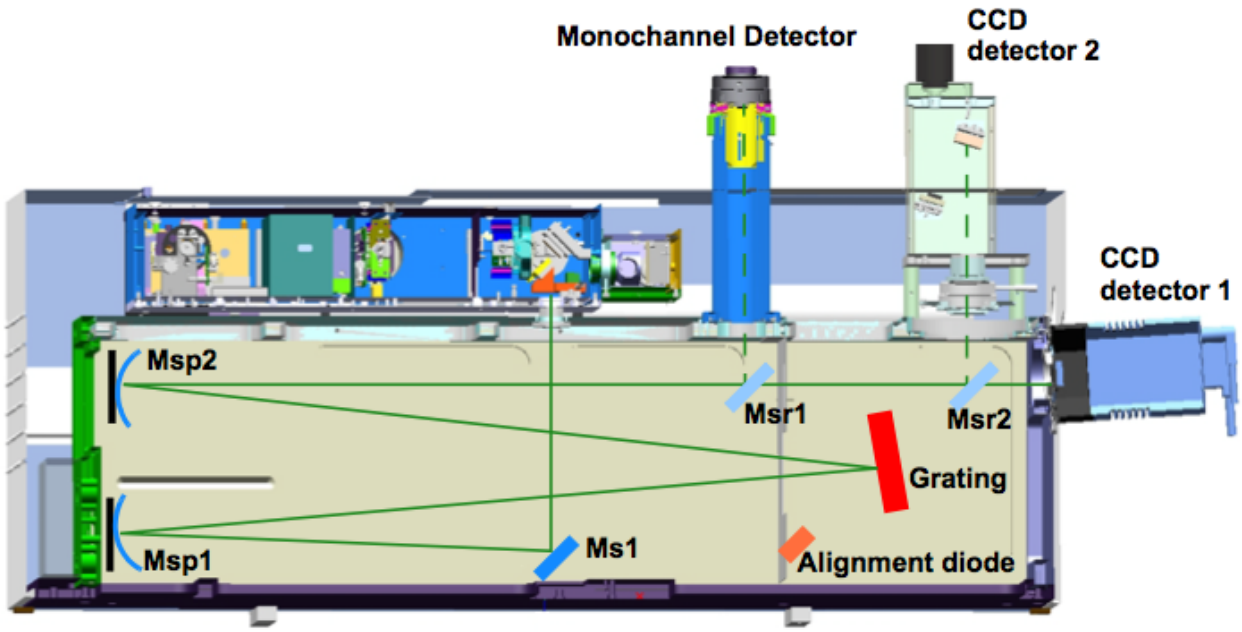

Figure 5.2: The light enters the spectrograph reflecting off the Ms1 mirror to a grating system and into a CCD for data collection [43].

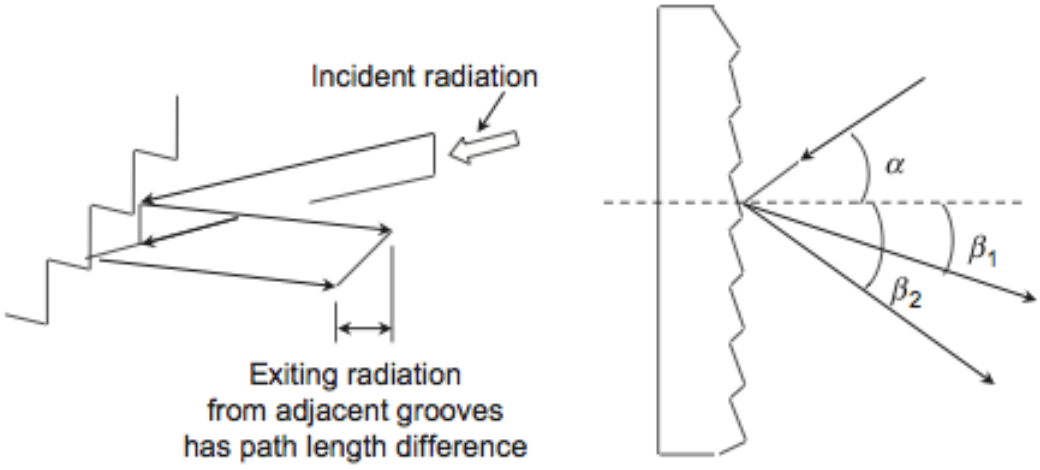

Figure 5.3: Light of different wavelengths are diffracted at varying spatial angles [62].

5.1.2 System Configurations

All scans recorded using the Raman spectrometer are first calibrated with respect to silicon. This is done by positioning the spectrograph to have the recorded Si ν_1 line at a theoretical value of 520.7 cm^{-1} [43]. This silicon peak is chosen simply because it produces a very strong Raman signal at this peak value and is a relatively common material.

The resolution of the Raman spectrometer is dependent on the grating spacing used. The system has a 800 mm focal length spectrograph equipped with two different grating types of 600 and 1800 gr/mm. A grating with a larger number of grooves per length has a higher resolution because the spacing between grooves are decreased, resulting in better dispersion of the light [35].

In addition to changing the resolution of each scan by switching grating types, there are several other parameters that may be altered to optimize the quality of the Raman spectra. As previously mentioned in section 5.1.1, there are six different filters that may be applied to reduce the intensity of the incoming laser source. The slit width can also be altered to allow different amounts of radiation to the sample.

The confocal hole size may also be configured. This mainly controls the depth of focus. As the confocal hole is closed, the depth is decreased, however, the Raman intensity will also be reduced. This leads to a compromise between signal and spatial resolution in the z-direction when choosing an appropriate hole size [43]. Smaller confocal sizes also result in a larger decrease in signal when the laser spot is moved slightly out of focus.

All scans performed for this thesis were done using the 1800 gr/mm grating with a slit width of 100 μm to produce a spectra resolution of about 0.4 cm^{-1}. The confocal hole is also kept at 100 μm. The repeatability of each scan should be $< 1cm^{-1}$ under normal temperature stability conditions ($\pm 1°C$) [43]. The main parameters that are altered between scans are the exposure time, the number of acquisitions and the power of the excitation radiation. The exposure time is the time allowed for the light to be collected for a single acquisition. All acquisitions for a given spectral range are then summed to give a final intensity count for each spectrum.

5.1.3 Sampling Procedures

The Raman system employed for this thesis uses a 180° backscattering geometry (instead of the commonly used 90° scattering geometry). This allows for quick and simple laser beam focusing on the sample, as well as sample replacement [35]. However, this arrangement can cause problems such as requiring the excitation source to first travel through a sample

container, such as a glass slide or vial. This can result in the appearance of background signal from the container material.

The vials used in this thesis for aqueous samples are KIMAX® (Mississauga, ON, Canada) sample vials made from borosilicate glass (8 mL vial with a height of 63 mm). Fortunately, this issue is mostly resolved as the glass vials give weak background Raman signals. This background signal can be even further minimized by using a small enough confocal hole. The laser must also be properly focused on the aqueous solution, which involves moving the focal spot to slightly above the glass-sample interface. The best results were obtained when the length of the focal column created in the solution extended the height of the solution. This require approximately 0.3-0.4 ml of solution in the KIMAX vials used.

The results presented in chapter 6 show Raman spectra of lysozyme in different contact lens solutions. The solutions examined were two multipurpose disinfection solutions called Bausch & Lomb ReNu multipurpose solution and Bausch & Lomb BioTrue multipurpose solution (Bausch & Lomb, Rochester, NY, USA), in addition to two hydrogen peroxide-based solutions – Alcon ClearCare (Alcon, Fort Worth, TX, USA) and Advanced Medical Optics UltraCare (AMO, Santa Ana, CA, USA). The ClearCare system is neutralized using a platinum coated disc, while UltraCare is neutralized using a catalase tablet.

The sample preparation involved using powered lysozyme from chicken egg white that was purchased from Sigma-Aldrich® (Oakville, ON, Canada) to make different concentrations of lysozyme. As discussed in section 3.4.3, chicken egg white can be used to reliably mimic the behaviour of human lysozyme. The lysozyme was first dissolved in phosphate buffered saline (PBS) solution before being introduced to a particular contact lens solution. The final concentration of lysozyme in the contact lens solutions used were approximately 50 mg/ml. This relatively high concentration compared to normal levels of lysozyme in tear film (approximately 0.5 - 2 mg/ml [91]) is used because lower concentrations produced extremely weak Raman signals and thus ambiguous spectra.

The problem previously described when using a backscattering technique are no longer relevant for solid samples. Chapters 7, 8 and 9 involve thin polymer films on a silicon substrate, graphene on nano pillars of silver, and etched gallium, respectively. These three types of samples are all solid surfaces, and thus can simply be inverted on the microscope stage in order to directly focus the laser beam on the substance of interest. This, of course, eliminates any issues related to a background signal due to the laser light having to travel through a container material.

5.1.4 Data Analysis

The Raman data from the lysozyme samples are collected using the above mentioned techniques. The data is converted and imported to the OriginPro 8 (Northampton, MA, USA) software program. This program has several useful automated functions which are utilized in the analysis of the recorded Raman spectra.

The initial analysis involves eliminating the background noise from the spectra caused by factors such as fluorescence and background signal from the container material. This is accomplished by using a baseline algorithm to manually fit multiple linear functions to a spectrum. These baseline functions can then be subtracted from the original data to obtain a spectrum with zero background signal.

The lysozyme spectral peaks can then be normalized with respect the 1448 cm^{-1} methylene deformation peak intensity, as practiced by Chen et al. (1973) [18]. This is done to allow comparisons between spectra, as the original data produces the vacuous and arbitrary unit of Raman intensity count as a function of Raman shift wavenumber. The information characterizing the spectral features, such as the peak positions, are obtained by fitting multiple Gaussian or Lorentzian functions to the normalized data set. Another fitting algorithm allowing multiple fitting functions incorporated in the software is utilized for this task.

5.1.5 Interpretation of Lysozyme Spectra

Both IR and Raman spectroscopy can be used to investigate the structural configurations of lysozyme. However, as previously mentioned in section 2.6.1, Raman spectroscopy provides an advantage of producing only very weak signals from the solvents involved, particularly water. The only moderately intense band produced by water appears in the spectral region 3200-3600 cm^{-1}. The other peaks of water, near regions of importance with respect to lysozyme, are 1640, 800, 450, and 175 cm^{-1}, which all exhibit extremely weak signals [66].

The Raman spectral peaks of lysozyme are displayed in table 5.1.5. The peaks are either due to vibrations in specific amino acid side group, or by certain types of vibrations between atoms within the backbone of the polypeptide chain. The presence of the aromatic side groups of phenylalanine (Phe), tryptophan (Trp) and tyrosine (Tyr) produce sharp spectral peaks.

One feature of the spectrum of lysozyme that can be of particular interest are the vibrations of the peptide bond in the backbone chain. The peptide (–CO–NH–) group, as

Table 5.1: This table shows the spectral peak values for lysozyme in a native state [18]. Relative intensities are normalized to the 1448 cm^{-1} peak, which is taken as 10. The *sh* abbreviation denotes a shoulder. Stretching vibrations between atoms are denoted by ν, while bending vibrations are denoted by σ.

Raman Shift (cm^{-1})	Relative Intensity	Tentative Assignment	Raman Shift (cm^{-1})	Relative Intensity	Tentative Assignment
315	3		1005	5 (sh)	Phe
333	0 (sh)		1012	11	Trp
353	0		1030	1 (sh)	Phe
375	0		1076	3	ν (C-N)
408	0 (sh)		1107	3	ν (C-N)
429	1		1129	2	ν (C-N)
462	1		1154	1	
507	4	ν (S-S)	1176	1(sh)	Tyr
525	1(sh)		1200	0 (sh)	Tyr and Phe
543	0	Trp	1208	1	Tyr and Phe
562	1		1234	2 (s)	Amide III
574	1	Trp	1254	5	Amide III
598	0		1271	1 (sh)	Amide III
622	1	Phe	1300	0	
645	1	Tyr	1327	0 (sh)	
660	1	ν (C-S) Cys	1338	11	Trp and σ (C-H)
700	1	ν (C-S) Met	1362	2	Trp and σ (C-H)
720	1		1427	1 (sh)	σ (N-H) indole rings
760	9	Trp	1448	10	σ (C-H)
834	1 (sh)	Tyr	1459	5 (sh)	σ (C-H)
854	2	Tyr	1490	0	
878	6	Trp	1553	8	Trp
900	5	ν (C-C)	1582	3	Trp
933	3	ν (C-C)	1607	4 (sh)	
960	3		1622	5	Trp, Tyr, and Phe
978	4		1660	10	Amide I

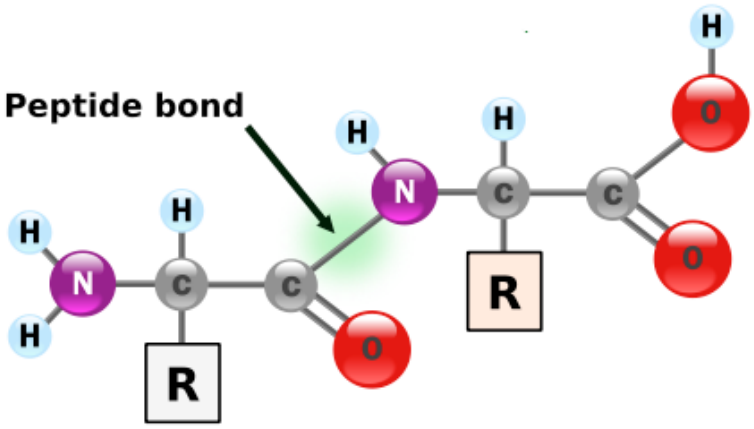

Figure 5.4: This is a diagram of a peptide bond, in which the CONH group produces the amide I and III regions of the Raman spectra of lysozyme [110].

depicted in figure 5.4, produces a total of nine different frequency groups, called the amide I, II, III, IV, V, VI, VII and the amide A and B. There exist two unique frequencies that are Raman active of particular importance at 1660 cm^{-1}, called amide I, and 1260 cm^{-1}, called amide III (assigned by the theoretical normal coordinate analysis [72]). The amide III is actually a triplet group, split into separate peaks at approximately 1240, 1262, and 1274 cm^{-1} [66]. This peptide group is involved in the stabilization of secondary structures through hydrogen bonding and interactions between side groups. Thus, both the amide I and III regions can signify changes in the α helices, β sheet, and random coil configurations [17, 18, 66]. However, amide III region is generally more sensitive to the structure than amide I [35].

On the basis of theoretical results [72], the amide I frequency has been assigned to the stretching mode of the C=O double bond. The amide III frequencies are allotted the coupled vibrations between the C–N stretching mode and N–H in-plane bending. The other coupled vibration is deemed the amide II region near 1567 cm^{-1}, however it produces an extremely weak Raman signal (although it exhibits a strong IR absorption). The amide IV, V, VI, VII groups also produce very weak Raman signals and are thus not readily used to study the structural conformation of the protein. The amide A and B frequencies (occurring at 3280 and 3090 cm^{-1}, respectively) arise from the Fermi resonance between the first overtone of the amide II vibration and the N–H stretching vibration. These peaks are usually masked in Raman spectra due by water modes and aromatic C–H stretching lines [66].

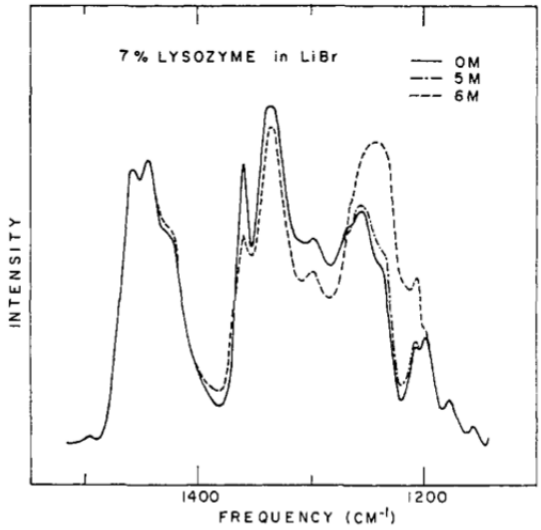

Figure 5.5: This figure displays the literature results of the amide III region of the Raman spectra of both native and chemically denatured lysozyme. The graph shows the different concentrations of LiBr used to denature the lysozyme [18].

Denaturation, as described in section 3.2, can be a complex process. There are many different unique protein configurations that can result in a loss of functionality, and thus be classified as the protein having become denatured. In fact, the process of a protein undergoing thermal denaturation and chemical denaturation can produce different denatured conformational states [87]. This thesis involves the possible chemical denaturation of lysozyme. However, the variety of different chemicals may again result in a distinct structural state and thus unique alterations in the Raman spectra.

Fortunately, as previously mentioned, the amide I and III regions give information about the secondary structure of the protein, and thus have the potential to distinguish between a native and a general denatured state. There are many different types of denaturation that have common alterations in these spectral regions (from both thermal and chemical denaturing [12, 17, 18]). They can then be reliably used as an indication of denaturation.

There have been multiple studies performed that show the Raman spectral changes that appear from denaturing lysozyme with several different chemicals. One common chemical explored is the denaturing effect of LiBr, performed by Chen et al. (1974) [18] and Porubcan et al. (1979) [87]. Figure 5.5 shows the amide III region of te Raman spectra comparing native lysozyme peaks to denatured lysozyme. There are several common changes to this amide III region that can be used to determine a state of denaturation. One main alteration

is that the amide III 1260 cm^{-1} peak, which is associated with the strongly hydrogen-bonded α helix structure, decreases to 1243 cm^{-1}, which is assigned to weaker hydrogen-bonded groups. This shifted peak also intensifies considerably. The interpretation of this change is that the backbone structure of the protein has shifted to a random coil formation [18, 87], which is occurs in thermal denaturing studies [17].

Another apparent change includes the decreasing of intensity in the 1338 and 1363 cm^{-1} peaks. These peaks both represent tryptophan vibrations, indicating a change in the environment of these side groups. This may possibly be due to hydrogen bonding between the bromide ion and indole NH [18]. Other changes include the increasing of the phenylalanine peaks at 1005 and 1030 cm^{-1}. The peaks at 1199 and 1209 cm^{-1} both correspond to tyrosine and phenylalanine and undergo a decrease in peak intensity.

The broadening and decreasing of the 900, 933 and 1105 cm^{-1} peaks are another indication of a random coil conformation. They are likely caused from the C–C and C–N stretching vibrations of the chain backbone [17]. These are also similar changes that occur in thermal denaturing [17]. This broadening and weakening is predicted to be a result of the variable conformations of side chains normally buried in the hydrophobic core of the protein. The rigid nature of the native lysozyme allow for only a single configuration of these inner side groups, however, upon denaturation, these groups can go through different formations and a variety of vibrations may occur.

The amide I region also have associated alterations. Mainly, the 1660 cm^{-1} peak is expected to increase and sharpen to 1672 cm^{-1}. However, this may be masked by the solvent of the protein, such as the LiBr observed by Chen et al. (1974), but may be visible with other chemical solutions [18].

The last major modification to the Raman spectrum of lysozyme that may occur as it denatures is the broadening and decreasing of the 509 cm^{-1} peak. This spectral peak corresponds to the disulfide bridges of the protein. The weakening of this signal thus indicates the breaking of these bridges, or at least a shift into different bond configurations, that may distort the structural form of the molecule [17, 18]. This peak change is also evident in thermal denaturation [12, 17].

Many of the differences in the Raman spectra between the denatured and native states of lysozyme occur for other chemicals such as sodium dodecyl sulfate (SDS) and S-cyanoethylation. However, not all chemicals produce the exact same denaturing spectral changes. Figure 5.6 shows the full Raman spectrum of the denatured state of S-cyanoethyl lysozyme, in which the sulfhydryl groups are specifically blocked and the S–S bonds are reduced.

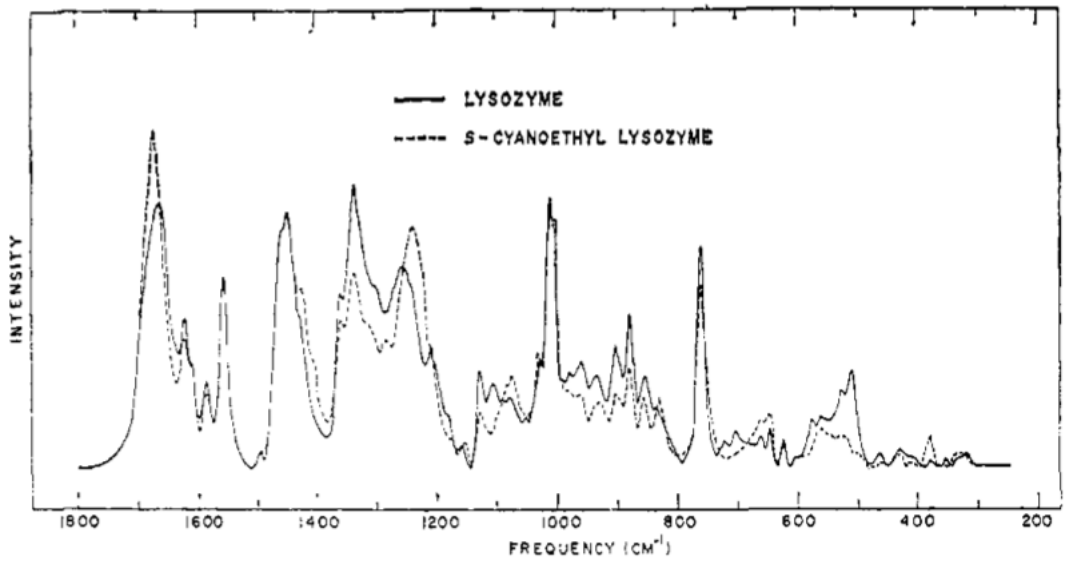

Figure 5.6: This figure displays the Raman spectrum of both native and chemically denatured lysozyme by S-cyanoethylation [18].

5.2 Micrococcus Assay

While the Raman spectra of lysozyme can determine structural configurations of the protein, a micrococcal assay can measure its functional activity. This provides two different means of studying denatured lysozyme since, as discussed in section 3.2, both the structure and function of proteins are related to denaturation. The main purpose of these activity assays is to measure the total concentration of denatured lysozyme that is present in a solution.

5.2.1 General Concept

The general process in which the micrococcus assay can determine the activity of lysozyme is relatively simple. As previously described in section 3.4.2, one of the main functions of lysozyme is to kill bacteria. However, lysozyme can only perform this action when it is in an active configuration, and cannot kill bacteria when denatured.

When lysozyme is added to a solution of bacteria, the active lysozyme will begin to kill the bacteria. The greater the amount of active lysozyme, the faster the bacteria will

die. In order to measure this death rate of bacteria cells, a spectrophotometer is utilized. This spectrophotometer shines light of a known specific wavelength and intensity through the sample of lysozyme and bacteria. The intensity of light that escapes the sample can be compared to the initial intensity to determine the optical density of the sample [93]. Optical density is the logarithmic ratio of the transmitted radiation intensity to the incident intensity.

The living bacteria cells will have a certain optical density, however, when the bacteria are destroyed their cell walls are fragmented, and thus the optical density of the solution will go down, due to a decrease in light scattering. The spectrophotometer allows for this rate of decreasing optical density to be recorded. For a given sample, the rate of loss in optical density can be compared to a control sample with a known amount of active lysozyme. This rate of change of optical density will be linearly related to the amount of active lysozyme present. The amount of native lysozyme in a sample is determined from a standard linear regression using these control samples.

5.2.2 Experimental Procedure

Each assay is performed using a new solution of the bacteria, called *micrococcus lysodeikticus*, which is readily destroyed by the native state of the lysozyme protein. Each stock of bacteria is made on the previous day from a ratio of 2 ml PBS to 1 mg of dried *micrococcus lysodeikticus* (stored at -20°C), which was purchased from Sigma-Aldrich®. This ratio is slightly altered, such that an initial optical density of approximately 1.1-1.2 is achieved at 450 nm using a SpectraMax M5 (Downingtown, PA, USA). The bacteria solution is left at 4°C in a refrigerator overnight. Each bacteria stock is put into an oven kept at 31°C approximately 30 minutes before use.

Each sample is made from an initial stock of lysozyme dissolved in PBS. The lysozyme solution is then added to the particular contact lens solution of interest to a concentration of approximately 40 ng/μl. This concentration was made mostly to be large enough to represent a similar concentration of lysozyme in actual tear film. However, if the concentration was too great the bacteria would be destroyed too quickly to produce reliable data. A standard lysozyme solution in PBS is also made to be included as a control for each scan. The standards are made with an initial concentration of 80 ng/μl, which is serial diluted to produce standard samples at 80 ng/μl, 60 ng/μl, 40 ng/μl, 30 ng/μl, 20 ng/μl, 10 ng/μl. Each standard is repeated twice per measurement and averaged in order to obtain a more accurate standard graph. All solutions are made in glass vials to minimize any binding interaction of the lysozyme with the container [73].

Using a micro-pipette, 10 μl of each sample, as well as the standard solution, is put into a separate wells in a 96 clear bottom well plate, purchased from Cellstar®. Thus, each sample well will have a total theoretical value of approximately 400 ng of lysozyme present, while the standard wells will have 800, 600, 400, 300, 200, and 100 ng of lysozyme. Each particular sample is repeated in three different wells to obtain the standard error of the measured lysozyme amounts.

A multichannel pipette is then used to insert 290 μl into each sample well. The optical density of the wells are then measured at 15 second intervals with the spectrophotometer, for up to 15 minutes, at 450 nm and set to a temperature of 30°C. The data is collected using a program called SoftMax Pro 5. Each well plate is also included with a sample of the different contact lens solutions without lysozyme. This allows for their relative contributions to destroying the bacteria cells to be determined.

5.2.3 Data Analysis

The optical densities at the respective time intervals for each of the standard and sample well plates are export and plotted. The standards are first plotted and a linear function is extrapolated to obtained a rate of change of optical density as a function of time. This rate of change in optical density for each of the standard values is then plotted against the theoretical masses of lysozyme present, which is assumed to all be in a native state. A linear regression fit is again applied to the relationship between the mass of active (control amount) lysozyme present and the rate of change of optical density. This provides a standard plot that may be used to determine the amount of native lysozyme present in the samples of interest.

The sample plots are processed in the same means as the standard graphs. The sample sets which have only the contact lens solutions, and no lysozyme, are also plotted. The rate of decreasing optical density resulting from the contact lens solution itself destroying bacteria is thus obtained as well. The rates of changing optical densities for all samples are then compared to the standard plot to ascertain the amount of active lysozyme present in the sample. However, this measured amount of lysozyme in each sample accounts for both the lysozyme destroying the bacteria, as well as the disinfecting contact lens solution. To obtain the actual amount of active lysozyme, the apparent lysozyme amount that is observed for samples with exclusively contact lens solutions only (no lysozyme) must be then subtracted from the recorded lysozyme mass present in the samples of interest. This produces a more accurate account of active lysozyme present in the samples. This normalized mass is compared to the total initial mass (400 ng) per well to determine an

active percent of lysozyme such that

$$\% \text{ of Active Lysozyme} = \text{Active Lysozyme Mass/Total Mass of Lysozyme} \times 100\%$$

Part II

Lysozyme Denaturation Results and Discussion

Chapter 6

Lysozyme in Contact Lens Solutions

This chapter will provide the results and discussion sections regarding research on lysozyme denaturation in various contact lens solutions. The first section of this chapter will be dedicated to presenting the Raman spectra that were recorded of lysozyme when dissolved in several contact lens solutions. The spectral alterations will be compared to the known spectral indications of a denatured state, as determined by literature findings, as discussed in section 5.1.5.

The next section in this chapter will involve the results measured from micrococcal assays. This will include a brief discussion of the unsuccessful attempts made to collect data and the troubleshooting involved. The results that produced meaningful data will then be discussed, using the experimental procedure explained in sections 5.2.2 and 5.2.3. The Raman and assay results will then be discussed and compared. The final section will present the conclusions and possible future research that may be done to improve and complement the results of this chapter.

6.1 Raman Spectra of Lysozyme in Contact Lens Solutions

Four different brands of contact lens solution were tested in this research for their effect on the state of lysozyme. The two MPS systems that were used were Bausch & Lomb ReNu fresh® (Rochester, NY) and Bausch & Lomb Bio True® (Rochester, NY), while the two peroxide-based systems were Alcon ClearCare® (Fort Worth, TX) and AMO UltraCare® (Santa Ana, CA).

Figure 6.1 shows the Raman spectra of the ReNu solution, without the presence of lysozyme. Figure 6.2 shows the Raman spectra of BioTrue, also in the absence lysozyme. Both spectra are similar and seem to have a strong peak near 877 cm^{-1}. The other major feature that are present in both the MPS samples due to components of the solutions is a very broad signal near 1637 cm^{-1}.

In order to obtain enough signal to produce strong Raman peaks, as previously discussed in section 5.1.3, the concentration of lysozyme in each contact lens solution needed to be considerably larger than tear film levels of approximately 0.5-2 mg/ml [91]. The concentrations of lysozyme in all of the following contact lens solutions used were about 50 mg/ml. The effects of using this relatively high concentration of protein will be further discussed in section 6.3.

The figures 6.3 and 6.4 depict the measured Raman spectra of dissolved lysozyme in the MPS ReNu and BioTrue, respectively. The background signals were subtracted and the spectra are normalized to the 1448 cm^{-1} peak. Each solution was scanned approximately 24 hours after the introduction of the lysozyme and compared to the initial spectrum. It is evident that each spectrum undergoes minimal changes.

The Raman spectra of the two hydrogen peroxide solutions ClearCare and UltraCare are depicted in figures 6.5 and 6.6, respectively. These are the spectra of the solutions prior to neutralization. Each have strong peaks around 876 cm^{-1}, which can mainly be attributed to the hydrogen peroxide molecules present [104]. Both spectra, again, have an extremely broad signal near the 1637 cm^{-1} line, possibly due to the other components in the solution.

When lysozyme was added to the non-neutralized hydrogen peroxide solutions, a cloudy white precipitate was visible after a certain amount of time. This precipitate could be focused on directly when enough mass had accumulated at the bottom of the vial. The earliest time that a relatively strong Raman signal of the precipitate was recorded was approximately 11 hours for the ClearCare solution, and about 1 hour and 40 minutes for the UltraCare solution. Some Raman recordings showed some spectral indications of structural changes at earlier times, however the scans produced relatively weaker signals. Figures 6.7 and 6.8 show the initial and final scans of lysozyme in ClearCare and UltraCare, respectively, after the given amount of time. The strong hydrogen peroxide peak near about 876 cm^{-1} was subtracted out from the spectra.

The spectra of the precipitate that formed has several spectral alterations with respect to the initial, presumably native, state of lysozyme. Both the ClearCare and UltraCare solutions seemed to produce similar alterations to the initial spectrum of lysozyme, and have several features similar to the denatured lysozyme produced by the chemical LiBr

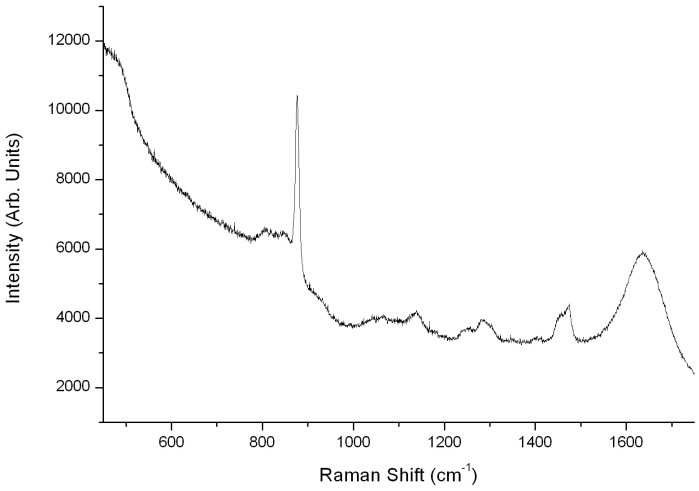

Figure 6.1: This figure is a Raman spectrum of ReNu solution without the presence of lysozyme. Background was not subtracted, and thus the intensity is in arbitrary units. A power of 100 mW was used at an exposure time of 60 seconds for 20 acquisitions.

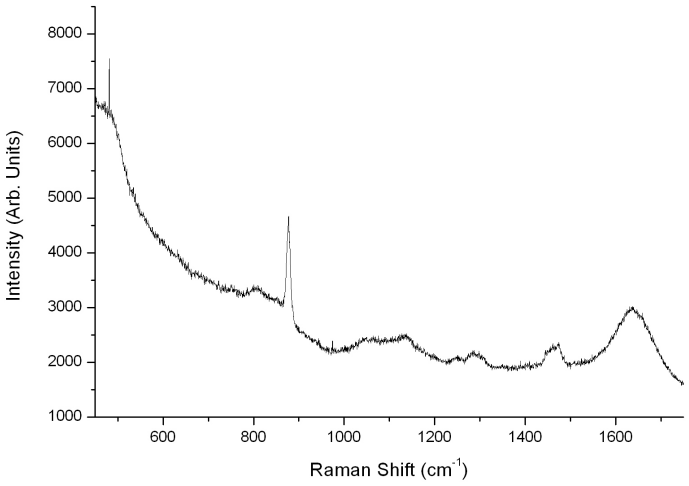

Figure 6.2: This figure is a Raman spectrum of BioTrue solution without the presence of lysozyme. Background was not subtracted, and thus the intensity is in arbitrary units. A power of 100 mW was used at an exposure time of 60 seconds for 20 acquisitions.

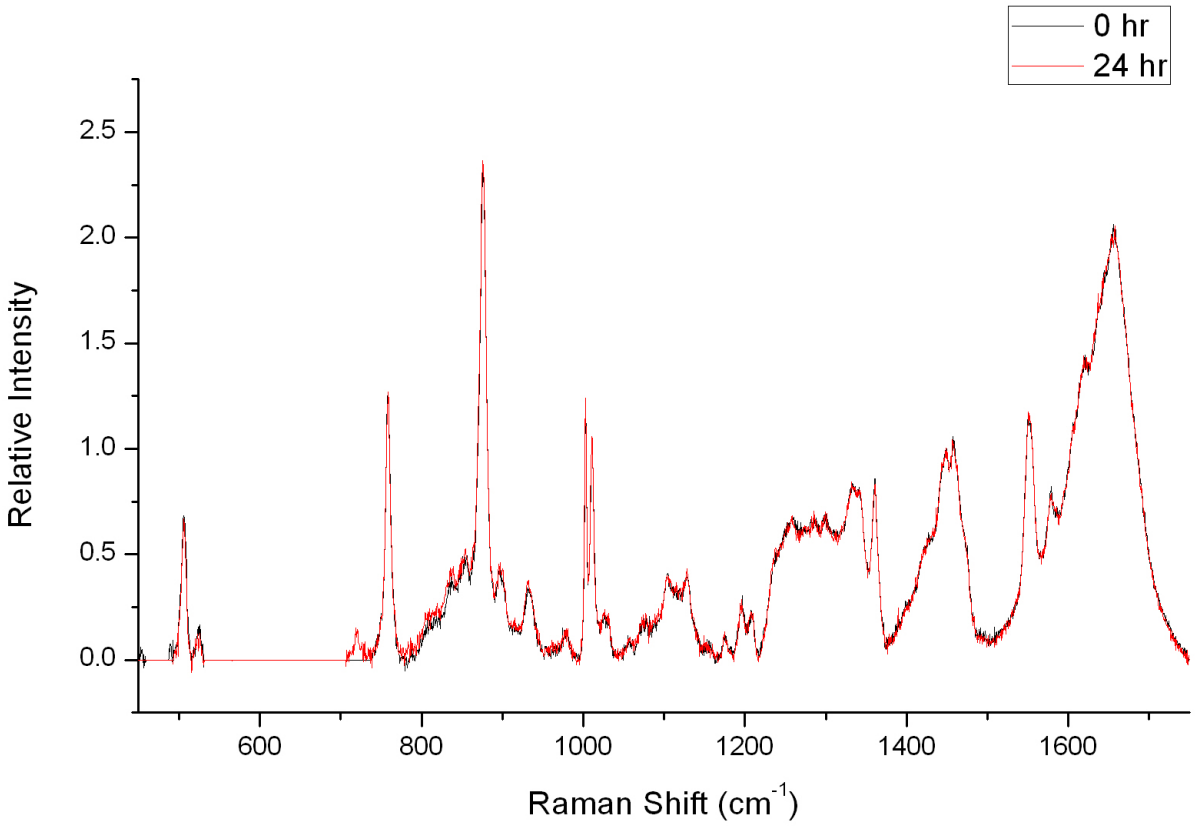

Figure 6.3: This figure is a Raman spectrum of ReNu solution at a lysozyme concentration of approximately 50 mg/ml. Background was subtracted and intensities are normalized to the 1448 cm^{-1} peak. The spectrum is unchanged after about 24 hours. A power of 100 mW was used at an exposure time of 60 seconds for 20 acquisitions.

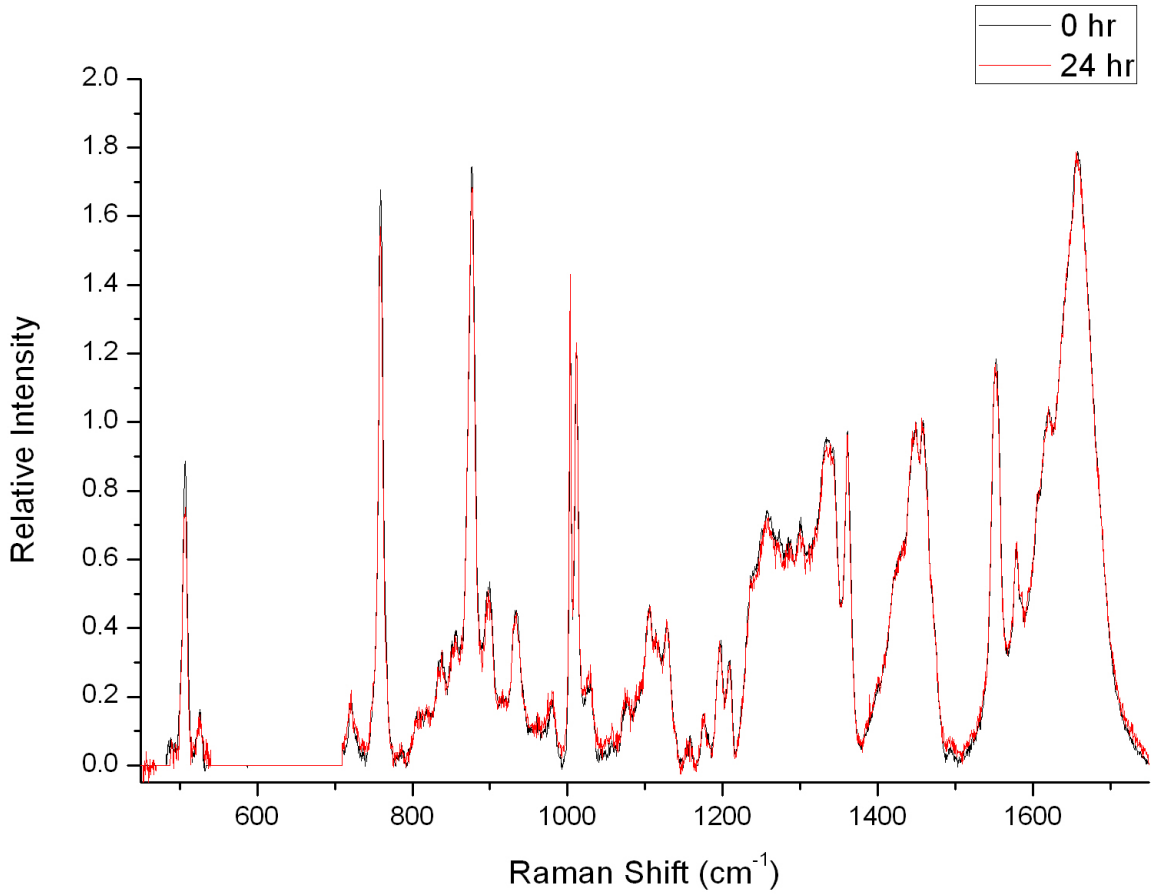

Figure 6.4: This figure is a Raman spectrum of BioTrue solution at a lysozyme concentration of approximately 50 mg/ml. Background was subtracted and intensities are normalized to the 1448 cm^{-1} peak. The spectrum is unchanged after about 24 hours. A power of 100 mW was used at an exposure time of 60 seconds for 10 acquisitions.

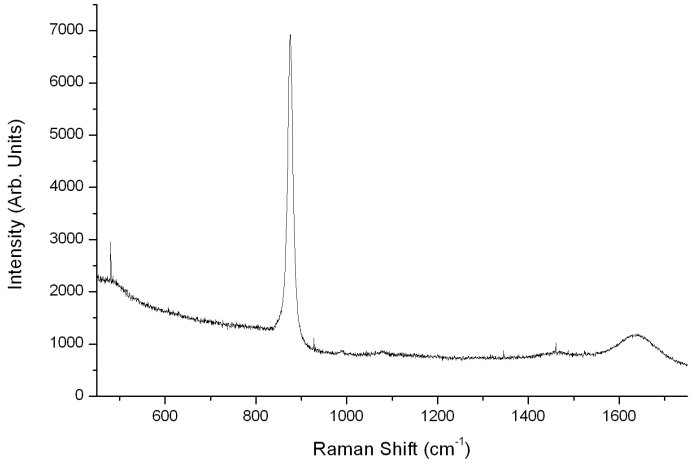

Figure 6.5: This figure is a Raman spectrum of ClearCare solution without the presence of lysozyme. Background was not subtracted, and thus the intensity is in arbitrary units. A power of 100 mW was used at an exposure time of 60 seconds for 20 acquisitions.

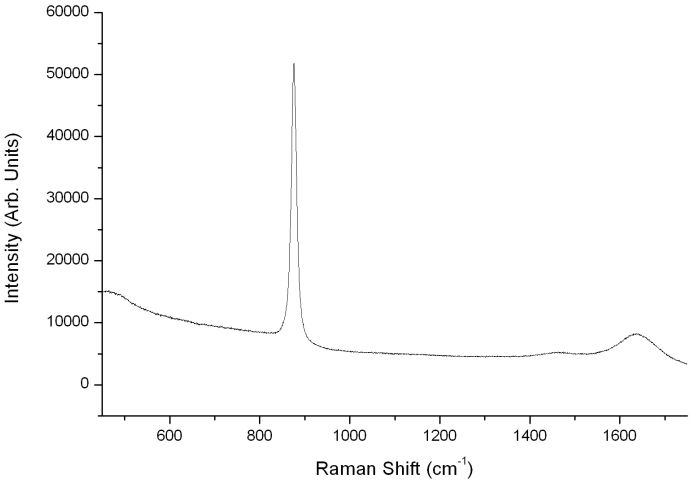

Figure 6.6: This figure is a Raman spectrum of UltraCare solution without the presence of lysozyme. Background was not subtracted, and thus the intensity is in arbitrary units. A power of 100 mW was used at an exposure time of 60 seconds for 20 acquisitions.

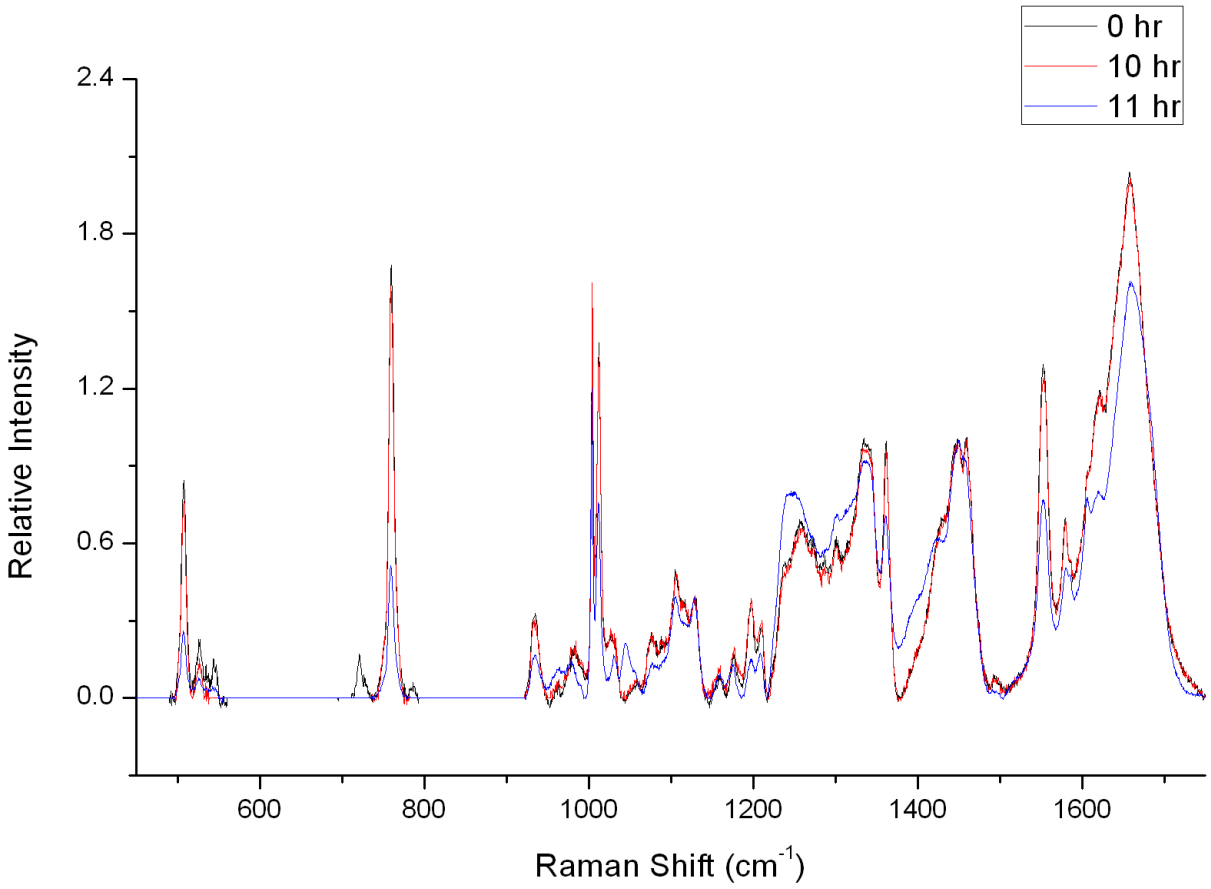

Figure 6.7: This figure is a Raman spectrum of ClearCare solution at a lysozyme concentration of approximately 50 mg/ml. A relatively strong spectrum with visible spectral alterations was obtained at approximately 11 hours of lysozyme exposure. Background was subtracted and intensities are normalized to the 1448 cm^{-1} peak. A power of 100 mW was used at an exposure time of 60 seconds for 20 acquisitions.

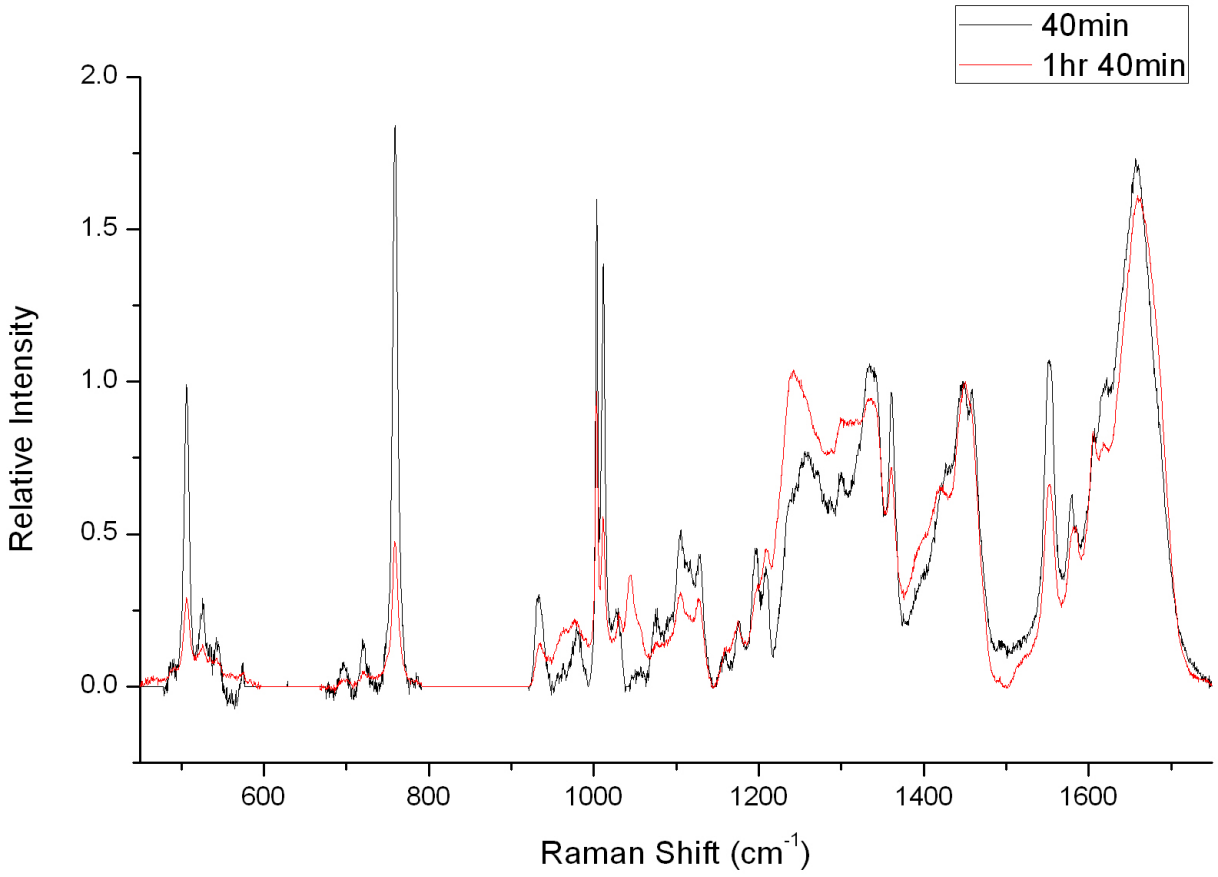

Figure 6.8: This figure is a Raman spectrum of UltraCare solution at a lysozyme concentration of approximately 50 mg/ml. A relatively strong spectrum with visible spectral alterations was obtained after approximately 1 hour and 40 minutes of lysozyme exposure. Background was subtracted and intensities are normalized to the 1448 cm^{-1} peak. A power of 100 mW was used at an exposure time of 60 seconds for 20 acquisitions.

shown by Chen et. al [18], as discussed in section 5.1.5.

One of the most prominent changes in the lysozyme spectrum is in the amide III region, in which the α helix peak at 1260 cm^{-1} is shifted to 1240 cm^{-1} and intensified. This effect is one of the most prominent indications that the structure of the molecules have changed to a random coil conformation, and thus become denatured. It is also evident that the tryptophan peaks at 1553 and 1362 cm^{-1} decrease.

The amide I region at 1660 cm^{-1}, however, does not seem to substantially alter in any respect, despite predicted changes for a denatured state (1660 cm^{-1} peak shift to 1673 cm^{-1}) [18, 72]. This may be due to a masking effect from the solvent. Since the contact lens solutions can be seen to have a broad signal near 1637 cm^{-1}, as seen in figure 6.5 and 6.6, the background solvents may prevent any noticeable changes in this region of the spectrum.

There are multiple other spectral modifications that are related to a denatured state similar to chemicals such as LiBr. Both the 933 and 1105 cm^{-1} peaks, representing the C–C and C–N chain backbone stretching modes, showed a broadening and decrease in intensity. These changes are another strong indication of a random coil formation in the structure [18]. A decrease in the 900 cm^{-1} peak, however, is not evident. This again may be attributed to a masking effect caused by the presence of hydrogen peroxide in the solution producing a very strong Raman signal at the 876 cm^{-1} line. The 1199 cm^{-1} and 1209 cm^{-1} peaks corresponding to both tyrosine and phenylalanine were found to decrease in intensity with LiBr [18].

Both the ClearCare and UltraCare produce a lysozyme spectrum with a decreased 1199 cm^{-1} peak intensity, however, the 1209 cm^{-1} peak did not seem to be affected. Another deviation from the study involving LiBr was the apparent decrease, rather than increase, in the spectral intensities at 1005 and 1030 cm^{-1}. These peaks both represent phenylalanine groups, and thus may indicate a change in the environment for these side groups. There is also, interestingly, a large increase in the intensity at a peak position of 1045 cm^{-1}, which represents an unknown structural effect.

The last major indication of denaturation in the lysozyme is evident in the decrease in the disulfide bridge peak at 509 cm^{-1}. This may relate to the breaking or reconfiguration of at least some of the four disulfide bonds. This effect is apparent in many forms of denaturation by different chemicals as well as thermal denaturing [18, 17].

The cause for this apparent denaturation at these high lysozyme concentrations in the hydrogen peroxide-based systems was then further investigated. One possible cause for the denatured protein is the hydrogen peroxide in each of the solutions. The ClearCare and UltraCare solutions both have a concentration of 3% hydrogen peroxide by mass.

Hydrogen peroxide was added to milli-q water to achieve an aqueous solution of different H_2O_2 concentrations. A solution of 0.1%, 1%, 3%, 8%, 10% and 20% hydrogen peroxide was made with a 50 mg/ml lysozyme concentration and scanned after a 24 hour period. The only solutions that showed signs of denatured lysozyme present after this time was the 10% and 20% H_2O_2 solutions. Figure 6.9 shows the Raman spectrum of the lysozyme in a 10% H_2O_2 solution. Similar indications of denaturation is present in the spectrum as previously recorded, namely the amide III alterations indicating a random coil configuration and a decrease in the 509 cm^{-1} disulfide bridge peaks.

Another possible factor contributing to the resulting denatured lysozyme in the hydrogen peroxide systems is the acidic pH of each solution. ClearCare and UltraCare have a pH of 6.53 and 3.33, respectively. To investigate the effect of the pH, solutions with a constant 3% H_2O_2 concentration were made while the pH was varied using hydrochloric acid. The different pH levels tested were 7.4, 4.85, 2.75, 2.45, and 2.21. The only solution that showed spectral indications of denatured lysozyme after 24 hours was at a pH of 2.21. The corresponding lysozyme spectrum had, again, similar spectral shifts that showed structural changes as previously discussed in this section.

The effect of lysozyme in these hydrogen peroxide systems at the same time in which the neutralization process occurs was also investigated. Figures 6.10 and 6.11 show the two hydrogen peroxide systems while being neutralized in the absence of lysozyme. The hydrogen peroxide peaks, particularly at 876 cm^{-1}, are no longer visible due to the neutralization process of chemically reacting with the hydrogen peroxide. However, it is evident that each solution still has a broad peak centered around 1637 cm^{-1}. It is also worthy to note the appearance of a strong peak at 1500 cm^{-1} in figure 6.11. This mode must be due to some component in the neutralizing tablet for UltraCare, as it does not appear in the spectrum of non-neutralized UltraCare without lysozyme, as seen in figure 6.6.

Figure 6.12 shows the Raman spectra of the lysozyme in ClearCare as it is being neutralized, and figure 6.13 shows the results for the UltraCare solution. Each solution showed a different effect on denaturing lysozyme than the previous spectra showing lysozyme in the contact lens solution without neutralization. The lysozyme in the neutralizing ClearCare did not result in any spectral indications of denaturation after a period of approximately 24 hours.

The neutralizing UltraCare, conversely, still showed signs of denaturing the lysozyme. However, the denatured lysozyme could be detected about 1 hours and 25 minutes after the initial exposure, in contrast to 1 hour and 40 minutes in non-neutralized UltraCare solution. The slight increase in the spectral intensity at 1500 cm^{-1} is due to the components of the neutralizing tablet, which are visible when no lysozyme in present, as seen in figure 6.11.

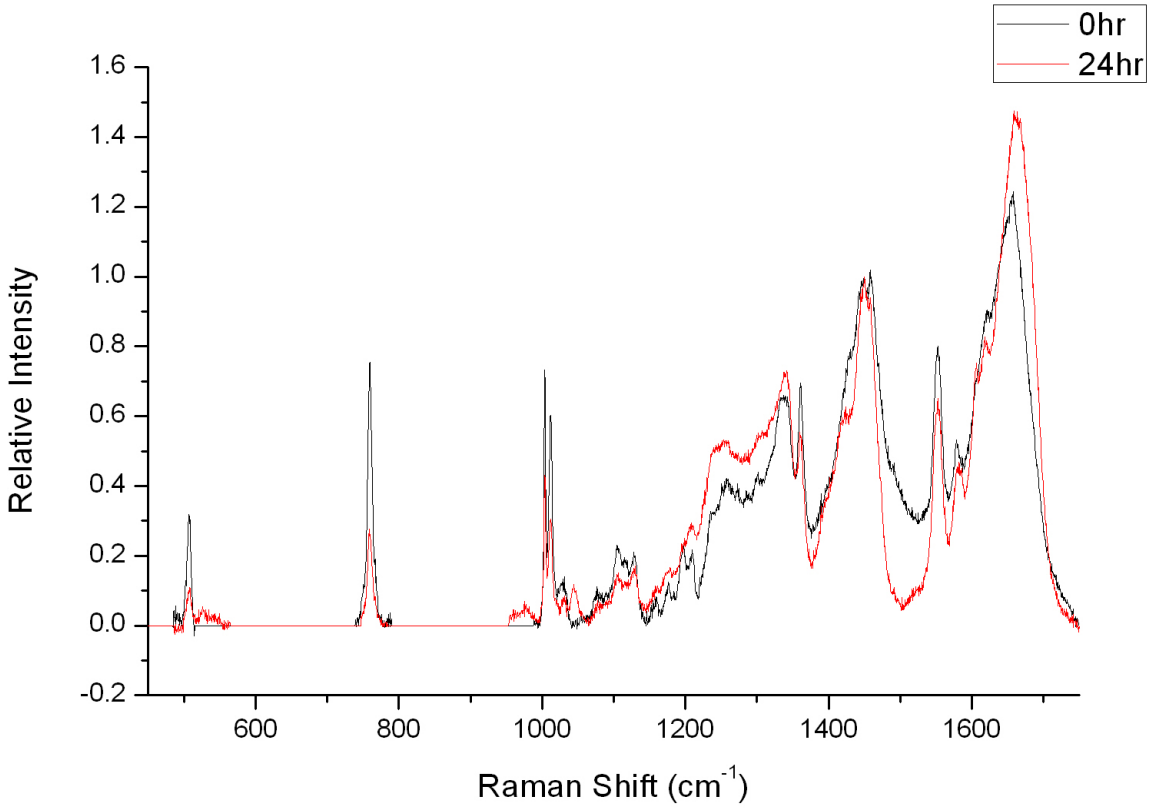

Figure 6.9: The Raman spectrum of a 50 mg/ml lysozyme concentration solution after 24 hours in a 10% hydrogen peroxide solution. Background was subtracted and intensities are normalized to the 1448 cm^{-1} peak. A power of 100 mW was used at an exposure time of 60 seconds for 20 acquisitions.

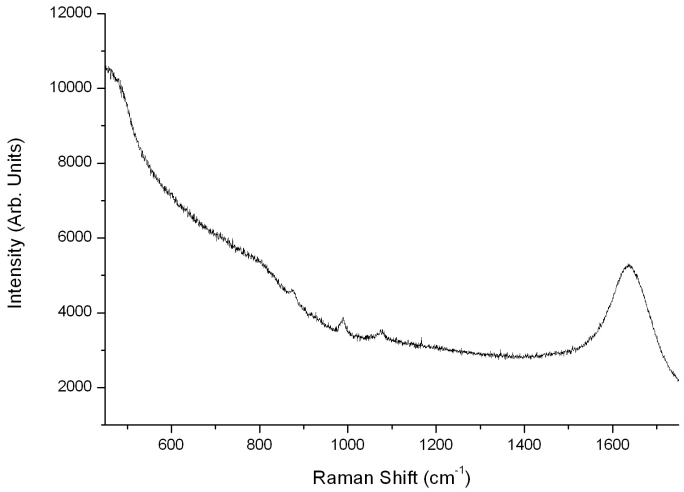

Figure 6.10: This figure is a Raman spectrum of neutralized ClearCare solution without the presence of lysozyme. Background was not subtracted, and thus the intensity is in arbitrary units. A power of 100 mW was used at an exposure time of 60 seconds for 20 acquisitions.

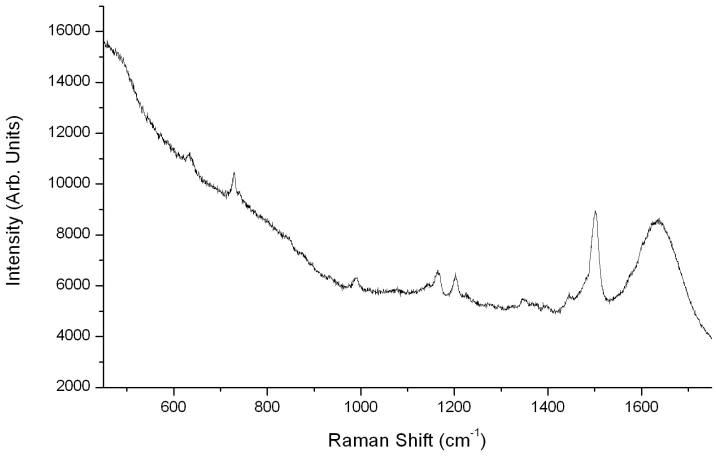

Figure 6.11: This figure is a Raman spectrum of neutralized UltraCare solution without the presence of lysozyme. Background was not subtracted, and thus the intensity is in arbitrary units. A power of 100 mW was used at an exposure time of 60 seconds for 20 acquisitions.

The large decrease in the hydrogen peroxide peak at 876 cm^{-1} is due to the neutralization of the solution, and thus break down of hydrogen peroxide molecules.

The causes for the apparent denaturing in the neutralized UltraCare solution was further investigated. The individual effects of the neutralizing tablet were examined by exposing a solution of lysozyme dissolved in PBS (rather than UltraCare) to this tablet. Figure 6.14 shows the resulting spectra from this experiment. The main spectral differences occurred after 1 hour and 16 minutes of exposure. The most significant alterations include a decrease in the 509 cm^{-1} representing a destruction of the disulfide bonds. The other major discrepancy that occurred is the spectral shift and intensification of the 1260 cm^{-1} to 1240 cm^{-1}, as well as a decrease in the 1362 cm^{-1} corresponding to alterations in the amide III and tryptophan modes, respectively. These primary changes all indicate a modification to the configuration of the lysozyme toward a random coil formation, similar to previous findings. Denaturation appears to also occur due to some component of the neutralizing tablet.

Several attempts were also made to reproduce these results for the various contact lens solutions at a much lower concentration of lysozyme (about 2 mg/ml) in order to more accurately mimic tear film. The difficulty presented was that the Raman signal of the lysozyme was too weak to clearly make out the spectral peaks within reasonable acquisition times. To overcome this issue, one strategy involved centrifuging the solutions to collect any precipitates that may form. The lower concentrations of lysozyme exposed to the contact lens solutions were centrifuged at 14,000 rpm for 1 hour to produce precipitates. These masses were then deposited on a glass cover slip. The samples were allowed to dry and the small clumps of precipitate were subsequently focused on to produce a stronger Raman signal than when left in solution. Scanning these precipitated masses showed similar indications of the lysozyme in a denatured state as the previous highly concentrated samples, such as the amide III spectral shifts.

6.2 Micrococcus Assay of Lysozyme in Contact Lens Solutions

6.2.1 Ineffective Experimental Methods

The final micrococcal assay results, as presented in section 6.2.2, uses the procedure described in section 5.2.2 and 5.2.3. However, before this procedure was established as a

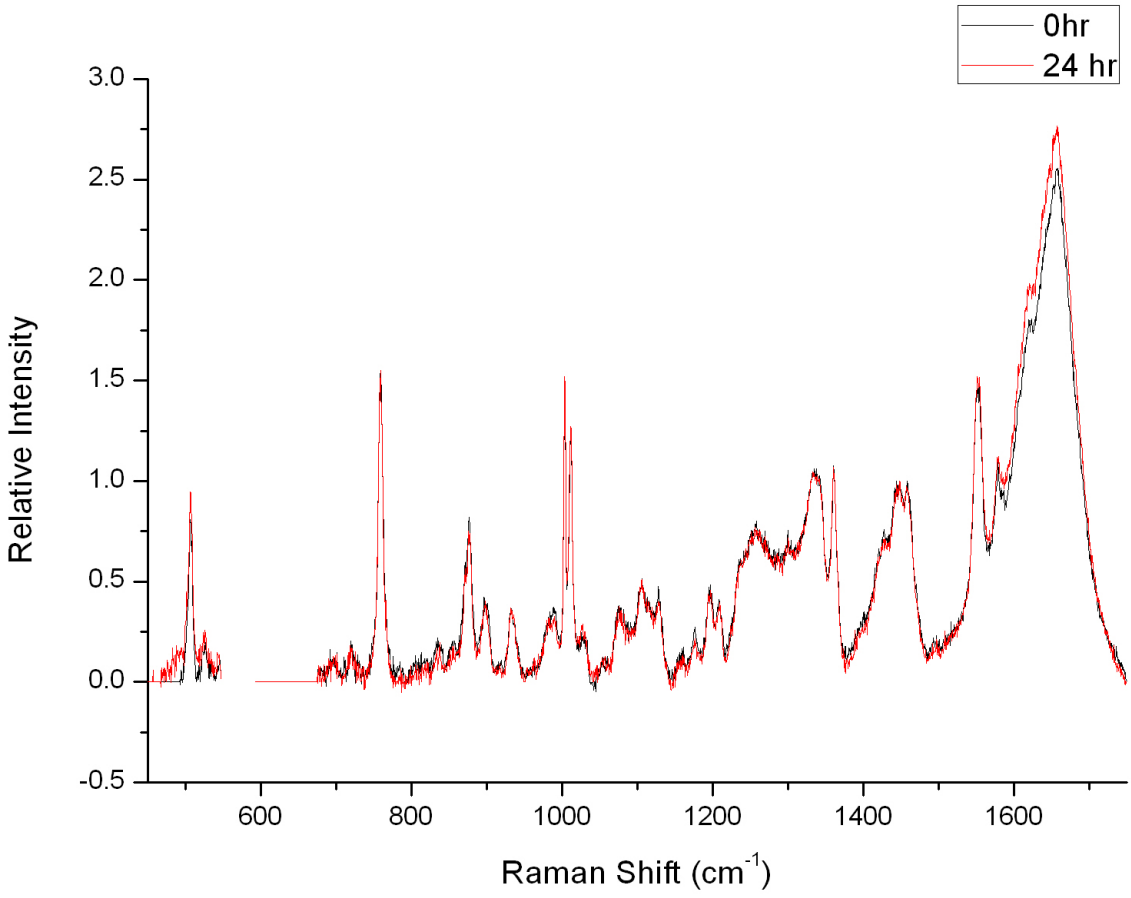

Figure 6.12: This figure is a Raman spectrum of neutralized ClearCare solution at a lysozyme concentration of approximately 50 mg/ml. There are no spectral alterations even after a period of 24 hours. Background was subtracted and intensities are normalized to the 1448 cm^{-1} peak. A power of 100 mW was used at an exposure time of 60 seconds for 20 acquisitions.

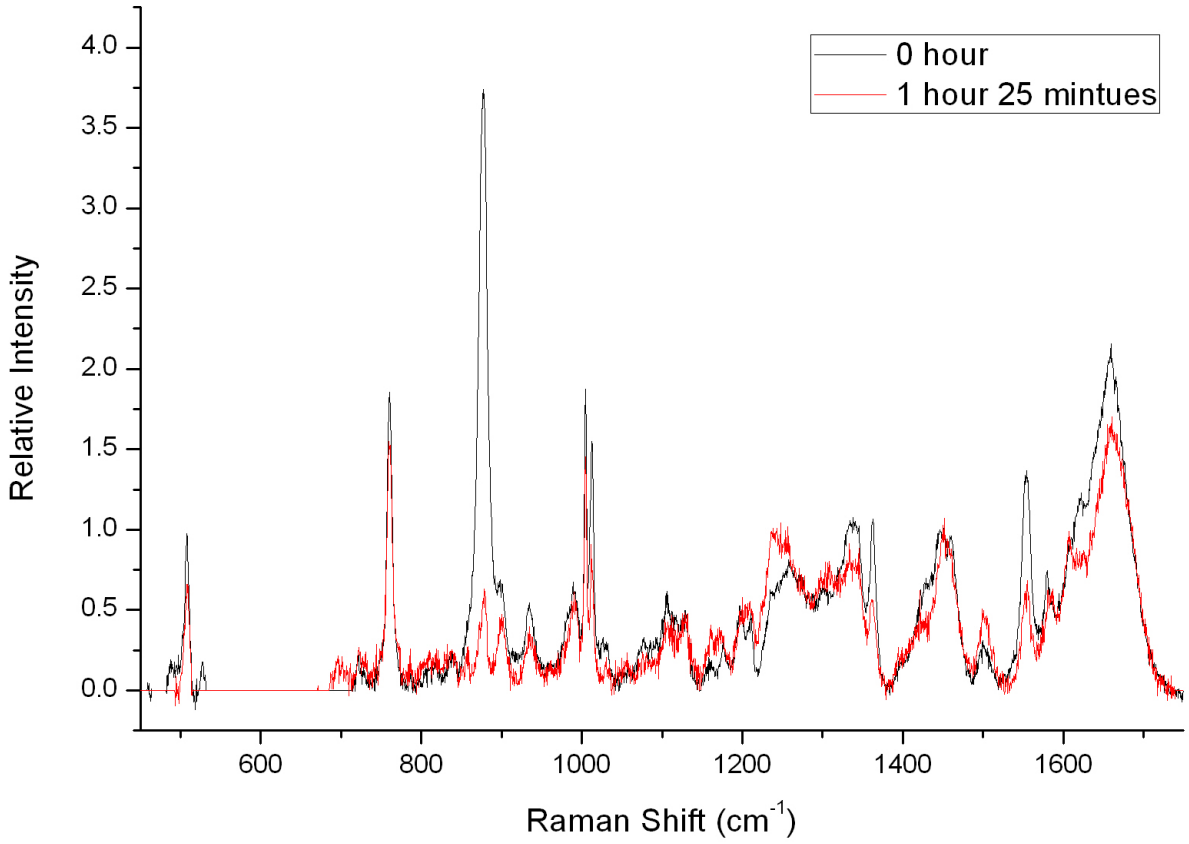

Figure 6.13: This figure is a Raman spectrum of neutralized UltraCare solution at a lysozyme concentration of approximately 50 mg/ml. A relatively strong spectrum with visible spectral alterations was obtained after approximately 1 hour and 25 minutes of lysozyme exposure. Background was subtracted and intensities are normalized to the 1448 cm^{-1} peak. A power of 100 mW was used at an exposure time of 60 seconds for 20 acquisitions.

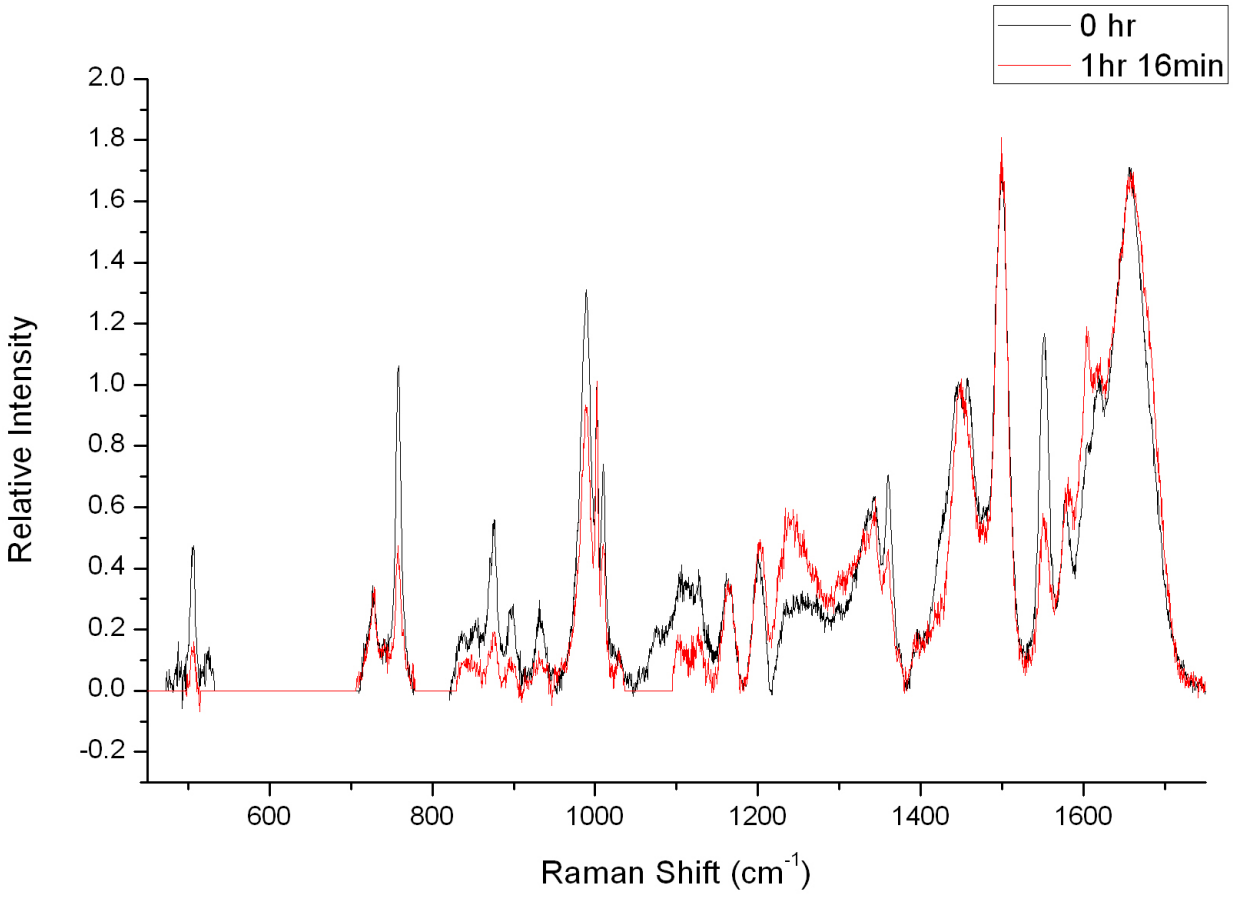

Figure 6.14: This figure is a Raman spectrum of neutralizing UltraCare tablet in PBS, rather than the UltraCare solution, at a lysozyme concentration of approximately 50 mg/ml. Visible spectral alterations were obtained after approximately 1 hour and 16 minutes of lysozyme exposure. Background was subtracted and intensities are normalized to the 1448 cm^{-1} peak. A power of 100 mW was used at an exposure time of 60 seconds for 20 acquisitions.

relatively reliable means of producing acceptable data, there were multiple variations of the experimental methodologies involved.

The main issue with the results that were obtained was that the measured lysozyme activity percentages were much greater than 100%. Many of these activity percentages were also erratic over time and inconsistent when the experiment was repeated multiple times under the exact same conditions. Several methods were explored to determine a variety of effects that may be contributing to these results, such as using different concentrations and preparation methods. Even different techniques for data analysis were attempted to produce more reasonable activity percentages. Different types of lysozyme were also tried, as some batches may contain lysozyme that is statistically partly denatured. This property may result in the protein renaturing when introduced to the contact lens solution. However, the molecules may remain in a denatured state in the PBS solution used for the standard samples. Some of these practices did eventually lead to more consistent data between trials thus improving the reproducibility. However, the issues involving activities greater than 100% were still not resolved during these many attempted solutions.

Another theory that was thought to result in the variable data was the consideration of surface interactions of the protein. If the lysozyme was binding to the walls of any container, the recorded concentrations were no longer valid. This may have caused problems particularly if the contact lens solution samples and the PBS standard samples were made in containers of different materials, such as plastic or glass vials. The size of the containers had to also be considered, since a smaller vial would result in lowering the surface to volume ratio and thus reduce the surface interactions. These binding characteristics could produce a protein concentration gradient across the solution that could skew the assay data.

The other binding effects that may alter the results of the assay are the protein interactions with the surface of the plate well walls used in the experiment. The influence of the well walls was examined by using larger well sizes to lower the surface to volume ratios. Any lysozyme that may bind to the walls could result in the inability for that molecule to perform the function of destroying the bacteria. This would influence the perceived rate of optical density decrease measured by the spectrophotometer. However, the assay results did not improve when changing different well sizes.

One major strategy that was attempted in order to minimize the protein-surface interactions was to include another protein, namely bovine serum albumin (BSA), in the sample solutions. BSA was added at relatively high concentrations with the purpose of competitively binding to the walls of the sample containers and plate wells to reduce any chance of lysozyme molecules binding the surfaces. Figure 6.1 shows the effects of introducing BSA

to samples. Each sample has a constant amount of lysozyme (400ng) dissolved in PBS with a varying concentration of BSA added. All recorded values were compared to standard samples without the addition of BSA to obtain a normalized relative active percent. It is evident that a concentration of 0 mg/ml of BSA results in a 100% activity of lysozyme. When even a concentration as low as 0.01 mg/ml of BSA is introduce to the sample, the measured activity increases above 100% due to the reduced amount of lysozyme that is bound to the surfaces.

BSA Concentration (mg/ml)	Lysozyme Activity (%)
0	100.0 ± 0.8
0.01	110.1 ± 0.5
0.1	110.2 ± 2.1
1	114.0 ± 3.4
5	109.5 ± 1.8

Table 6.1: This table shows the normalized assay results for the different concentrations. The rates of optical density reduction from standard samples without the use of BSA were used to determine an active percentage of the lysozyme.

Although these results do seem to address a problem with the experiment, it may introduce other complications. The introduction of BSA to the solutions also result in the possibility of BSA-lysozyme interactions as well as BSA-bacteria interactions. These additional variables complicate the mechanisms of the experiment even further and were thus deemed undesirable conditions to accurately determine the activity of the lysozyme. The final methodology to correct for the inaccurate activity percentages was to subtract the effect of the contact lens solution itself in destroying the bacteria, which lead to increased rates of optical density reduction.

6.2.2 Final Results

The experimental methods, as described in section 5.2.2, were used to produce the most accurate and reliable data set from the micrococcus activity assay. The graph depicted in figure 6.15 shows the activity assay results of the two MPS ReNu and BioTrue. The percent of the lysozyme that is still functionally active is shown with respect to the time of exposure. The time scale is similar to a sleep cycle, in which the lenses would be cleaned overnight. Both MPS seem to show high activity throughout the time period, indicating that almost all of the present lysozyme remained in an active, native configuration.

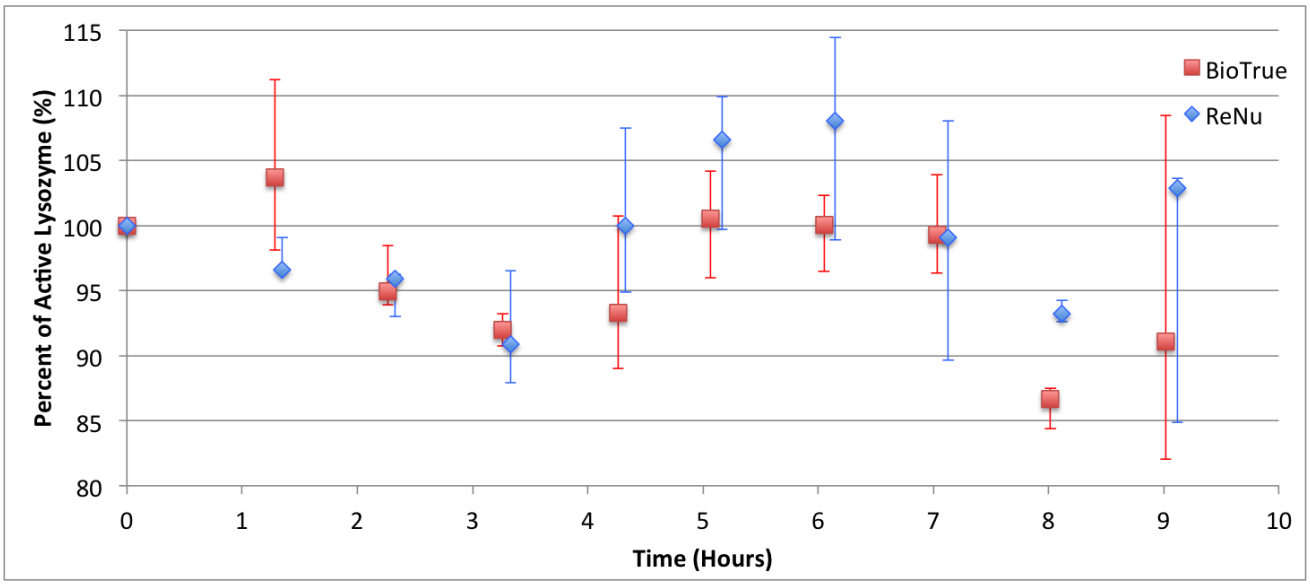

Figure 6.15: This figure shows the percent of active lysozyme in ReNu and BioTrue MPS during a time period resembling a normal overnight cleaning cycle.

The activity assay results of the two hydrogen peroxide systems, ClearCare and UltraCare, are shown in figures 6.16 and 6.17, respectively. These results show that the ClearCare solution shows minimal signs of decreasing lysozyme activity, regardless of whether the solution is concurrently being neutralized or not. The UltraCare solution, however, results in a different effect on lysozyme activity. The non-neutralized UltraCare solution seems to slightly decrease lysozyme activity. Interestingly, when UltraCare is simultaneously being neutralized, the functionality of the lysozyme is greatly decreased.

The apparent denaturing effect of neutralized UltraCare on lysozyme was investigated further. Figure 6.18 shows the activity assay of a solution of PBS with dissolved lysozyme while the UltraCare neutralizing tablet is introduced. This assay experiment is designed to test the effects of the neutralizing tablet ingredients on lysozyme by eliminating the presence of the UltraCare solution. The results seem to indicate that the decrease in lysozyme activity is in fact due to the UltraCare tablet compounds.

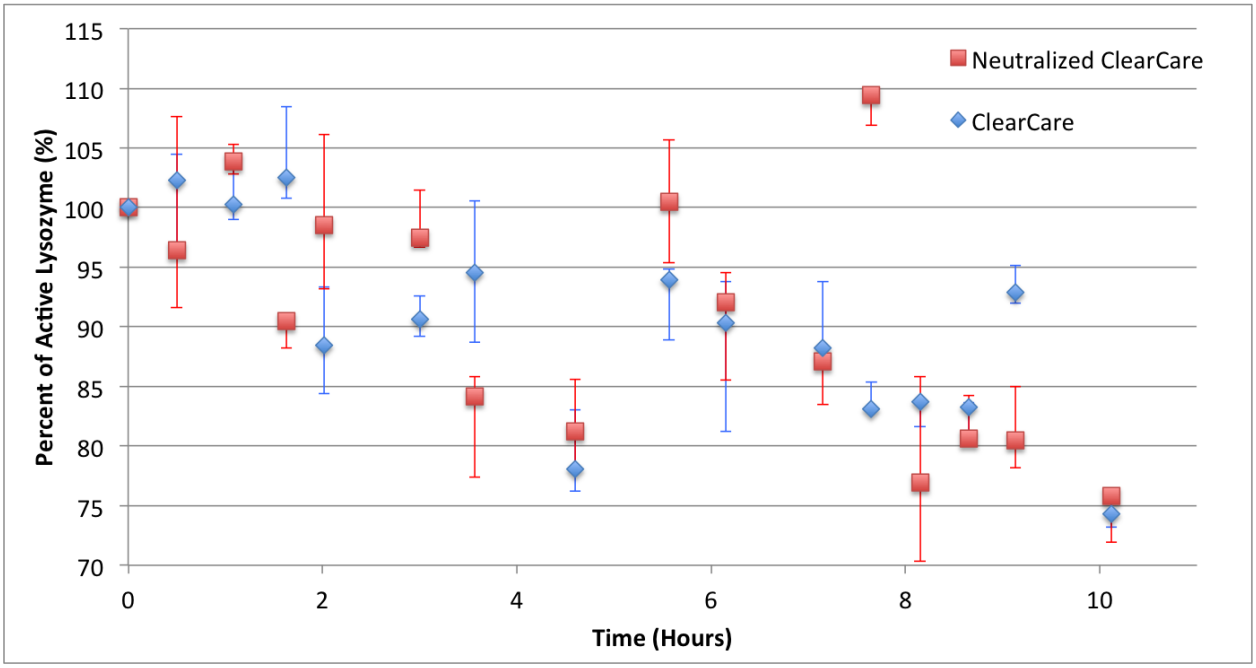

Figure 6.16: This figure shows the percent of active lysozyme in ClearCare, both non-neutralized and while being neutralized, during a time period resembling a normal overnight cleaning cycle.

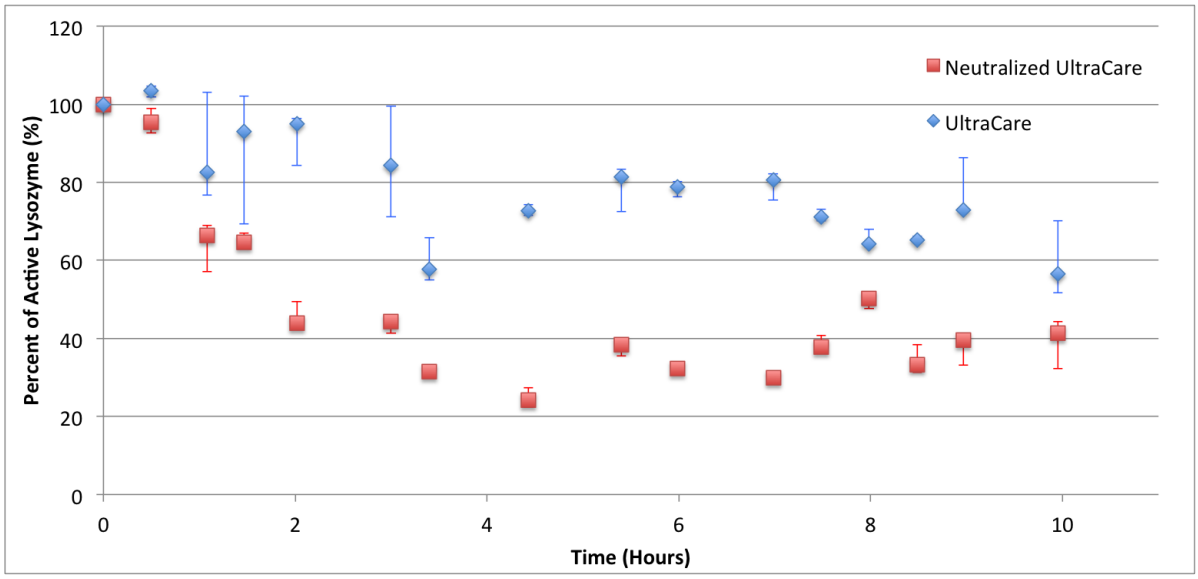

Figure 6.17: This figure shows the percent of active lysozyme in UltraCare, both non-neutralized and while being neutralized, during a time period resembling a normal overnight cleaning cycle.

6.3 Discussion

The Raman spectra of the lysozyme in different contact lens solutions represent the structural alterations that the protein may undergo. The micrococcus activity assays are experiments that indicate the functional alterations of the lysozyme that can occur. Both the structural and functional states of the lysozyme can be used to deduce the denatured state of the molecule.

The lysozyme in the MPS systems that were tested, ReNu and BioTrue, each showed minimal signs of denaturation. The initial Raman spectra of native lysozyme was observed when the protein was first introduced to these contact lens solutions. The Raman spectrum remained unchanged for a period of up to 24 hours, and thus the structure of the molecules seemed to be unchanged. This result is further confirmed by the activity assay data, which indicated that both MPS systems preserved essentially all lysozyme functionality. The absence of either structural alterations nor a loss of activity may be used to conclude that the MPS systems tested do not denature lysozyme.

The Raman spectra and activity assays of the lysozyme in the two hydrogen peroxide systems investigated, ClearCare and UltraCare, seemed to indicate somewhat contradic-

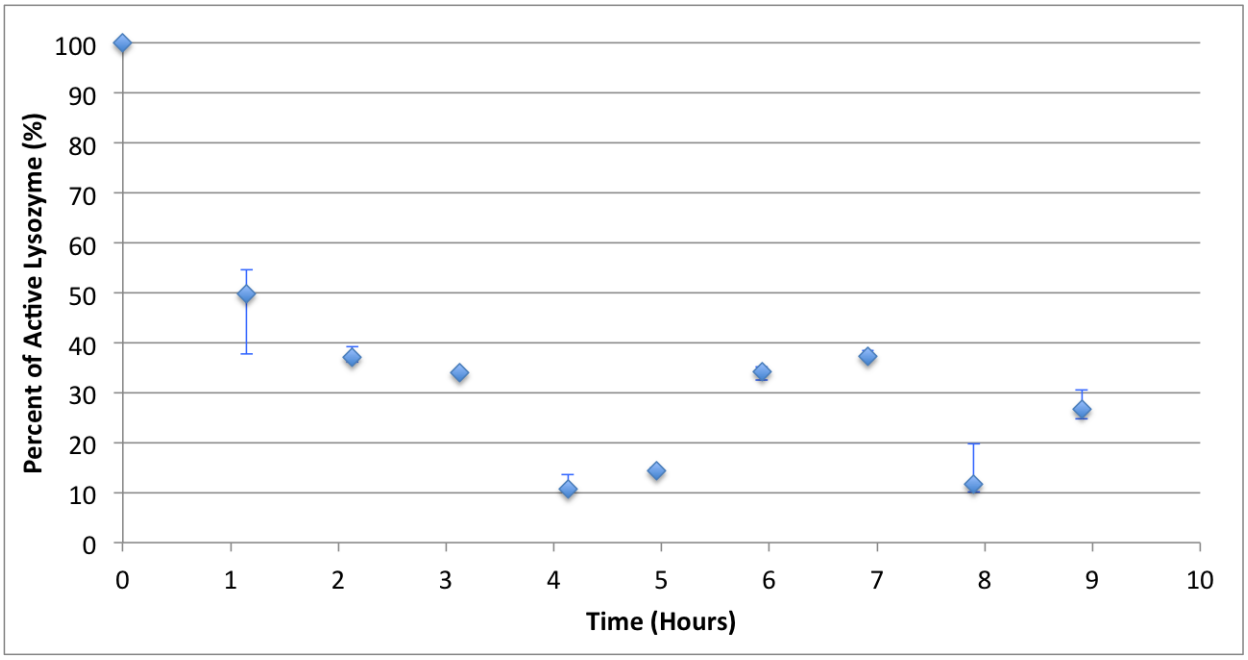

Figure 6.18: This figure shows the percent of active lysozyme in PBS and the UltraCare neutralizing tablet during a time period resembling a normal overnight cleaning cycle.

tory results. The Raman spectrum of lysozyme in the non-neutralized ClearCare solution showed spectral indications of structural changes and thus that the lysozyme had become denatured after a certain period of time. This denaturing state appeared after a period of at most 11 hours. However, weak spectral indications were recorded at earlier times, due to the need for a thick enough layer of precipitate to form at the bottom of the vial in order to produce a strong enough Raman signals. Thus, some of the lysozyme may have most likely become denatured at times earlier than 11 hours. These findings, as well as the early occurrence of white precipitates forming, shows that the lysozyme became denatured due to the ClearCare solution. However, the activity assays produced data showing that the activity of the lysozyme remained consistently high, and thus showed no signs of denaturation.

These results somewhat mimic the data produced by lysozyme in non-neutralized UltraCare. The Raman spectrum of lysozyme indicated a denatured state after only a short period of time (at most approximately 1 hour 40 minutes). The activity assay showed that the majority of the lysozyme had retained functionality (approximately 70% after 10 hours). These results show that the UltraCare solution had only a slight effect on denaturing the lysozyme.

There is a possible explanation to these somewhat conflicting indications of the denatured state of lysozyme in non-neutralized ClearCare and UltraCare. The ability to produce a strong Raman spectrum required relatively high concentrations of the lysozyme in the solutions. These high concentrations may introduce the possibility of protein-protein interactions. As the protein molecule denatures and unfolds, it may interact with other denatured proteins to form aggregates of denatured molecules. The formation of aggregates would also explain the occurrence of the white precipitates observed. When the proteins form aggregates, they become irreversibly denatured and thus will no longer be able to refold back to the native state.

The concentrations of lysozyme used in the activity assays were much smaller than what was required to produce an adequate Raman signal. These small concentrations were also relatively similar to biological tear film lysozyme concentrations. If denaturation of the protein molecules still occurs at these low concentrations solutions, the protein-protein interactions may be minimized and relatively insignificant enough to produce aggregates. This may lead to any denatured protein to be only reversibly denatured, and thus may potentially return to the active native state. This refolding to a native state may result when the protein molecules are introduced to the bacteria mixture, which includes a buffer solution (PBS), involved in the assay procedure. This can occur because the contact lens solution, which may act as the cause of denaturation, would become diluted enough to allow the lysozyme molecules to return to the stable native state.

The two possible causes for this denaturing process in the non-neutralized hydrogen peroxide-based systems was the H_2O_2 concentration and the pH of the solution. The denatured lysozyme was only visible in the Raman measurements at a concentration of 10% or higher (after 24 hours), and at a pH of 2.21. However, both ClearCare and UltraCare only have a H_2O_2 concentration of 3% and a pH of 6.53 and 3.33, respectively. These results seem to indicate that neither the H_2O_2 concentration nor the acidic pH of the two contact lens solutions are the only factors leading to the measured denaturing effect measured by their Raman spectrum. However, they may still contribute to some degree since denaturing occurred at high enough H_2O_2 concentrations and low enough pH levels. Each contact lens solution has multiple ingredients that could be the cause for the denaturation of the lysozyme molecules at the given pH and H_2O_2 concentration.

The Raman spectrum and assay data did, in fact, somewhat agree on the state of denaturation of lysozyme in both neutralized UltraCare and ClearCare. The neutralized ClearCare showed no structural differences in the Raman spectrum even after 24 hours of exposure. The activity assay of lysozyme in this solution also produced results that indicated a very high level of protein functionality throughout a typical sleep cycle. However, as previously discussed, the preservation of high protein activity does not necessarily indicate that the lysozyme is in a native state while exposed to the contact lens solution. The lysozyme may simply be in a reversibly denatured state while exposed to the hydrogen-peroxide system. The lysozyme may refold to an active state when the contact lens solution is diluted after being introduced to the bacteria solution in the assay experiment.

The Raman spectra of the lysozyme, however, remained unaltered throughout the exposure, even at high concentrations in which aggregation may result in irreversible denaturation. This indicates that the protein does not undergo structural alterations, and may be concluded to not be in a separate reversibly denatured state while exposed to the contact lens solution. These experiments show the lysozyme retained both the functionality and structural configuration of the native state. Thus, it may be concluded that the lysozyme does not become denatured during the neutralization process in ClearCare.

The neutralized UltraCare showed spectral indications that the protein had undergone structural changes after no longer than approximately 1 hour and 25 minutes. The activity assay also showed that the functionality of the lysozyme greatly decreased during the normal cleaning cycle. Both experiments indicate that some form of denaturation had occurred due to the neutralization process in a time period significant to a regular cleaning cycle.

Interestingly, the neutralizing tablet was also shown to reduce activity of the protein in the absence of UltraCare. In addition, the Raman results were indicative of the lysozyme

transitioning to a random coil structure, and thus evidently were denaturated. These results lead to the conclusion that some component in the tablet must be causing the decrease in activity. A main chemical found in these tablets is HPMC, as previously discussed in section 4.2.1. One possible explanation of this assay data would be that an ingredient such as HPMC could cause denaturation, and thus the inactivity and structural alterations of the protein. The Raman results, in combination with the low activity measured at relatively low concentrations, indicate that the protein seems to be in an irreversibly denatured state while exposed to the UltraCare neutralizing tablet.

One main difficulty encountered in producing results that are most relevant for lysozyme found in tear film was the need to use high concentrations of the protein to acquire sufficient Raman signals. This may increase the occurrence of aggregation and thus produce irreversibly denatured protein. One attempt to instead use biologically similar concentrations of lysozyme while producing an adequate Raman spectrum was the use of SERS, as described in section 2.7. Industrial manufactured SERS substrates, purchased from Integrated Optics® (Vilnius, Lithuania), were used to enhance the Raman signal produced by a lower concentration of lysozyme.

Unfortunately, this technique did not produce strong enough Raman signals at the given low lysozyme concentrations (results not shown). The technique of SERS may be perfected using different methodologies in this application. However, any result obtained would not necessarily indicate the correct structural configuration of the lysozyme while exposure to the contact lens solution. This is due to the inherent surface-protein interactions needed to perform SERS. Thus, the introduction of these variable surface interactions could alter the state of the protein and would not reliable characterize the protein while solely dissolved in the solution.

The other attempt to create Raman signals of the protein at low concentrations was to use centrifugation. However, this technique produced similar spectral results indicating denaturation as compared to the prior high concentrations of lysozyme that were used. The problem with this method, however, is that the centrifugation process resulted in aggregation of the protein. Consequently, centrifuging allows the clumping of protein to create irreversibly denatured molecules. Thus, this experiment cannot be used to accurately model the state of the protein while exposed to the different contact lens solutions.

6.4 Conclusion and Future Work

The denatured state of lysozyme was investigated by determining both the structural configuration as well as the functionality of the protein. This link between molecular

conformation and activity is made with the use of Raman spectroscopy and micrococcus activity assays, respectively.

The multipurpose solutions ReNu and BioTrue both showed no indications of denaturing lysozyme in a normal cleaning cycle. Similar results were also found when lysozyme was exposed to the hydrogen peroxide-based system ClearCare while the neutralizing process occurred. When the solution was not neutralized, there were structural indications that some lysozyme had denatured, taking no longer than 11 hours. The activity of the lysozyme remain consistently high throughout a 10 hour period. The other hydrogen peroxide system tested, UltraCare, showed early indications of structural alterations for both the neutralized and non-neutralized solutions. However, the assays indicated relatively high activity for protein exposed to the non-neutralized UltraCare solution, while the neutralized solution produced lysozyme with extremely low activity.

The discrepancies between the observed physical alterations to the molecular structure while showing relatively high protein functionality may be due to the high concentrations of lysozyme needed to obtain the Raman spectra. These high concentrations may allow for the prevalent occurrence of protein aggregation, and thus cause for the irreversible denaturation of the lysozyme. The relatively low, and biologically similar, concentrations of the lysozyme may allow for reversible denaturing of the molecule, in which a refolding to the native state can occur when diluted in the assay experiments.

Both the Raman spectra and assay results indicated a denatured state of lysozyme while introduced to the neutralized UltraCare solution, as well as a neutralized solution without UltraCare present. These results seem to indicate that the denaturing effect may be caused by some component of the UltraCare neutralizing tablet. Future work that may be done to compliment this research is to further investigate any denaturing effects that may occur while lysozyme is exposed to the separate constituents of the tablet, in particular the HPMC component. This may be accomplished by simply exposing lysozyme to the individual compounds separately and determine the denatured state using Raman spectroscopy and activity assays as performed in this thesis research. As discussed in section 6.2.1, surface interactions of the protein with walls of the containers and plate wells can alter the assay results. This effect could also be further studied using protein such as BSA and different surface to volume ratios.

Other studies may also be employed using Raman spectroscopy to characterize the state of proteins in the contact lens cleaning process. Research could be done to investigate the state of other proteins that are present in tear film solutions, such as albumin or lactoferrin, while exposed to contact lens solutions. Another such study that may be relevant to this current research would be using Raman spectroscopy (in combination with activity assays)

to investigate the structural state of the lysozyme while absorbed to a variety of contact lens materials. This would provide a more direct analysis of the state of the proteins that are introduced to the ocular tissue.

Part III

Additional Applications of Raman Spectroscopy

Chapter 7

Polystyrene Nanoporous Material

The following chapter will provide a brief synopsis for research conducted on a separate project. This work was undertaken for another PhD student (Chad Daley) and this chapter is based on a paper to be submitted for publication shortly entitled 'Nanoporous polystyrene prepared through the selective removal of low-Mw component in polystyrene blends' [24]. This research involves dissolving away a smaller chained polystyrene molecules in a blend mixture to produce a nanoporous polystyrene material. The specific work performed for this project was using Raman spectroscopy to determine the efficiency of this dissolving process by identifying the relative ratios of different polystyrene molecular weights present. Other various properties of the nanoporous material were also investigated in this research paper using other techniques, such as atomic force microscopy (AFM), scanning electron microscopy (SEM), and nulling ellipsometry, however, only the relevant Raman measurements will be discussed in the following sections.

7.1 Introduction

Nanoporous materials find applications in a wide variety of fields due to a high internal surface area. Their properties may be tuned for utilization in areas such as thermal insulation, gas separation and storage, optical coatings, and chemical absorption. The main techniques for the production of these materials are lithography, the sol-gel method, and leeching schemes. The simplest approaches involve leeching techniques. However, they require the use of materials that are immiscible such that for a particular solvent, one component will act as a solute while the other component does not.

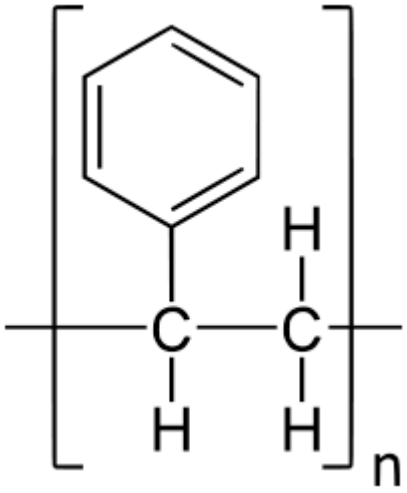

Figure 7.1: This figure depicts the monomer styrene. Polystyrene is composed of many of these monomers linked in a long chain [109].

The techniques described in this research can be used to produce a polystyrene (PS) thin film material with nanopores with diameters 10-100 nm. PS is a synthetic polymer made of long chains of the monomer sytrene, as shown in figure 7.1. The underlying principle that allows for this leeching process to occur is the relatively high entropic gain for smaller chains released into solution rather than lower chains. The particular solvent used has unfavourable enthalpic influences with respect to the dissolving of these polymers. This allows for the larger PS chains to be immiscible, while the shorter PS chains can dissolve in the solvent due purely to the entropic interactions. This methodology can be used for any polymer with a blend of contrasting chain lengths and a solvent with the correct enthalpic considerations.

7.2 Experimental Methods

The samples were all prepared by a PhD student (Chad Daley) which included first dissolving the PS in toluene at concentrations of ¡4% polymer by mass. The two molecular weights (M_w) of PS used were 627,000 g/mol and 600 g/mol and were prepared in different blend ratios from a low M_w fraction of 0.1 to 0.9. The polymer thin films were made by spin coating the PS solutions onto quartz discs at 2500 RPM. These ‘cast’ samples, which

contain both the low and high M_w PS, were then converted to a 'leeched' state. This was done by the successive submerging of the cast samples into two separate vials of n-heptane (HPLC grade, Fisher Scientific Canada) for 60 seconds each and then dried under a flow of N_2 gas.

To distinguish the low and high M_w PS molecules with the Raman spectrometer, the high M_w polymer chains are fully deuterated, in which the hydrogen in the molecules are substituted with deuterium. The Raman spectra of the blend samples can then be used to measure the efficiency of the leeching process by investigating the relative spectral peak intensities representative of each of the PS chain lengths present. The Raman spectra were recorded using the same experimental setup as described in section 5.1.

7.3 Results

The deuteration of the high M_w results in several alterations in its characteristic PS Raman spectrum. One such variation is apparent in the shifting of the normal, hydrogenated, PS peak of 3050 cm^{-1}, representing a C–H radial stretching mode in the benzene ring [90], to 2290 cm^{-1} when deuterated. A measurement of the amounts of high and low M_w polymer can be determined by finding the relative intensities of these two corresponding peaks.

Figure 7.2 shows the fraction of the low M_w plotted against the intensity of the deuterated high M_w peak (at 2290 cm^{-1}) normalized to the combined deuterated and hydrogenated peak intensities at 2290 cm^{-1} and 3050 cm^{-1}, respectively. Both the cast and leeched samples are plotted, with the solid lines representing the expected behaviour. The inset image shows the Raman spectra of the PS film before and after the samples are leeched for a 0.5 low M_w fraction.

7.4 Discussion and Conclusion

The cast samples show a relatively good correspondence with the expected results. The leeched films did not show Raman peaks indicating the presence of the hydrogenated PS for low M_w fractions greater than 0.3. A reduced leeching effect was observed for 0.2 and 0.3 low M_w fractions. A fraction of 0.1 subsequently showed no indication of a change in the relative intensities between the deuterated and hydrogenated peaks. The interpretation of this result is that at these low concentrations of shorter chains, the molecules of the n-heptane cannot infiltrate the film to dissolve the low M_w chains.

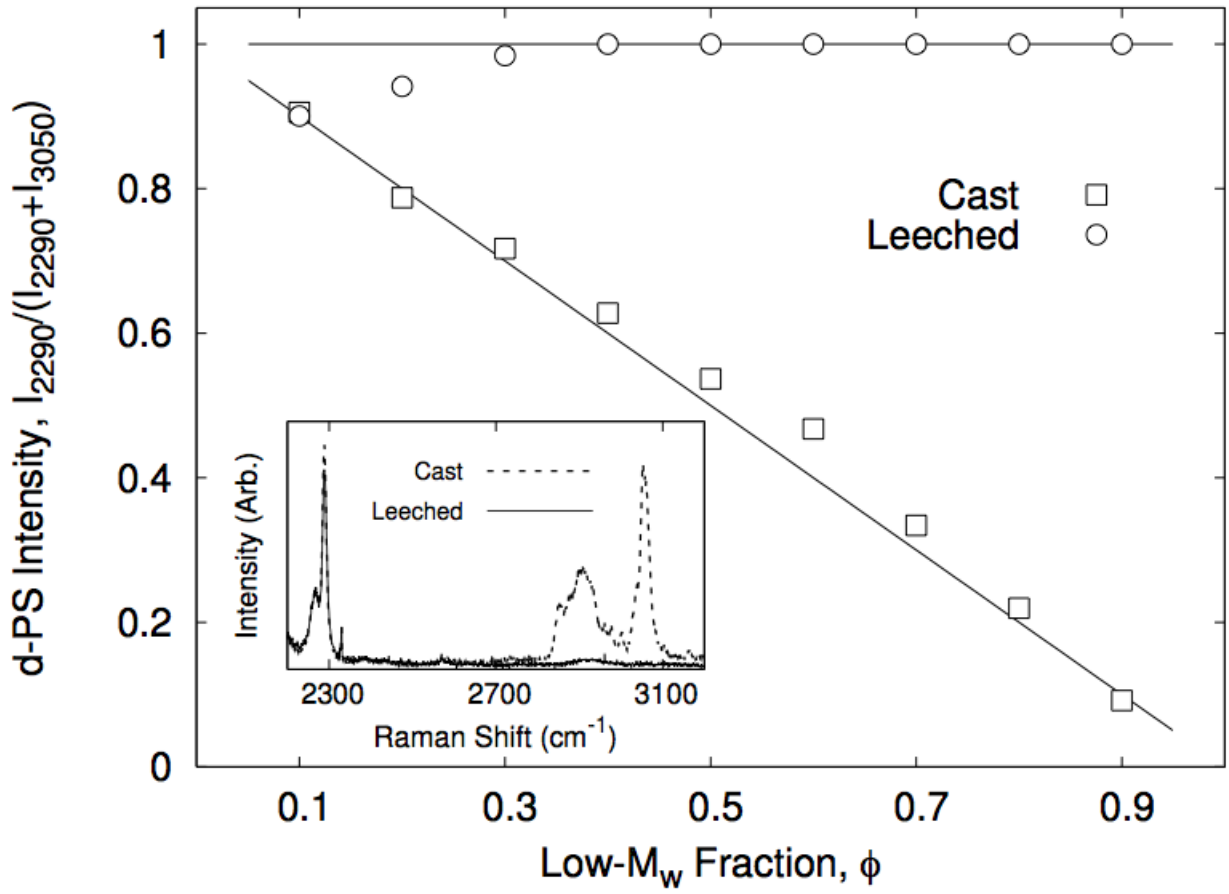

Figure 7.2: This figure depicts the measured relationship between the low M_w hydrogenated PS fraction and the normalized intensity of the deuterated high M_w. Both the cast and leeched sample results are shown. The solid lines represent the ideal behaviour. Inset image: An example Raman spectra showing the recorded spectral peaks before and after leeching for a low M_w ratio of 0.5. [24].

This novel approach to producing nanoporous films is considered a leeching technique. The aspects unique to this original leeching procedure is that the initial system is both stable and miscible. Raman spectroscopy has been shown to be a useful tool in determining the relative concentrations of the materials in a sample. The use of deuteration can evidently be used to even distinguish the relative amounts of separate components that would otherwise produce identical Raman signatures.

Chapter 8

Graphene Raman Signal Enhancement by Silver Nano Pillars

This chapter is dedicated to describing research performed for a separate graduate group in the Department of Electrical and Computer Engineering. Raman spectra were recorded for a project led by a PhD student (Reza Khorasaninejad). The following sections provide a brief summary of the research that resulted in the paper entitled 'Highly Enhanced Raman Scattering of Graphene using Plasmonic Nano-Structure' which was published in Scientific Reports of October 14, 2013 [57]. The graphene samples were also investigated using atomic force microscope (AFM), however, the following sections only discuss the relevant Raman measurement results.

8.1 Introduction

The relatively recent discovery of graphene has led to applications in a variety of fields, such as physics, engineering and nanotechnology, due to its exceptional properties including extremely high thermal and electrical conductivity. Graphene is essentially a single atom thick layer of carbon atoms bonded in a honeycomb pattern, as depicted in figure 8.1 Graphene can display unique (non-linear) properties that may be exploited to create optical logic gates and switches. These optical characteristics even have the capability to be tuned with the introduction of an external electric field [10]. The efficacy and sensitivity of the photo-detection required for these particular optical applications can be greatly increased by improving the interaction of the graphene with light.

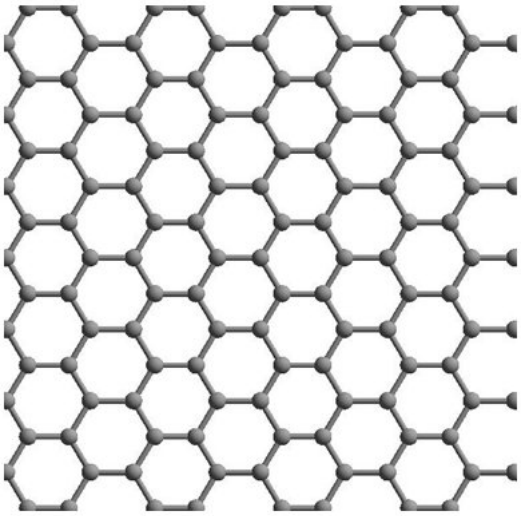

Figure 8.1: This figure depicts graphene as a honeycomb pattern of bonded carbon atoms [81].

A major methodology that has been shown to increase these effects is by the use of metallic structures to enhance the absorption and emission of photons. These enhancements involve incorporating the graphene layer with surface plasmons. Incident photons may become coupled with these plasmons to produce the enhancement effect. The mechanism by which these enhanced interactions occur are essentially the same process involved in the SERS technique, as described in section 2.7. The enhancement of Raman signatures can provide information on the electric field enhancement within the graphene. In particular, the ability for Raman signals to be used in certain optical devices have been shown for devices such as silicon nanowires and waveguides [22].

8.2 Experimental Methods

All samples were prepared by another research group. These samples included periodic, sharp nano-structures to create a localized enhanced electric field. Figure 8.2 shows a schematic of the tested sample structures. These configurations include a two-dimensional array of silver nano-structures which have either a ring or crescent shape. These structures are then embedded on top of a silicon dioxide substrate coated with a thin layer of gold approximately 30nm. The silver nano-structures were made at a constant height of 75 nm. The nano-pillars have a spacing 100 μm. The ring structure has previously been used

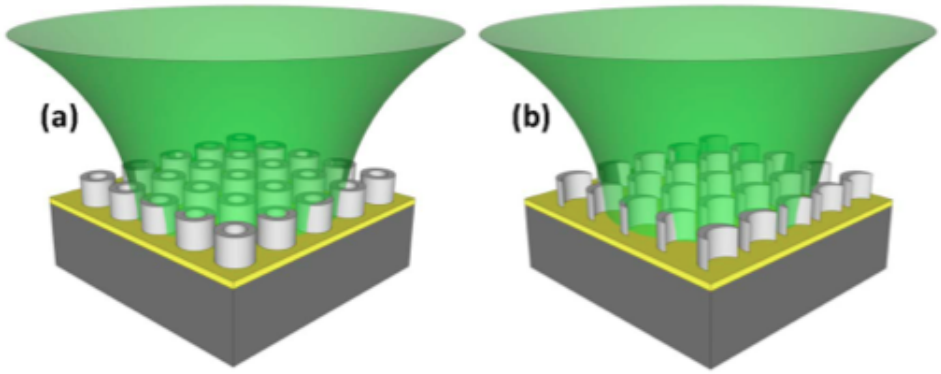

Figure 8.2: Figure a.) and b.) depict a diagram for the tested samples with either a ring or a crescent shaped periodic silver nano-structures embedded on top of a gold-coated silicon dioxide substrate. [57].

to show enhancement effects [1], while the crescent shape was chosen to allow for sharp tip features. The layer of graphene is then created on top of these silver nano-structures. Multiple samples were constructed with varying inner and outer diameters in order to determine the largest possible enhancement available.

The plasmons are localized on the surface of these structures, and so the degree of Raman enhancement will be dependent on the gap size between the silver nano-pillars and the graphene. The crescent shaped pillars allow for a smaller gap due to the lack of material creating space for which the graphene may access. The gold coating acts like a mirror, allowing for the light to be reflected with a phase shift that creates a hot spot of enhancement located at the top of the pillar structures, and thus closer to the graphene.

The Raman measurements were obtained by taking spectra from several spots on each sample array. The focal spot size used was 1 μm in diameter. The recorded Raman spectra was attained using a power of 1 mW at an exposure time of 15 seconds and summed over 10 acquisitions. All Raman spectra were measured with the same experimental setup as described in section 5.1.

8.3 Results

Figure 8.3 shows the optimized Raman spectra of the graphene samples on the ring and crescent patterned silver nano-structures, as well as the silicon dioxide substrate. The

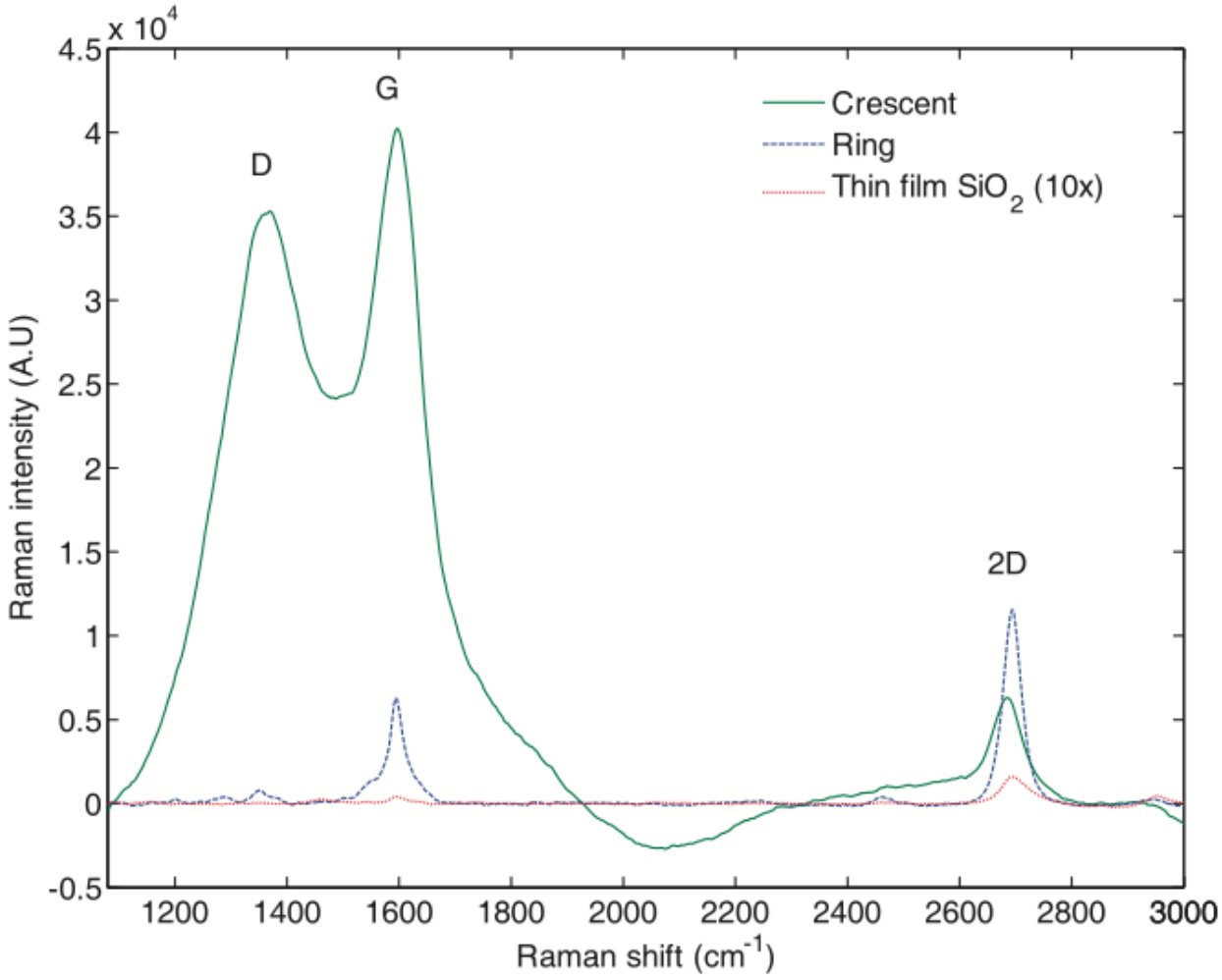

Figure 8.3: The enhanced Raman spectra of graphene due to the ring and crescent shaped nano-structures [57].

ring structure that gave these maximally enhanced Raman signals had an outer and inner diameter of 270 nm and 180 nm, respectively. The crescent shaped structure which gave the optimal signal enhancement had an outer and inner diameter of 220 nm and 130 nm, respectively, with a maximum width of 45 nm.

The two most prominent peaks in the characteristic graphene spectra are the peaks at 1600 cm^{-1}, called the G-peak, and at 2700 cm^{-1}, called the 2D-peak. The 2D-peak has a greater peak intensity than the G-peak for graphene on silicon dioxide and on the silver ring structure, which signifies that the graphene is a single layer. Another peak present at 1466 cm^{-1} is a weaker mode called the D-peak and shows that there are defects in the graphene layer. There were no substantial spectral changes when multiple measurements were made at different spots on the sample arrays. The crescent shaped structures produced a D-peak at 1350 cm^{-1} with a greatly increased intensity similar to that of the G-peak. This peak also appears as a very weak signal for the graphene on the ring structure, and represents sharp folds in the graphene sheet.

There were several enhancement features that occurred for the silver nano-structure samples. One common element was that the G-peak received a much larger enhancement than the 2D-peak. Another consistent result is that the crescent patterned array produces a much greater difference in the spectral enhancement factor than the ring structures. The enhancement from the ring structure decreases as the diameter is reduced. The Raman signal of the 2D-peak is enhanced by a factor of 73 and 38 for the ring and crescent structures. respectively. However, the G-peak was enhanced by the ring and crescent patterns by a factored of 154 and 890, respectively. These factors were found by using a reference spectral peak intensity obtained from graphene only on the silicon dioxide substrate.

8.4 Discussion and Conclusion

As previously discussed, the crescent pattern resulted in a much greater enhancement in the G-peak than the ring pattern. The particular enhancement characteristics were also different for each of the two types of nano-structures. These effects were further investigated by the comparison of the experimental results with calculated electric field distributions. These calculations were performed by Reza Khorasaninejad and are further discussed in the aforementioned published journal paper describing this research [57]. Different aspects of the experimental observations were mostly explained using this theoretical modeling of the electric fields present in the silver structures. A significant enhancement in the G-peaks and 2D-peaks when the graphene is present on the nano-structures compared to on only

the silicon dioxide seems to indicate the involvement of surface plasmons, as anticipated by the theoretical model. These results also indicated that the enhancement effects did not incrementally increase with the diameter of the structures, but instead the enhancement could be maximized at an optimal size of structure.

The gap spacing between the nano-structures and the graphene is also one of the main variables contributing to the enhancement. This is due to the confinement of the electric field to the surface of the nano-structures. It is thus suggested that Raman signal increase will highly depend on the distance between the graphene and the nano-structures. The experimental data confirmed the theoretical model predicting that the crescent patterns produce a greater enhancement than the ring geometry for the same gap distance between the graphene and structures. The large variance for the enhancement factors between that of the ring and crescent shaped structure can be attributed to the larger gap sizes that occur between the graphene and the silver for the ring structures than the crescent patterns.

The computational models also predict that the enhancement due to the crescent shape will decrease much faster for the G-peak compared to the 2D-peak as the gap between the graphene and nano-structure is reduced. This, again, is confirmed by the recorded experimental results. However, the experimentally observed enhancement was smaller than the model predicted, which may simply be a result of any imperfections in the crescent shape for the fabricated structures. The simulations incorporated a crescent shape with ideally sharp edges, while the manufactured sample structures may have resulted in more rounded edges. However, due to the still relatively sharp tips of the crescent pattern in the arrays, the graphene becomes slightly deteriorated. This effect resulted in the large D-peak that appeared in the spectra. The crescent spectra also produced broadened peaks, which are another indication of possible defects in the graphene. These sharpened corners of the crescents also can cause for the folding of the graphene and thus destroy the symmetry of the graphene nano-structure. This consequence of the crescent peaks were also confirmed by SEM scans (images are not shown).

In summary, the experimental data collected for this research included the enhancement effects due to silver ring and crescent patterned nano-structure. The highest enhancement of the graphene spectra consistently appeared on the G-peak, rather than the 2D-peak. This novel approach in using crescent shaped structures produced the optimal enhancement of the G-peak by a factor of 890, with respect to graphene on silicon dioxide. These effects corresponded to the expected predictions made by theoretical modeling of the electric field distributions.

These experimental results have shown that Raman spectroscopy can be used to in-

vestigate optical devices comprised of graphene on plasmonic nano-structures. Raman measurements can even be useful in determining different structural heights as well as characterizing the folding of graphene, which may provide an easier and quicker alternative to other surface characterization techniques such as AFM or SEM. The relatively large enhancement factors found in this research may be relevant in applications for devices containing interactions involving graphene with light, such as solar cells, nonlinear optical devices, optical modulators, and photo-detectors.

Chapter 9

Photo-Thermal Effects of GaAs Nano-Structures

This chapter will give a brief description of the work done for another research project implemented by a PhD graduate student (Jaspreet Walia) from the Department of Electrical and Computer Engineering. This research led to a paper by this group named 'Diameter Dependent Photo-thermal Effects in Vertically Etched GaAs Nanowire Arrays' [106] that has been accepted to the 2014 IEEE International Conference on Nanotechnology (IEEE-NANO) held in Toronto, ON. The main subject of this research investigates the Raman spectral properties of etched nano-structures of GaAs. The work performed for this research was obtaining the Raman spectra of the various GaAs samples.

9.1 Introduction

The potential applications of photo-thermal devices span a variety of technological domains such as bio-electronics [70], laser therapeutic agents for specific microorganism elimination [71], and energy conversion in photo-thermal-electrical (PTE) devices [19]. These technologies all benefit from a greater efficiency in converting incident radiation into heat. In particular, PTE devices convert excitation photons into heat, which is then converted to electricity. Devices such as these provide a potential method for solar energy collection. Theoretically, higher efficiency for these thermoelectric devices is achieved for materials with a high electric conductivity and a low thermal conductivity. PTE devices specifically require a high efficacy in generating heat from the absorption of incoming light.

Several different structures have been shown to increase the photonic absorption of certain materials. One such structural design that is known to produce an increase in the optical absorption properties of the material are vertically oriented nanowire arrays [44]. This effect is mostly due to a resonant coupling with optical modes. In particular, semiconductor nanowires are of great interest for use in thermoelectric devices due to their unique properties. One such material that is a candidate for use in the production of semiconductor nanowires is gallium arsenide (GaAs). The bulk form of GaAs has a thermal conductivity of 54 $Wm^{-1}K^{-1}$. However, GaAs nanowires have been shown to have a thermal conductivity of 8-36 $Wm^{-1}K^{-1}$ [98]. GaAs also has a thermal conductivity that is naturally lower than commonly used Si, and thus is a superior prospect for use in thermoelectric devices.

The research presented in this chapter investigates the dependence of the nanowire size on photo-thermal effects in GaAs. Several diameters of GaAs nanowires were examined in order to obtain an optimal size for increasing the temperature of the material. This is done by using the Raman spectral features of the nanowires to determine their temperature. Certain shifts in the Raman spectral peak positions can be used to indicate the localized temperature of the sample as a function of diameter of the nanowires.

9.2 Experimental Methods

The arrays of GaAs nanowires were constructed using an etching technique called inductively coupled plasma reactive ion etching (ICP-RIE), as described in the literature [29]. This work was done by another research group to produce the relevant samples. The GaAs wafer composed of eight separate etched arrays of nanowires with diameters sizing from 50 nm to 155 nm at 15 nm increments with a uniform vertical height of 1.0 μm. Each nanowire diameter size were created in a square lattice (100 μm $\times$ 100 μm) with a 400 nm pitch.

The Raman measurements were made using the experimental setup described in section 5.1. The focal spot size obtained for each scan was on the order of 100 μm^2. The power of the incident radiation was 1 mW to produce a intensity on the focal spot of 10 W/mm^2 and was polarized along one of the lattice directions. Each spectrum was recorded using an exposure time of 45 seconds and summed over 15 acquisitions.

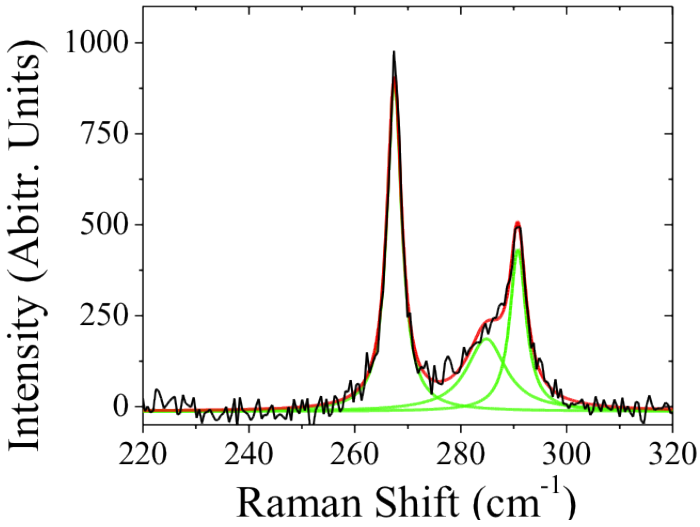

Figure 9.1: The spectral decomposition of the Raman spectrum obtained from an array of 50 nm diameter nanowires. The fit is achieved by modeling the three different modes each as separate Lorentzian functions [106].

9.3 Results

Each Raman spectrum for the varying diameters of nanowires was fitted using Lorentzian functions to model the spectral features. This allowed for a more accurate measurement of the peak positions and the relative peak intensities. The Raman spectra has peaks at 267 cm^{-1} and 290 cm^{-1} corresponding to scattering from transverse optical (TO) and longitudinal (LO) phonons, respectively. Scattering from surface optical (SO) phonons results in a third shoulder peak.

Figure 9.1 shows an example Raman spectrum of the 50 nm diameter GaAs nanowires with three separate Lorentzian fitting functions corresponding to the three distinct spectral peaks. These functions fit well to the TO (centered at 291 cm^{-1}) and LO (centered 267.5 cm^{-1}) modes with spectral widths of 3 cm^{-1} and 3.3 cm^{-1}, respectively.

Each of the Raman spectra for the eight different nanowire diameters are shown in figure 9.2. The spectrum of the bulk GaAs without etched nanowire structures is also shown. The TO phonon peak at 267 cm^{-1} is not present in the bulk spectrum due to being disallowed by the Raman selection rules for GaAs. This indicates the GaAs wafer remained smooth after the etching process. The surface roughness introduced by the etching process, as well

as crystalline damage of the sidewalls, reduces the influence of this selection rule to allow for scattering by the TO phonons.

The TO and LO modes can be used to provide information on the localized temperature of the arrays. The relationship between the local temperature increase of the GaAs nanowires has been shown to be dependent on the spectral shifts of the TO and LO phonon scattering peaks [7, 47]. This correlation can be expressed by the linear relation

$$\frac{d\nu}{dT} = 0.016\,\mathrm{cm}^{-1}\mathrm{K}^{-1}$$

in which $d\nu/dT$ is the rate of change of the wavenumber shift with respect to temperature, T. This relationship can be used to show that the fitted parameters for the 50 nm diameter nanowire array shown in figure 9.1 did not undergo heating effects from the excitation radiation and are in agreement with values from the bulk GaAs at a temperature of 300 K.

Figure 9.3 plots the central peak positions of the TO and LO modes with respect to the varying nanowire diameter. The Raman peaks show red-shifted peak positions and spectral broadening for each of the modes. The maximum shift and broadening for both peaks was observed at a diameter of 95 nm. This diameter of nanowire also resulted in the greatest Raman intensity, as evident in figure 9.2.

9.4 Discussion and Conclusion

The top sections of the nanowires are expected to become heated the most due to the vertical orientation of the structures relative to the excitation radiation source. This is because the TO and LO modes occur from scattering effects on the side walls and top features of the nanowires, respectively, each of which is expected to have a separate local temperature. This is evident as the TO spectral peaks only appear for sections of the wafer with the etched nanowire structures (and not the bulk). The variability of the spectral peak intensities for different nanowire diameters are thus indicative of the importance of these photonic modes in increasing the temperature by means of an incident light source.

Other studies have shown that the highest local temperatures for a particular incident radiation intensity are achieved in nanowires with the smallest diameter. This effect is usually attributed to the decrease in thermal conductivity as the diameter is reduced [97]. However, this current research indicates that GaAs nanowires that are vertically oriented with a diameter of 95 nm had an optimal heating effect for a given input light intensity,

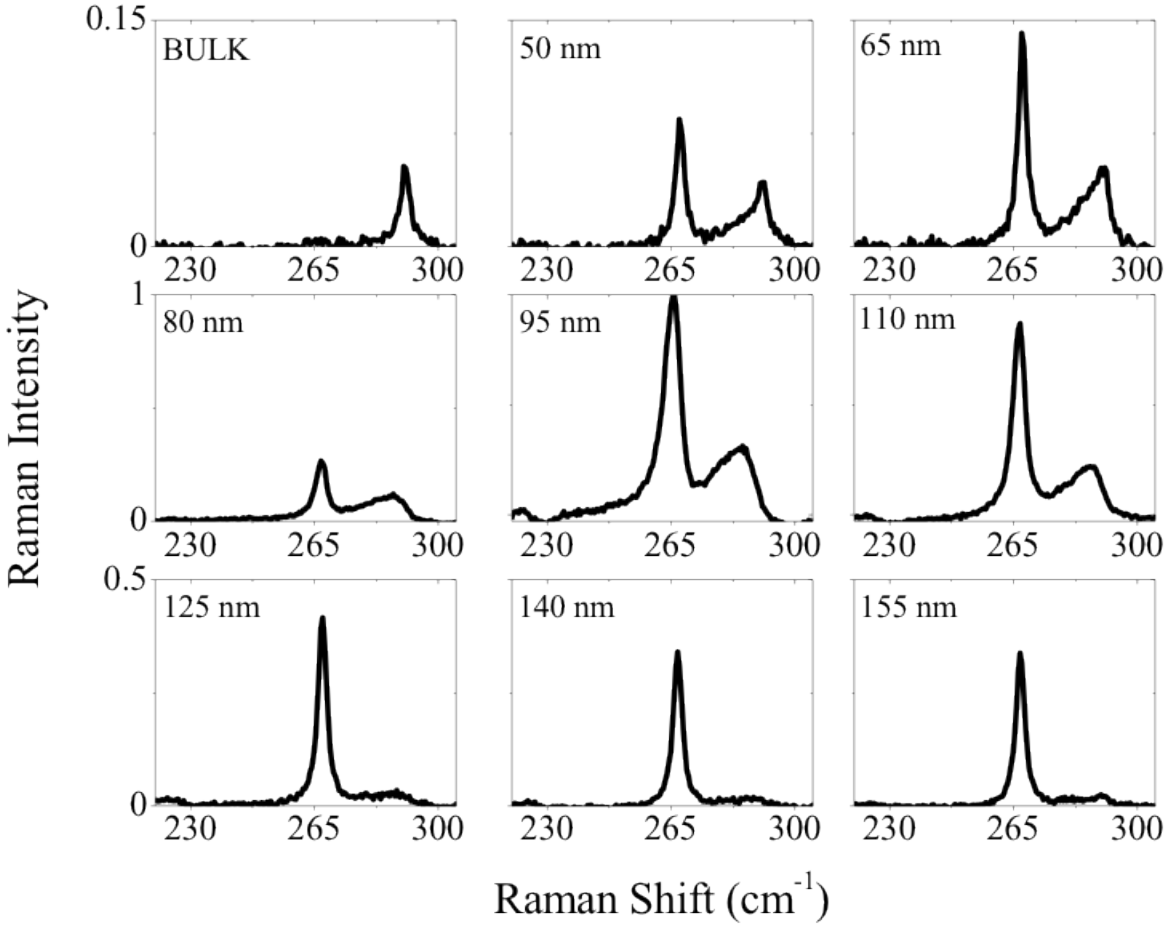

Figure 9.2: The eight separate Raman spectra for the different nanowire diameters ranging from 50 to 155 nma are depicted. The Raman spectrum of the bulk GaAs without a nano-structure is also shown [106].

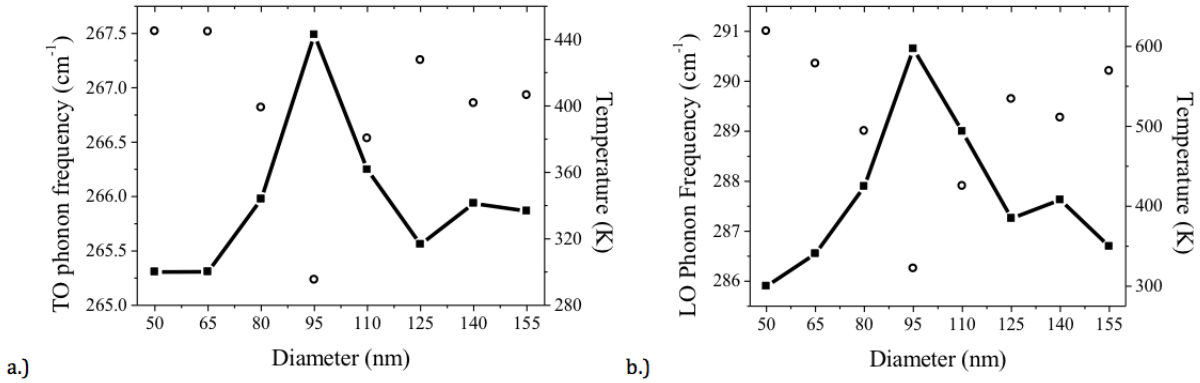

Figure 9.3: The central peak positions of the a.) TO and b.) LO phonon modes as a function of nanowire diameter (plotted as open circles). The corresponding calculated temperatures are also shown (plotted as the solid lines) [106].

at a wavelength of 532 nm. Thus, a decrease in diameter is conversely not always superior in generated more heat.

The enhancement of the Raman scattering at the nanowires correspond to strong electric fields localized within the nano-structures to produce the observed high temperatures. This effect is similar to the mechanisms behind the SERS technique of enhancement, as discussed in section 2.7. The apparent resonance effect at the particular nanowire diameter seems to have been observed due to the use of much smaller increments of diameter differences being tested, rather than the large increments used in prior studies.

These results also reassert that GaAs nanowires experience a much lower thermal conductivity compared to Si nanowires. These local heating effects have not been shown in previous studies involving the Raman scattering of vertically oriented Si nanowires, even for excitation intensities that are an order of magnitude larger than used in this research [58].

The research performed for this project indicates a resonant phenomenon that produces an optimal heating effect by an incident optical source (at a wavelength of 532 nm) at a nanowire diameter of 95 nm. In general, alternate incident wavelengths require different diameters for this resonance effect to occur. A direct implication of this research is that temperature gradients may possibly be generated by simply tuning the nanowire diameters in an array. This may have applications in planar PTE devices. Maximizing the ability for the incident light source to couple to the nanowires will greatly increase the efficiency of the generated heat in the next generations of PTE devices based GaAs materials.

References

[1] J. Aizpurua, P. Hanarp, D. S. Sutherland, M. Kall, Garnett W. Bryant, and F. J. Garcia de Abajo. Optical properties of gold nanorings. *Physical Review Letters*, 90, Feb 2003.

[2] R. Arnon and M. Sela. Antibodies to a unique region in lysozyme provoked by a synthetic antigen conjugate. *Proceedings of the National Academy of Sciences of the United States of America*, 62(1):163–70, January 1969.

[3] E. Bailo and V. Deckert. Tip-enhanced Raman scattering. *Chemical Society Reviews*, 37(5):921–30, May 2008.

[4] C. N. Banwell. *Fundamentals of Molecular Spectroscopy*. McGraw-Hill Book Company (UK) Limited, Maidenhead, Berkshire, England, third edition, 1972.

[5] E. R. Berman. *Biochemistry of the Eye*. Plenum Press, New York, 1991.

[6] P. F. Bernath. *Spectra of Atoms and Molecules*. Oxford University Press, Inc., New York, New York, 1995.

[7] J. M. Besson, J. P. Itié, A. Polian, G. Weill, J. L. Mansot, and J. Gonzalez. High-pressure phase transition and phase diagram of gallium arsenide. *Physical Review B*, 44:4214–4234, Sep 1991.

[8] C. C. F. Blake, D. F. Koenig, G. A. Mair, A. C. T. North, D. C. Phillips, and V. R. Sarma. Structure of hen egg-white lysozyme. *Nature Publishing Group*, 206(757-761), 1965.

[9] J. L. Bohnert, T. A. Horbett, B. D. Ratner, and F. H. Royce. Adsorption of proteins from artificial tear solutions to contact lens materials. *Investigative Ophthalmology & Visual Science*, 29(3):362–73, March 1988.

[10] F. Bonaccorso, Z. Sun, T. Hasan, and A. C. Ferrari. Graphene photonics and optoelectronics. *Nature Photonics*, 4(August):611–622, 2010.

[11] P. D. Boyer. *The Enzymes*, volume 7. 1972.

[12] H. Brunner and H. Sussner. Raman scattering of native and thermally denatured lysozyme. *Biochimica et Biophysica Acta*, 271:16–22, 1972.

[13] P. J. Cadusch, M. M. Hlaing, S. A. Wade, S. L. McArthur, and P. R. Stoddart. Improved methods for fluorescence background subtraction from Raman spectra. *Journal of Raman Spectroscopy*, 44(11):1587–1595, November 2013.

[14] E. J. Castillo, J. L. Koenig, J. M. Anderson, and J. Lo. Protein adsorption on hydrogels II. reversible and irreversible interactions between lysozyme and soft contact lens surfaces. *Biomaterials*, 6:338–345, 1985.

[15] NDT Resource Center. Nature of radiation. http://www.ndt-ed.org/EducationResources/CommunityCollege/RadiationSafety/theory/nature.htm.

[16] R. L. Chalmers. A review of the metabolism of hydrogen peroxide by external ocular structures. *International Contact Lens Clinic*, 22(78):143 – 147, 1995.

[17] M. C. Chen, R. C. Lord, and R. Mendelsohn. Laser-excited Raman spectroscopy of biomolecules IV. Thermal denaturation of aqueous lysozyme. *Biochimica et Biophysica Acta*, 328(2):252–60, December 1973.

[18] M. C. Chen, R. C. Lord, and R. Mendelsohn. Laser-excited Raman spectroscopy of biomolecules V. Conformational changes associated with the chemical denaturation of lysozyme. *Journal of the American Chemical Society*, 96(10):3038–42, May 1974.

[19] Y. Chen, K. Chen, H. Bai, and L. Li. Electrochemically reduced graphene porous material as light absorber for light-driven thermoelectric generator. *Journal of Materials Chemistry*, 22(34):17800–17804, 2012.

[20] C. Choy, P. Cho, M. V. Boost, and I. F. F. Benzie. Do multipurpose solutions damage porcine corneal epithelial cells? *Optometry and Vision Science*, 86(5):447–453, 2009.

[21] C. L. Christie and J. G. Meyler. Contemporary contact lens care products. *Contact Lens & Anterior Eye*, 20:11–17, January 1997.

[22] R. Claps, D. Dimitropoulos, V. Raghunathan, Y. Han, and B. Jalali. Observation of stimulated Raman amplification in silicon waveguides. *Optics Express*, 11(15):1731–9, July 2003.

[23] G. M. Cooper and R. E. Hausman. *The Cell: A Molecular Approach*. American Society for Microbiology Press, fifth edition, 2009.

[24] C. R. Daley, J. Flannery, S. Zhang, and J. A. Forrest. Nanoporous polystyrene prepared through the selective removal of low-M w component in polystyrene blends. 2014.

[25] K. Dalton and L. Subbaraman. Physical properties of soft contact lens solutions. *Optometry and Vision Science*, 85(2):122–128, 2008.

[26] M. Daune. *Molecular Biophysics: Structures in Motion*. Oxford University Press, New York, 1999.

[27] F. G. De Felice, M. Vieira, M. Meirelles, L. Morozova-Roche, C. Dobson, and S. Ferreira. Formation of amyloid aggregates from human lysozyme and its disease-associated variants using hydrostatic pressure. *The FASEB Journal*, 18(10):1099–101, July 2004.

[28] P. L. De La Jara, E. Papas, J. Diec, T. Naduvilath, M. D. P. Willcox, and B. A. Holden. Effect of lens care systems on the clinical performance of a contact lens. *Optometry and Vision Science*, 90(4):344–350, 2013.

[29] N. Dhindsa, A. Chia, J. Boulanger, I. Khodadad, R. R. Lapierre, and S. S. Saini. Highly ordered vertical gaas nanowire arrays with dry etching and their optical properties. *Nanotechnology*, 2014.

[30] B. Dippel. Raman Scattering Intensity. http://www.raman.de/htmlEN/basics/intensityEng.html.

[31] P. C. Donshik. Giant papillary conjunctivitis. *Transactions of the American Ophthalmological Society*, 92:687–744, January 1994.

[32] P. C. Donshik and A. D. Porazinski. Giant papillary conjunctivitis in frequent-replacement contact lens wearers: a retrospective study. *Transactions of the American Ophthalmological Society*, 97:205–220, 1999.

[33] K. Dumbleton, N. Keir, A. Moezzi, Y. Feng, L. Jones, and D. Fonn. Objective and subjective responses in patients refitted to daily-wear silicone hydrogel contact lenses. *Optometry and Vision Science*, 83(10):758–68, October 2006.

[34] R. E. Canfield E. F. Osserman and S. Beychok. *Lysozyme*. Academic Press, Inc., New York, 1974.

[35] J. R. Ferraro, K. Nakamoto, and C. W. Brown. *Introductory Raman Spectroscopy*. Elsevier Inc., San Diego, California, second edition, 2003.

[36] K. French and L. Jones. A decade with silicone hydrogels: part 1. *Optometry Today*, pages 42–46, 2008.

[37] K. French and L. Jones. A decade with silicone hydrogels: part 2. *Optometry Today*, pages 38–43, 2008.

[38] M. Gaft and L. Nagli. UV gated Raman spectroscopy for standoff detection of explosives. *Optical Materials*, 30(11):1739–1746, 2008.

[39] R.J. Garofalo, N. Dassanayake, C. Carey, J. Stein, R. Stone, and R. David. Corneal staining and subjective symptoms with multipurpose solutions as a function of time. *Eye and Contact Lens*, 31(4):166–174, 2005.

[40] K. Gericke. Groups and Their Representations. http://www.pci.tu-bs.de/aggericke/PC4e/Kap_IV/Gruppent.html.

[41] M. Gething and J. Sambrook. Protein folding in the cell. *Nature Publishing Group*, 355, 1992.

[42] J. P. Halper, N. Latovitzki, H. Bernstein, and S. Beychok. Optical activity of human lysozyme. *Proceedings of the National Academy of Sciences of the United States of America*, 68(3):517–22, March 1971.

[43] Horiba Scientific. *HR800 User Manual*, 2010.

[44] S. Hu, C.-Y. Chi, K.T. Fountaine, M. Yao, H.A. Atwater, P.D. Dapkus, N.S. Lewis, and C. Zhou. Optical, electrical, and solar energy-conversion properties of gallium arsenide nanowire-array photoanodes. *Energy and Environmental Science*, 6(6):1879–1890, 2013.

[45] R. Hughes, W. Heaselgrave, S. Kilvington, R. Hughes, W. Heaselgrave, and S. Kilvington. Acanthamoeba polyphaga strain age and method of cyst production influence the observed efficacy of therapeutic agents and contact lens disinfectants. *Antimicrobial Agents and Chemotherapy*, 47:3080–3084, 2003.

[46] K. Ikeda, K. Hamaguchi, M. Imanishi, and T. Amano. Effect of pH on the ultraviolet optical rotatory dispersion and circular dichroism of lysozyme. *Journal of Biochemistry*, 62(3):315–20, September 1967.

[47] G. Irmer, M. Wenzel, and J. Monecke. The temperature dependence of the lo(t) and to(t) phonons in gaas and inp. *Physica Status Solidi (B)*, 195(1):85–95, 1996.

[48] L. Jensen, C. M. Aikens, and G. C. Schatz. Electronic structure methods for studying surface-enhanced Raman scattering. *Chemical Society Reviews*, 37(5):1061–73, May 2008.

[49] L. Jones. Modern contact lens materials: a clinical performance update. *Contact Lens Spectrum*, 17(September 2002):24–35, 2002.

[50] L. Jones and C. Christie. Soft contact lens solutions review : part 2 : modern-generation care system. *Optometry in Practice*, 9:43–62, 2008.

[51] L. Jones, V. Franklin, K. Evans, R. Sariri, and B. Tighe. Spoilation and clinical performance of monthly vs. three monthly group II disposable contact lenses. *Optometry and Vision Science*, 73:16–21, 1996.

[52] L. Jones, D. Jones, and M. Houlford. Clinical comparison of three polyhexanide-preserved multi-purpose contact lens solutions. *Contact Lens & Anterior Eye*, 20(1):23–30, 1997.

[53] L. Jones and M. Senchyna. Soft contact lens solutions review part 1 : Components of modern care regimens. *Optometry in Practice*, 8:45–56, 2007.

[54] L. Jones, M. Senchyna, M.A. Glasier, J. Schickler, I. Forbes, D. Louie, and C. May. Lysozyme and lipid deposition on silicone hydrogel contact lens materials. *Eye Contact Lens*, 29, 2003.

[55] J. Kameoka and T. Good. Raman Spectroscopy - Optical Fingerprint. http://biomed.tamu.edu/obsl/OBSL/Research%20Projects/SERS_biosensor.htm.

[56] R.K. Khanna, D.D. Stranz, and B. Donn. A spectroscopic study of intermediates in the condensation of refractory smokes: matrix isolation experiments of sio. *The Journal of Chemical Physics*, 74(4):2108–2115, 1981.

[57] M. Khorasaninejad, S. Jafarlou, M. J. Wesolowski, C. R. Daley, J. B. Flannery, J. Forrest, and S. S. Saini. Highly enhanced Raman scattering of graphene using plasmonic nano-structure. *Scientific Reports*, 3:1–7, 2013.

[58] M. Khorasaninejad, J. Walia, and S. S. Saini. Enhanced first-order raman scattering from arrays of vertical silicon nanowires. *Nanotechnology*, 23(27):275706, 2012.

[59] K. Kneipp, Y. Wang, H. Kneipp, L. Perelman, I. Itzkan, R. Dasari, and M. Feld. Single molecule eetection using surface-enhanced Raman scattering (SERS). *Physical Review Letters*, 78(9):1667–1670, March 1997.

[60] D. La Hood. Daytime edema levels with plus powered low and high water content hydrogel contact lenses. *Optometry and Vision Science*, 68:877–880, 1991.

[61] J. Lamperski. Absorption and emission processes in two level system. http://www.invocom.et.put.poznan.pl/~invocom/C/P1-9/swiatlowody_en/p1-1_6_2.htm.

[62] P. Larkin. *Infrared and Raman Spectroscopy: Principles and Spectral Interpretation*. Elsevier Inc., Waltham, Massachusetts, 2011.

[63] B. Levy. Superficial corneal "staining"-clinical observation and risk assessment. *Eye & contact lens*, 33(4):165–6, July 2007.

[64] T. Liu. Black Body Radiation. http://astronomybythecosmos.com/the-universe/light/light-and-black-body-radiation/.

[65] H. Lodish, A. Berk, C. A. Kaiser, M. Krieger, M. P. Scott, A. Bretscher, H. Ploegh, and P. Matsudaira. *Molecular Cell Biology*. W. H. Freeman and Company, Houndmills, Basingstoke, England, sixth edition, 2008.

[66] R. C. Lord and N. T. Yu. Laser-excited Raman Spectroscopy of biomolecules I. native lysozyme and its consituent amino acids. *Journal of Molecular Biology*, 1970.

[67] D. Luensmann and L. Jones. Protein deposition on contact lenses: the past, the present, and the future. *Contact Lens & Anterior Eye*, 35(2):53–64, April 2012.

[68] M. Markoulli. Solution-induced corneal staining: review and case study. *Contact Lens Update*, 2012.

[69] G. McNay, D. Eustace, W. E. Smith, K. Faulds, and D. Graham. Surface-enhanced Raman scattering (SERS) and surface-enhanced resonance Raman scattering (SERRS): a review of applications. *Applied Spectroscopy*, 65(8):825–37, August 2011.

[70] E. Miyako, C. Hosokawa, M. Kojima, M. Yudasaka, R. Funahashi, I. Oishi, Y. Hagihara, M. Shichiri, M. Takashima, K. Nishio, and Y. Yoshida. A photo-thermal-electrical converter based on carbon nanotubes for bioelectronic applications. *Spectrochimica Acta Part A: Molecular and Biomolecular Spectroscopy*, 50(51):12266–12270, 2011.

[71] E. Miyako, H. Nagata, K. Hirano, Y. Makita, K.-I. Nakayama, and T. Hirotsu. Near-infrared laser-triggered carbon nanohorns for selective elimination of microbes. *Nanotechnology*, 18(47), 2007.

[72] T. Miyazawa, T. Shimanouchi, and S.-I. Muzushima. Normal vibrations of n-methylacetamide. *The Journal of Chemical Physics*, 29(3):611–616, 1958.

[73] T. Mizutani and A. Mizutani. Estimation of adsorption of drugs and proteins on glass surfaces with controlled pore glass as a reference. *Journal of Pharmaceutical Sciences*, 67(8):1102–1105, 1978.

[74] B. R. Mohammed. Amino Acids. http://biochemanics.wordpress.com/2013/03/31/amino-acids/.

[75] P. B. Morgan and N. Efron. A decade of contact lens prescribing trends in the United Kingdom. *Contact Lens & Anterior Eye*, 29(2):59–68, 2006.

[76] Multiple. Asparagine. http://chemistry.tutorvista.com/biochemistry/asparagine.html.

[77] Multiple. Protein Secondary Structure Analysis (PSSA) Module. http://www.bioinformatics.utep.edu/agriculture/PSSA-module.php.

[78] Multiple. Triclinic Crystal System I. http://metafysica.nl/triclinic_1.html.

[79] Multiple. Wikipedia - Disulfide Bond. http://en.wikipedia.org/wiki/Disulfide_bond.

[80] Multiple. Wikipedia - Fermi Resonance. http://en.wikipedia.org/wiki/Fermi_resonance.

[81] Multiple. Energy efficient solar cell breakthrough, 2010.

[82] Multiple. Proteins, 2011.

[83] J. Nichols. Growth in some specialty areas and consensus on lens discomfort highlighted an otherwise stable year. *Contact Lens Spectrum*, 2014.

[84] K. Ogasahara and K. Hamaguchi. Structure of lysozyme XII. Effect of pH on the stability of lysozyme. *The Journal of Biochemistry*, 61(2), 1967.

[85] A. Pastore and P Temussi. Protein aggregation and misfolding: good or evil? *Journal of Physics: Condensed Matter*, 24(24):244101, 2012.

[86] G. Placzek. *Rayleigh-Streuung und Raman-Effekt*. Leipzig : Akademische Verlagsgesellschaft, Germany, 1934.

[87] R. S. Porubcan, K. L. Watters, and J. T. Mcfarland. A laser Raman study of lysozyme denaturation. *Archives of Biochemistry and Biophysics*, 186(2):255–264, 1979.

[88] C. V. Raman. A new radiation. *Indian Journal of Physics*, (March):387–389, 1928.

[89] P. J. Russell, S. L. Wolfie, P. E. Hertz, C. Starr, and B. McMillan. *Biology: The Dynamic Science*, volume 1. 2008.

[90] W. M. Sears, J. L. Hunt, and J. R. Stevens. Raman scattering from polymerizing styrene I. vibrational mode analysis. *Journal of Chemical Physics*, 75:1589, 1981.

[91] D. K. Sen and G. S. Sarin. Biological variations of lysozyme concentration in the tear fluids of healthy persons. *The British Journal of Ophthalmology*, 70(4):246–8, April 1986.

[92] A. P. Shreve, N. J. Cherepy, and R. A. Mathies. Effective rejection of fluorescence interference in Raman spectroscopy using a shifted excitation difference technique. *Applied Spectroscopy*, 46(4):707–711, April 1992.

[93] D. Shugar. The measurement of lysozyme activity and the ultra-violet inactivation of lysozyme. *Biochimica et Biophysica Acta*, 8(3):302–9, March 1952.

[94] C. C. Skotnitsky, T. J. Naduvilath, D. F. Sweeney, and P. R. Sankaridurg. Two presentations of contact lens-induced papillary conjunctivitis (clpc) in hydrogel lens wear: Local and general. *Optometry and Vision Science*, 83(1):27–36, 2006.

[95] A. Smekal. Zuschriften und vorlaufige mitteilungen. *Naturwissenschaften*, 11(43):873–875, 1923.

[96] G. Socrates. *Infrared and Raman Characteristic Group Frequencies*. John Wiley and Songs Ltd, West Sussex, England, third edition, 2001.

[97] M. Soini, I. Zardo, E. Uccelli, S. Funk, G. Koblmller, A. Fontcuberta I Morral, and G. Abstreiter. Thermal conductivity of gaas nanowires studied by micro-raman spectroscopy combined with laser heating. *Applied Physics Letters*, 97(26), 2010.

[98] P. S. Soni, D. G. Horner, and J. Ross. Ocular response to lens care systems in adolescent soft contact lens wearers. *Optometry and Vision Science*, 73:70–85, 1996.

[99] T. G. Spiro and T. C. Strekas. Resonance Raman spectra of heme proteins. Effects of oxidation and spin state. *Journal of the American Chemical Society*, 570(20):338–345, 1974.

[100] L. N. Subbaraman. *Lysozyme deposition studies on silicone hydrogel contact lens materials*. PhD thesis, 2005.

[101] M. Suwala, M.-A. Glasier, L.N. Subbaraman, and L. Jones. Quantity and conformation of lysozyme deposited on conventional and silicone hydrogel contact lens materials using an in vitro model. *Eye and Contact Lens*, 33(3):138–143, 2007.

[102] J. Teichroeb. *Selected experiments with proteins at solid-liquid interfaces*. PhD thesis, University of Waterloo, Ontario, 2008.

[103] J. Tonge. Unlocking the secrets of enzyme power using Raman. *Accounts of Chemical Research*, (8):8–13.

[104] V. Vacque, B. Sombret, J. P. Huvennea, P. Legrand, and S. Suc. Characterisation of the O-O peroxide bond by vibrational spectroscopy. *Spectrochimica Acta Part A: Molecular and Biomolecular Spectroscopy*, (96):55–66, 1997.

[105] C. J. van Oss. Hydrophobicity of biosurfaces - Origin, quantitative determination and interaction energies. *Colloids and Surfaces B: biointerfaces*, 5(3-4):91–110, November 1995.

[106] J. Walia, N. Dhindsa, J. Flannery, I. Khodadad, J. Forrest, R. LaPierre, and S. Saini. Diameter dependent photo-thermal effects in vertically etched GaAs nanowire arrays. *IEEE International Conference on Nanotechnology*, 2014.

[107] D. R. Westenskow, K. W. Smith, D. L. Coleman, D. E. Gregonis, and R. A. Van Wagenen. Clinical evaluation of a Raman scattering multiple gas analyzer for the operating room, 1989.

[108] R. Willingale. Lasers and Quantum Optics. http://www.star.le.ac.uk/~zrw/courses/lect4313.html.

[109] Yikrazuul. Polystyrene. http://en.wikipedia.org/wiki/Polystyrene#mediaviewer/File:Polystyrene.svg.

[110] Yikrazuul. Wikipedia - Amino Acid. http://en.wikipedia.org/wiki/Amino_acid.

[111] Yikrazuul. Wikipedia - Lysozyme. http://en.wikipedia.org/wiki/Lysozyme.

[112] L. Zigler, R. Cedrone, D. Evans, C. Helbert-Green, and T. Shah. Clinical evaluation of silicone hydrogel lens wear with a new multipurpose disinfection care product. *Eye and Contact Lens*, 33(5):236–243, 2007.